Topics in Machining with Industrial Robots and Optimal Control of Vehicles

Olofsson, Björn

2013

Document Version:
Publisher's PDF, also known as Version of record

Topics in Machining with Industrial Robots and Optimal Control of Vehicles

Topics in Machining with Industrial Robots and Optimal Control of Vehicles

Björn Olofsson

Department of Automatic Control
Lund University
Lund, April 2013

Department of Automatic Control
Lund University
Box 118
SE-221 00 LUND
Sweden

ISSN 0280–5316
ISRN LUTFD2/TFRT--3259--SE

Printed in Sweden.
Lund 2013

Abstract

Two main topics are considered in this thesis: Machining with industrial robots and optimal control of road-vehicles in critical maneuvers. The motivation for research on the first subject is the need for flexible and accurate production processes employing industrial robots as their main component. The challenge to overcome here is to achieve high-accuracy machining solutions, in spite of strong process forces affecting the robot end-effector. Because of the process forces, the nonlinear dynamics of the manipulator, such as the joint compliance and backlash, significantly degrade the achieved position accuracy of the machined part. In this thesis, a macro/micro manipulator configuration is considered to the purpose of increasing the position accuracy. In particular, a model-based control architecture is developed for control of the micro manipulator. The macro/micro manipulator configuration are validated by experimental results from milling tests in aluminium. The main result is that the proposed actuator configuration, combined with the control architecture proposed in this thesis, can be used for increasing the accuracy of industrial machining processes with robots.

The interest for research on optimal control of road-vehicles in time-critical maneuvers is mainly driven by the desire to devise improved vehicle safety systems. Primarily, the solution of an optimal control problem for a specific cost function and model configuration can provide indication of performance limits as well as inspiration for control strategies in time-critical maneuvering situations. In this thesis, a methodology for solving this kind of problems is discussed. More specifically, vehicle and tire modeling and the optimization formulation required to get useful solutions to these problems are investigated. Simulation results are presented for different vehicle models, under varying road-surface conditions, in aggressive maneuvers, where in particular the tires are performing at their limits. The obtained results are evaluated and compared. The main conclusion here is that even simplified road-vehicle models are able to replicate behavior observed when experienced drivers are handling vehicles in time-critical maneuvers. Hence, it is plausible

that the results presented in this thesis provide a basis for development of future optimization-based driver assistance technologies.

Acknowledgments

I would like to acknowledge my supervisors, Prof. Anders Robertsson and Prof. Rolf Johansson, for continuous guidance during my Ph.D. studies. Further, Dr. Klas Nilsson has provided valuable comments on the work. My colleague within the COMET and SMErobotics projects, Olof Sörnmo, has been an inspiring research partner as well as traveling partner at project meetings and conferences around the world. Dr. Mathias Haage is acknowledged for good cooperation on the joint-based robot models and simulation of joint dynamics.

In the ELLIIT consortium, Karl Berntorp, has been an excellent research partner and Prof. Bo Bernhardsson provided constructive comments on the work. Kristoffer Lundahl, Prof. Lars Nielsen, and Dr. Jan Åslund, Linköping University, are acknowledged for good cooperation on the work with optimal control of vehicles and their sharing of knowledge of vehicle and tire dynamics.

I am also grateful to Dipl.-Ing. Ulrich Schneider, Dr. Arnold Puzik, and Dipl.-Ing. Manuel Drust at Fraunhofer IPA, Germany, for numerous fruitful workshops in the Robotics Lab in Stuttgart and discussions on the micro manipulator for machining. Dipl.-Ing. Christian Lehmann and Dipl.-Ing. Marcel Halbauer, Brandenburg University of Technology, Germany, are acknowledged for the joint work on the clamping method for identification of robot joint properties.

I also extend my acknowledgments to my colleagues at the Department of Automatic Control at Lund University for interesting discussions on control theory, and to the technical and administrative staff at the department for assistance on various subjects related to my research.

Financial support is gratefully acknowledged from the European Commission's Seventh Framework Program under grant agreements COMET (ref. #258769) and SMErobotics (ref. #287787), as well as the Swedish Foundation for Strategic Research within the program ProViking, under grant ProFlexA PV08–0036. The author is part of the LCCC Linnaeus Center,

supported by the Swedish Research Council, and the ELLIIT Excellence Center, supported by the Swedish Government.

Contents

Abstract **5**

Acknowledgments **7**

1. Introduction **11**
1.1 Background and Motivation 11
1.2 Publications 12
1.3 Outline and Contributions 14

I Machining with Industrial Robots **16**

2. Introduction **17**
2.1 Motivating Machining Example 17
2.2 The COMET project 24
2.3 Micro Manipulator for Machining 25

3. Modeling and Control of the Micro Manipulator **28**
3.1 Introduction 28
3.2 Micro Manipulator Design 28
3.3 Dynamic Characterization of the Micro Manipulator 29
3.4 Modeling of the Mechanical Construction 31
3.5 Position Control of the Micro Manipulator 38
3.6 Conclusions 43

4. Nonlinear Model-Based Control of the Micro Manipulator **45**
4.1 Introduction 45
4.2 Background 45
4.3 Theory of Nonlinear Hysteresis Models 46
4.4 Model Identification 49
4.5 Experimental Results 56
4.6 Conclusions 59

5. Experimental Verification of the Micro Manipulator **61**
5.1 Introduction 61

5.2 Experimental Setup 61
5.3 Experimental Results 62
5.4 Experimental Evaluation 65
5.5 Discussion 69
5.6 Conclusions 74
6. Conclusions and Future Work **75**

II Optimal Control of Vehicles **76**
7. Introduction **77**
8. Optimization Methodology for Road-Vehicle Maneuvers **79**
8.1 Introduction 79
8.2 Problem Description 79
8.3 Modeling 80
8.4 Optimal Control Problem 86
8.5 Results 89
8.6 Conclusions 101
9. Optimal Maneuvers on Uncertain Road-Surfaces **102**
9.1 Introduction 102
9.2 Problem Description 103
9.3 Modeling 103
9.4 Results 106
9.5 Conclusions 114
10. Conclusions and Future Work **116**
Bibliography **117**
A. Vehicle and Tire Model Parameters **125**
B. Code Listings **128**

1

Introduction

This thesis considers two different topics: Machining with industrial robots and optimal control of road-vehicles in critical maneuvers. The common theme of these two topics is the importance of accurate motion control in advanced applications; the robot in a machining scenario with significant process forces affecting the robot end-effector and the vehicle in a time-critical situation, where in particular the tires are performing at their limits.

1.1 Background and Motivation

Motion control of industrial serial kinematic robots has been investigated in the scientific community for several decades. Hence, the positioning accuracy achieved with model-based feedforward control combined with joint-servo feedback controllers for a robot moving in free space is satisfactory for most applications. In addition, certain methods and products exist for achieving absolute accuracy by kinematic calibration. For an introduction to robot modeling and control, see, *e.g.*, [Spong et al., 2006] and [Siciliano et al., 2009]. When considering machining applications traditionally performed with dedicated machine tools—where the manipulator and the tool form a kinematic chain with the workpiece—the effects of joint dynamics such as friction, backlash, and compliance influence the positioning accuracy significantly. This is mainly caused by the process forces required for these tasks, but in addition the accuracy to be fulfilled in these kind of applications is often below 50–100 μm. This motivates the need for research on methods and strategies for increasing the accuracy of machining tasks performed with industrial robots. In this thesis, a macro/micro manipulator configuration for milling scenarios is considered. The configuration is modeled and a subsequent control architecture is developed, which finally is verified in milling experiments.

The interest for optimal control of road-vehicles is mainly driven and motivated by the need for improved safety systems and driver assistance

technologies, see, *e.g.*, [Sharp and Peng, 2011]. In order to increase the understanding of vehicle dynamics, optimal vehicle control in time-critical situations is an appealing approach in order to trigger extreme modes in the vehicle dynamics and to find performance limits. The challenge here is to find vehicle models—and in particular tire models—which contain sufficient expressiveness in order for the results to be useful, not only in a simulation setting but also for vehicle control in general. The overall aim of these kind of studies is to find vehicle behavior and control strategies, which can lead the way to new vehicle safety systems. In this thesis, optimal control of road-vehicles in certain critical maneuvers, resulting in aggressive maneuvering behavior, is investigated. In particular, the tire and vehicle modeling required for optimal control applications is in focus in these studies.

1.2 Publications

In this section, the publications on which this thesis is based are presented. The publications are divided into two parts; machining with industrial robots and optimal control of vehicles.

Machining with Industrial Robots

Olofsson, B., O. Sörnmo, U. Schneider, A. Robertsson, A. Puzik, and R. Johansson (2011). "Modeling and control of a piezo-actuated high-dynamic compensation mechanism for industrial robots". In: *IEEE/RSJ Int. Conf. on Intelligent Robots and Systems (IROS)*. San Francisco, CA, pp. 4704–4709.

Olofsson, B., O. Sörnmo, U. Schneider, M. Barho, A. Robertsson, and R. Johansson (2012). "Increasing the accuracy for a piezo-actuated micro manipulator for industrial robots using model-based nonlinear control". In: *10th Int. IFAC Symp. on Robot Control (SYROCO)*. Dubrovnik, Croatia, pp. 277–282.

Sörnmo, O., B. Olofsson, U. Schneider, A. Robertsson, and R. Johansson (2012). "Increasing the milling accuracy for industrial robots using a piezo-actuated high-dynamic micro manipulator". In: *IEEE/ASME Int. Conf. on Advanced Intelligent Mechatronics (AIM)*. Kaohsiung, Taiwan, pp. 104–110.

Publication one and three were developed as a cooperation between the author and O. Sörnmo, and equal contribution is asserted. The author was main responsible for the modeling and control development and O. Sörnmo was main responsible for the experimental verification. A. Puzik developed the considered micro manipulator for online compensation and U. Schneider

took part in the implementation and the experiments. A. Robertsson and R. Johansson provided comments on the manuscript.

In the second publication, the author developed the models from experimental data. O. Sörnmo discussed the methodology with the author. U. Schneider and M. Barho performed the experiments. A. Robertsson and R. Johansson provided comments and assisted in structuring the manuscript.

Optimal Control of Vehicles

Berntorp, K., B. Olofsson, K. Lundahl, B. Bernhardsson, and L. Nielsen (2013). "Models and methodology for optimal vehicle maneuvers applied to a hairpin turn". In: *Am. Control Conf. (ACC)*. Washington, D.C. *Accepted for publication*.

Lundahl, K., K. Berntorp, B. Olofsson, J. Åslund, and L. Nielsen (2013). "Studying the influence of roll and pitch dynamics in optimal road-vehicle maneuvers". In: *Int. Symp. on Dynamics of Vehicles on Roads and Tracks (IAVSD)*. Qingdao, China. *Accepted for publication*.

Olofsson, B., K. Lundahl, K. Berntorp, and L. Nielsen (2013). "An investigation of optimal vehicle maneuvers for different road conditions". In: *7th IFAC Symp. on Advances in Automotive Control (AAC)*. Tokyo, Japan. *Submitted*.

The author developed the optimization methodology and performed the optimizations, whose results are presented in the first and third publication, together with K. Berntorp, and equal contribution is asserted. K. Lundahl developed the models utilized in the optimal control formulation together with the author and K. Berntorp, as well as performed the optimizations whose results are presented in the second publication. B. Bernhardsson and L. Nielsen provided comments on the methodology and assisted in structuring the manuscripts.

Other Related Publications

The following publications, where the author also has made contributions in related areas, were decided not to be part of the present thesis.

Berntorp, K., B. Olofsson, and A. Robertsson (2013). "Path tracking with obstacle avoidance for pseudo-omnidirectional mobile robots using convex optimization". In: *Proc. Conf. Decision and Control (CDC)*. Firenze, Italy. *Submitted*.

Lehmann, C., B. Olofsson, K. Nilsson, M. Halbauer, M. Haage, A. Robertsson, O. Sörnmo, and U. Berger (2013). "Robot joint modeling and parameter identification using the clamping method". In: *IFAC Conf. on Manufacturing Modelling, Management, and Control (MIM)*. St. Petersburg, Russia. *Accepted for publication*.

Olofsson, B., H. Nilsson, A. Robertsson, and J. Åkesson (2011). "Optimal tracking and identification of paths for industrial robots". In: *Proc. 18th World Congress of the Int. Federation of Automatic Control (IFAC)*. Milano, Italy, pp. 1126–1132.

Sörnmo, O., B. Olofsson, A. Robertsson, and R. Johansson (2012). "Increasing time-efficiency and accuracy of robotic machining processes using model-based adaptive force control". In: *10th Int. IFAC Symp. on Robot Control (SYROCO)*. Dubrovnik, Croatia, pp. 543–548.

The first publication was developed as a cooperation between the author and K. Berntorp, and equal contribution is asserted and joint first-authorship is claimed. A. Robertsson provided comments on the method and assisted in structuring the manuscript.

In the second publication, the author developed the method from an original idea of K. Nilsson. C. Lehmann and M. Halbauer performed the experiments and developed parts of the experimental procedure. The remaining authors took part in the discussions and implementation of the method.

The third publication was based on the Master Thesis of the author, which was performed together with H. Nilsson. The author wrote the paper and A. Robertsson and J. Åkesson provided comments on the method and assisted in structuring the manuscript.

In the fourth publication, the author contributed with ideas for the developed method and assisted in the experimental work.

1.3 Outline and Contributions

The main contributions of this thesis are:

- Modeling and control of a micro manipulator for online position compensation in high-accuracy machining production scenarios using industrial robots;
- An experimental verification of the proposed micro manipulator control architecture in a milling scenario;
- A methodology for calculation of optimal road-vehicle maneuvers and a subsequent investigation of the influence of vehicle and tire model configurations;

- An investigation of the influence of road-surface uncertainties in optimal road-vehicle maneuvers.

This thesis comprises two parts. Part 1 presents results related to machining with industrial robots. Chapter 2 gives a background to the subject and provides a motivating machining example and discusses the challenges of machining with industrial robots. Modeling and subsequent model-based control of a micro manipulator for milling applications using industrial robots are presented in Chapter 3. An extension of the control architecture, with explicit modeling of the nonlinear dynamics of the micro manipulator, is discussed in Chapter 4. The proposed method and control architecture are evaluated in milling experiments, whose results are presented and discussed in Chapter 5. Finally, conclusions and aspects on future work are provided in Chapter 6.

The second part of the thesis, Part 2, discusses optimal control of vehicles, and in particular control of road-vehicles. An introduction to the subject is given in Chapter 7. In Chapter 8, a methodology for solving optimal control problems for road-vehicles in time-critical situations is proposed. In addition, vehicle and tire modeling with focus on optimal control is discussed and simulation results are presented. In Chapter 9, optimal vehicle maneuvers on different road-surfaces are investigated. In addition, simulation results are provided showing the vehicle behavior on the investigated road-surfaces. This part of the thesis is concluded in Chapter 10.

Part I

Machining with Industrial Robots

2

Introduction

As a result of the increased demands on efficiency and flexibility in industrial production over the past decades, the need for automated, flexible, and high-accuracy machining tasks has increased. In this context, usage of industrial robots is an appealing solution based on their flexibility in terms of reconfiguration possibilities, versatility, and their relatively low investment cost, compared to the cost of a machine tool. However, because of the limited stiffness and position-accuracy of industrial robots, and consequently their inability to execute tasks based on *Computer-Aided Design* (CAD) specifications with acceptable results, machining operations are not straightforward to perform, see, *e.g.*, [Zhang et al., 2005; Abele et al., 2011; Wang et al., 2009; Pan and Zhang, 2009]. Further, the nonlinear dynamics of the robot joints, such as backlash, friction, and nonlinear stiffness, are important for the Cartesian positioning accuracy, since the joint servo controllers are based on measurements on the motor side of the joint. Consequently, discrepancies between the arm-side position and the motor-side position for the joints occur. The dynamics of a robot joint is depicted in Figure 2.1, where the variables included in the model are explained in Table 2.1.

2.1 Motivating Machining Example

In order to illustrate some of the challenges in machining with industrial robots and motivate the work presented in this part of the thesis, a milling task executed in aluminium is considered in this section. The task is to remove material in a rectangular area, referred to as a pocket, see Figure 2.2.

The procedure for the milling task was as follows: First, the milling path was computed from CAD data of the robot cell and the workpiece using a *Computer-Aided Manufacturing* (CAM) software and subsequently a robot program was generated. Second, the milling task was performed with an industrial robot of model IRB2400 from ABB [ABB Robotics, 2012], which was holding the workpiece. The machining spindle was attached to a base

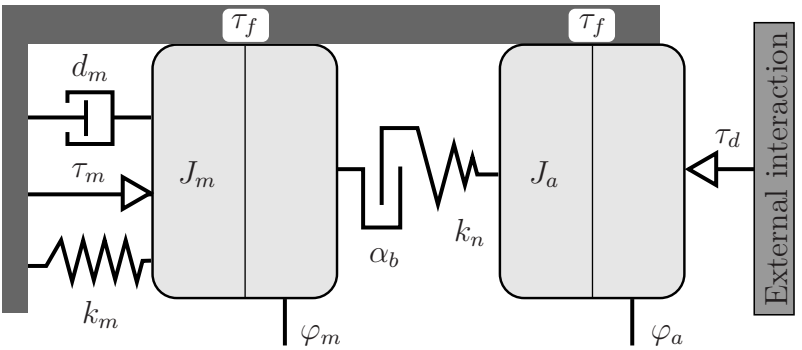

Figure 2.1 Robot joint model with nonlinear dynamics, depicted as a prismatic joint for simplicity.

Table 2.1 Variables and parameters in the nonlinear robot joint model depicted in Figure 2.1.

τ_m	—	Torque from controller to motor
τ_d	—	External disturbance torque
φ_m	—	Joint angle, motor side
φ_a	—	Joint angle, arm side
α_b	—	Backlash angle
k_n	—	Nonlinear spring constant
τ_f	—	Friction torque
J_m	—	Actuator/motor inertia
J_a	—	Arm side inertia
k_m	—	Stiffness accomplished by controller
d_m	—	Damping accomplished by controller

inside the robot working space, see Figure 2.3. The spindle was running at a speed of 24 000 rpm and the milling tool had a diameter of 7 mm. For arm-side measurements of the position and orientation of the tool center point (TCP) coordinate system, defined at the robot end-effector, an optical tracking system from Nikon Metrology of model K600 [Nikon Metrology, 2010] was used. This tracking system provides data at a sample rate of 1 kHz during the whole milling process. In addition, a force/torque sensor was attached to the robot end-effector for measurements of the process forces. For accessing the sensor data in the robot controller, the ExtCtrl architecture [Blomdell et al., 2010; Blomdell et al., 2005; Nilsson and Johansson, 1999], a research interface to ABB S4CPlus and IRC5 controllers, was used.

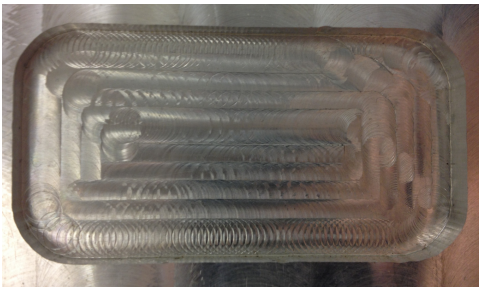

Figure 2.2 Milling task where a rectangular area of material, a so called pocket, is to be removed.

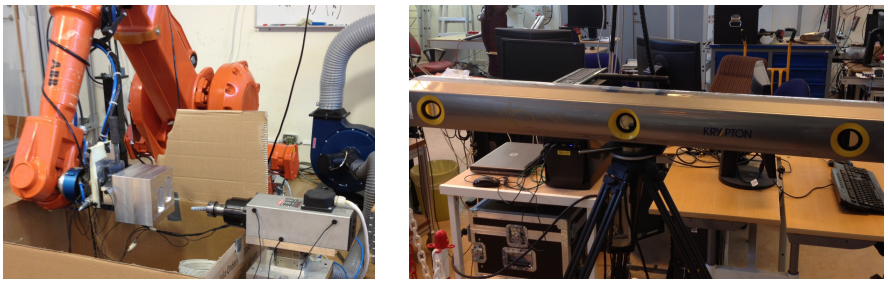

Figure 2.3 Experimental setup for milling experiments (left) at Lund University, including an optical tracking system (right) for high-accuracy measurements of robot position and orientation.

The milling experiment was performed, whereby the results displayed in Figure 2.4 were obtained. It is to be noted that the path planning is such that the pocket is created in several milling runs, where the accumulated depth-of-cut is increased in every cycle. This strategy is common practice for machine tools and has for that reason also been adopted in the path planning software utilized in this experiment. Further, the milling tool left the workpiece between each cycle, resulting in the characteristic force transients visible in the process force data when reentering the material prior to each cycle. Several conclusions can be drawn from the experimental data, exhibiting the challenges of machining with industrial robots:

- Uncertainty in the calibration of the robot—*i.e.*, in particular the kinematic parameters—and the aluminium block results in position and orientation errors of the workpiece which means that the milling tool is not completely orthogonal to the machined surface;
- The negative influence of the backlash in the robot joints, clearly visible

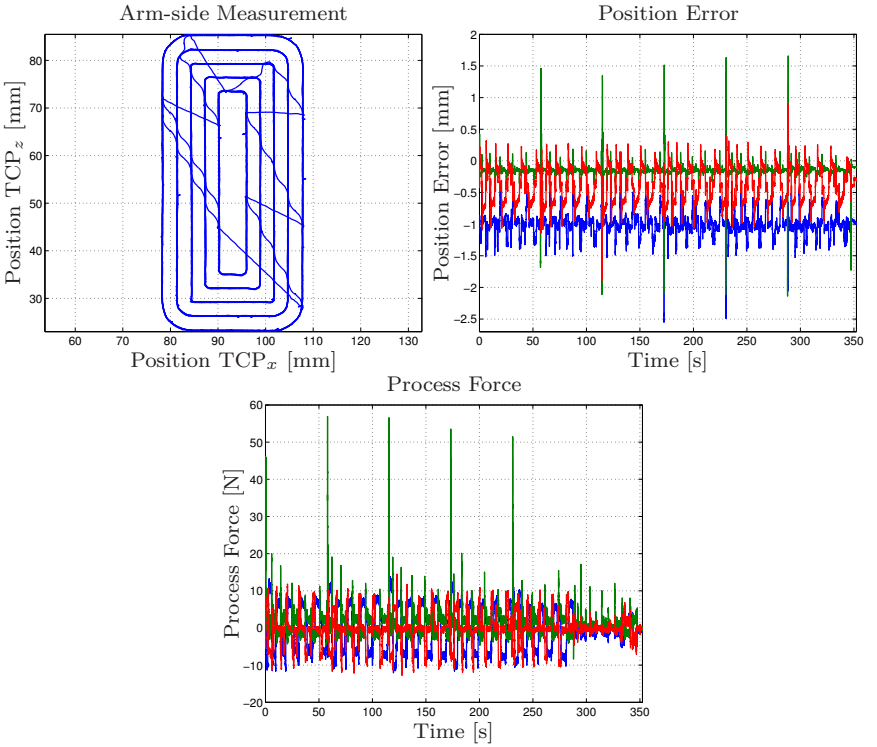

Figure 2.4 Measurements during a milling task with an industrial robot of model ABB IRB2400, see Figure 2.3. Subplots: Arm-side position measurements (upper left), position error (upper right), and process forces (lower center). Color scheme in upper right and lower plot: TCP$_x$–blue, TCP$_y$–green, and TCP$_z$–red.

in the machined surface in Figure 2.2 at the locations where the gears of the motors reverse motion direction and thus excite the backlash;

- Position deviations occurring when the milling tool enters the material and consequently gives rise to significant force transients with frequency characteristics higher than the bandwidth of the position control loop of the robot;

- The limited stiffness of the industrial robot—or more specifically the compliance of the robot joints—which results in position deviations when the process forces affect the robot end-effector.

Eigenfrequencies in Cartesian Space Considering the joint-based actuation for a serial kinematic robot and that the high-frequency disturbances

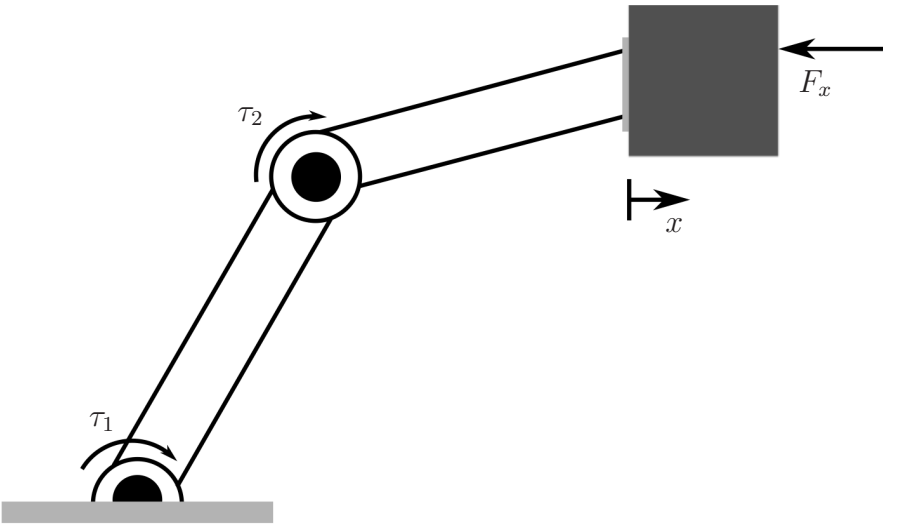

Figure 2.5 Schematic of a simplified robot manipulator with joint actuation with torques τ_1 and τ_2, where high-frequency force disturbances F_x from the machining process enter at the end-effector. The disturbances result in a position deflection x.

from the milling process enter the robot at the end-effector, not only the joint actuation bandwidth of the robot is of importance but also the bandwidth for disturbance rejection at the TCP. The latter is significantly different from the joint actuation bandwidth because of the mechanical structure of the links. The noncolocation of actuation and disturbances is schematically illustrated in one dimension for a simplified two degrees-of-freedom robot in Figure 2.5. For illustration purposes, an impulse response experiment was performed, where a force impulse was applied to the end-effector of the ABB IRB2400 robot and the subsequent position deflection was measured simultaneously as the forces. The deflection of the robot was measured using the Nikon Metrology K600 optical tracking system. The result is displayed in Figure 2.6. As can be observed in the experimental data, all Cartesian directions exhibit natural eigenfrequencies in the range of 10–25 Hz, with different damping in the different directions. This implies the limitations on the process force disturbance-rejection bandwidth. The Cartesian eigenfrequencies of the robot also exhibit a dependency on the robot configuration.

Nonlinear Dynamics in Robot Joints Modeling and investigation of the nonlinear dynamics of robot joints have been discussed extensively in the literature. Methods for measuring the static and dynamic joint friction in industrial manipulators have been investigated previously, see, *e.g.*, [Bitten-

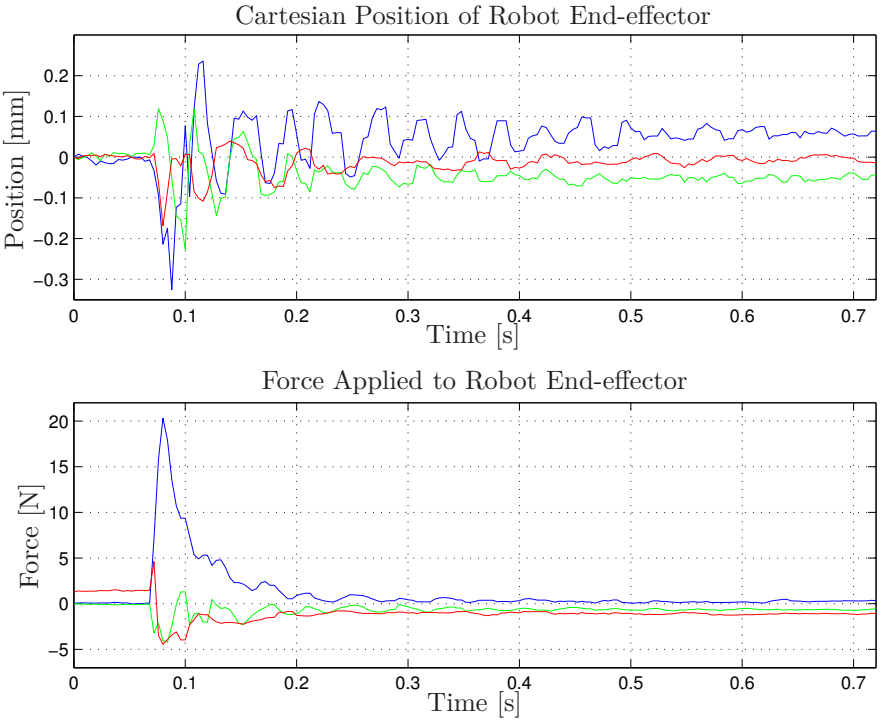

Figure 2.6 Impulse response obtained by applying a force on the robot end-effector and measuring the corresponding deflection. Color scheme: TCP_x–blue, TCP_y–green, and TCP_z–red.

court et al., 2010]. Friction modeling in general is discussed extensively in [Olsson, 1996]. Further, methods and strategies for modeling and quantifying the backlash in robot joints have been discussed in [Hovland et al., 2002; Ruderman et al., 2009]. Stiffness modeling and subsequent online position error compensation are discussed in [Abele et al., 2008; Wang et al., 2009; Pan and Zhang, 2009].

The static friction torques for different motor velocities were estimated for each of the joints on the ABB IRB2400 robot setup as an illustration. A model similar to the one presented in [Bittencourt et al., 2010] is adopted. In the model, both viscous friction and the Stribeck effect are considered. The friction torque τ_f can be written as

$$\tau_f(\dot{\varphi}_m) = \left(F_C + F_S e^{-\left|\frac{\dot{\varphi}_m}{\dot{\varphi}_S}\right|^{\alpha}} \right) \text{sign}(\dot{\varphi}_m) + F_V \dot{\varphi}_m, \tag{2.1}$$

where $F_C, F_S, \dot{\varphi}_S, \alpha$, and F_V are model parameters to be determined from

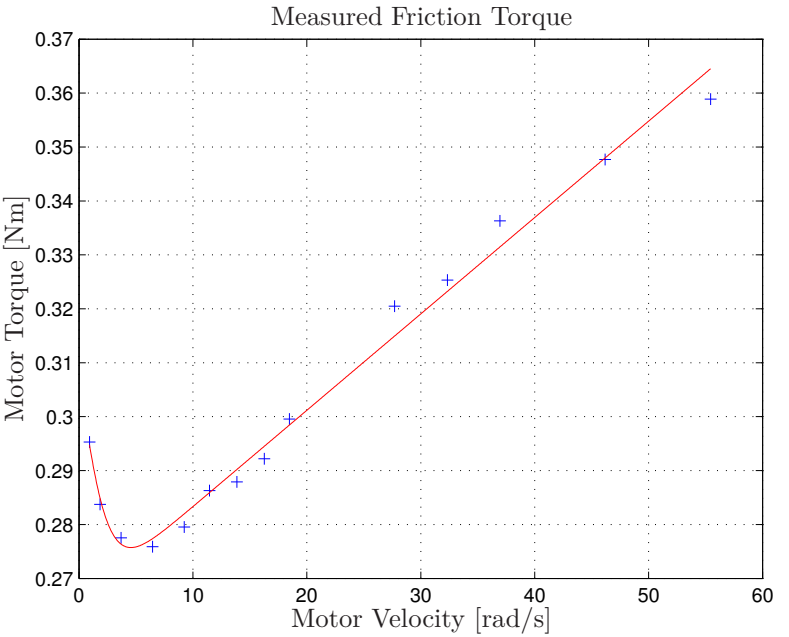

Figure 2.7 Friction measurements (blue cross) for joint 2 on the IRB2400 robot. The red solid line represents a fit of the measured data to the model in (2.1). The Stribeck effect is clearly visible for low motor velocities.

experimental data. For obtaining an estimate of the friction in the robot joint, the procedure described in [Bittencourt et al., 2010] was performed. With this method, a sequence of constant joint velocities are referenced to the joint servo controllers, while the required motor torques are measured. The friction behavior for the second joint of the ABB IRB2400 robot is displayed in Figure 2.7, where the stationary friction torque is displayed as function of the motor velocity. It is to be noted that the Stribeck effect is clearly visible for low motor velocities, whereas for higher motor velocities the viscous friction is dominant. The measured data was fitted to the model in (2.1). The model parameters for the current joint are

$$F_C = 0.27, \quad F_S = 0.046, \quad \dot{\varphi}_S = 1.7, \quad \alpha = 1.1, \quad F_V = 0.0018.$$

The friction behavior displayed in Figure 2.7 is typical for robot joints. The measured friction behavior for the remaining joints of the investigated robot is similar, even though the Stribeck effect is less pronounced in some of the smaller wrist joints.

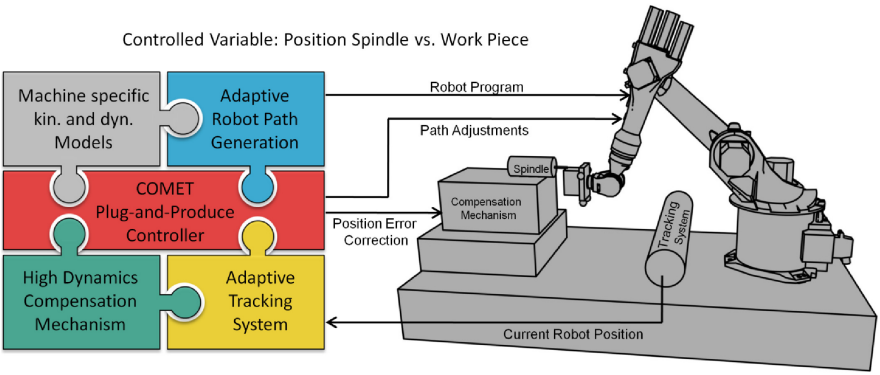

Figure 2.8 Graphical representation of the research aim of the COMET project, and its four corner stones [COMET, 2013].

2.2 The COMET project

Within the research project COMET[1] [COMET, 2013] started in 2010, the aim is to develop milling solutions for industrial robots achieving an accuracy better than 50 µm. This research is performed in a four-step procedure according to Figure 2.8. The four different parts of the project can be summarized as follows:

Kinematic and Dynamic Models In order to increase the machining accuracy, both kinematic and dynamic models of the robot are developed. The kinematic models consist of the Denavit-Hartenberg parameters [Denavit and Hartenberg, 1955] as well as the geometric data of the robot. Further, the dynamic models are to describe the joint dynamics of the robot, significantly influencing the milling accuracy as observed in the milling experiment in the previous section. In particular, essential properties such as friction, backlash, and compliance are considered in the joint-based robot models. Further, methods for determining these properties of an industrial robot using automated procedures are investigated.

Model-Based Path Generation Based on the kinematic and dynamic models, an improved strategy for offline path planning is developed. In the path-planning stage, the models are utilized in order to plan a reference path utilizing CAM software which, taking the developed models into account, results in the desired milling path.

[1] Plug-and-produce COmponents and METhods for adaptive control of industrial robots enabling cost effective, high precision manufacturing in factories of the future

Real-Time 6D Tracking System As opposed to the two approaches described in the previous paragraphs based on offline compensation, also online strategies for improving the milling accuracy are investigated. To this purpose, online real-time 6D-compensation is developed, where the term 6D here refers to position and orientation. The position and orientation of the robot workpiece are measured using optical tracking systems, whose measurements are fed to the robot controller and position corrections are performed in real-time.

Micro Manipulator for Milling For milling tasks with industrial robots demanding high position-accuracy, a micro manipulator where the machining spindle is attached was developed. The aim of the micro manipulator is to compensate online for the 3D position deviations of the robot, as measured by the optical tracking system. By design, the micro manipulator has a significantly higher bandwidth than the robot. Consequently, position deviations with higher frequency than the robot bandwidth are to be fed to the micro manipulator—which has a geometrically limited compensation range—whereas low-frequency and stationary errors are handled by the robot itself.

Focus of This Thesis In this thesis, research results from the development of the control architecture for the micro manipulator are presented. The background and motivation for this development are discussed next.

2.3 Micro Manipulator for Machining

For high-accuracy milling tasks, a piezo-actuated 3D-compensation mechanism has been developed [Puzik et al., 2009; Puzik et al., 2010; Puzik, 2011] at the Fraunhofer Institute for Manufacturing and Engineering in Stuttgart, Germany. The mechanism is to compensate for the remaining position errors of the robot, which the robot *per se* is unable to compensate for because of its limited structural bandwidth. The bandwidth of the position control for the robot is mainly limited by the eigenfrequencies of the manipulator structure, as experimentally indicated in Section 2.1. In the proposed setup, the spindle holding the milling tool is attached to the compensation mechanism and the robot is consequently holding the workpiece. A subsequent experimental setup is displayed in Figure 2.9.

The main contribution of the present thesis is the development of a model-based control architecture and an experimental verification of the proposed method for machining with industrial robots. A first prototype version of the control architecture is presented, as well as an improved version with explicit consideration of the nonlinear dynamics of the micro manipulator. The experimental evaluation presents results from milling tasks in aluminium using both peripheral and face milling strategies. In addition, the experimental ver-

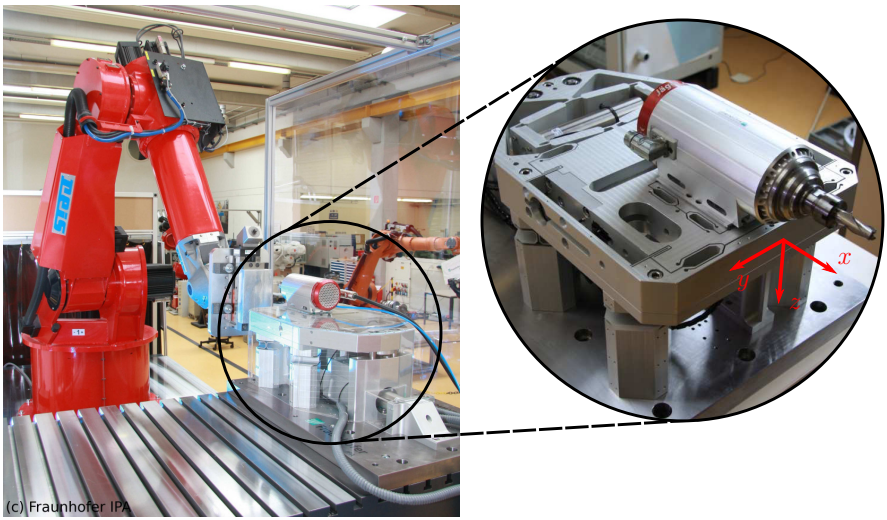

Figure 2.9 The experimental setup at Fraunhofer IPA, Stuttgart, Germany, for online compensation of positioning errors during machining tasks, where the robot holds the workpiece and the milling spindle is attached to the micro manipulator. A close-up of the micro manipulator, as seen from the opposite side, is displayed to the right in the figure.

ification contrasts the milling accuracy achieved by using the compensation mechanism to the standard uncompensated case.

The advantages of utilizing an additional manipulator, with higher bandwidth than the primary robot, together with a robot manipulator in a closed kinematic chain, has previously been investigated by Sharon, Fasse, and Hogan et al., see, *e.g.*, [Sharon et al., 1993; Fasse and Hogan, 1995]. It was shown that the bandwidth of the endpoint position-control loop was increased. The concepts of macro and micro manipulator were introduced to describe the robot and the additional compensation mechanism, respectively. These terms are adopted in this thesis. It is to be noted, though, that the micro manipulator in the experimental setup proposed in this thesis is not attached to the robot end-effector as an additional joint.

Piezo-actuated mechanisms based on flexure elements have been proposed for micro and nano manipulation earlier, see, *e.g.*, [Li and Xu, 2011; Liaw and Shirinzadeh, 2010]. Although the compensation mechanism considered in this thesis utilizes similar components in its mechanical design, there are significant differences. Previous designs were designed for compensation in micro and nano manipulation, whereas the micro manipulator discussed in this thesis is designed for machining processes with industrial robots, where strong process forces are required to fulfill the specified task.

In [Vuong et al., 2009], a control architecture for task-space control of industrial manipulators, with a hierarchical structure similar to the one utilized for control of the micro manipulator discussed in this thesis, is presented. However, the control of the micro manipulator in this thesis is performed directly in task space, due to the decoupled nature of the actuation axes of the mechanism.

3

Modeling and Control of the Micro Manipulator

3.1 Introduction

In this chapter, modeling and position control design for the micro manipulator for machining tasks with industrial robots are discussed. Dynamic models of the system and a subsequent model-based control architecture are developed. This chapter is based on the publications [Olofsson et al., 2011a] and [Sörnmo et al., 2012].

The structure of this chapter is as follows: First, the mechanical design of the micro manipulator is reviewed in Section 3.2. Subsequently, a dynamic characterization of the micro manipulator is presented in Section 3.3, which provides the foundation for the modeling discussed in Section 3.4. Section 3.5 presents a model-based control architecture for position control of the micro manipulator. The chapter is concluded with a summary in Section 3.6.

3.2 Micro Manipulator Design

In order to provide a basis for the development of position control algorithms, the mechanical design of the micro manipulator is reviewed in this section. The design is such that translational motion of the machining spindle is possible in all three Cartesian directions. However, there are no rotational degrees of freedom. Referring to Figure 2.9, the actuation axes are hereafter called x, y, and z, respectively.

The mechanism is actuated by piezo-actuators, which realize the stiff and strong actuation required to withstand the process forces used during the milling process. The movements of the piezo-actuators are transferred to a corresponding translational movement of the spindle *via* a flexure mechanism, see Figure 3.1. The flexure elements are constructed using *solid-state joints*—*i.e.*, the joints are cut directly in the solid aluminium base plate. The flexure

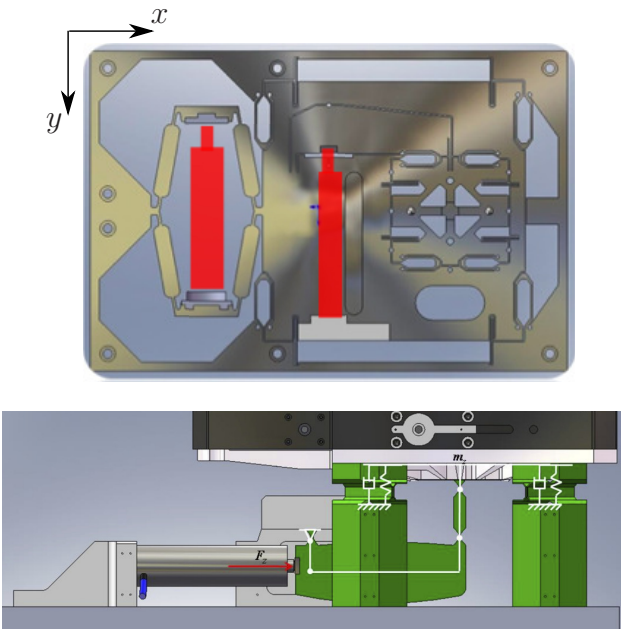

Figure 3.1 Actuation principle for the axes of the micro manipulator, x- and y-axes (upper drawing) and z-axis (lower drawing). The piezo-actuators in the xy-plane are marked by red color in the upper drawing [Puzik et al., 2009; Puzik et al., 2010; Puzik, 2011].

elements result in an effective gear ratio between actuator side and end-effector side along each of the motion axes. The maximum extension of the different piezo-actuators is 100–180 µm and the gear ratio in each of the axes is between four and five, which results in a maximum compensation range of approximately 0.5 mm in each direction. The micro manipulator is equipped with strain gauges integrated into the piezo-actuators measuring the corresponding extensions with temperature compensation, thus achieving a resolution of 0.7 µm. In addition, capacitive sensors which measure the Cartesian position of the end-effector with a resolution of 0.15 µm and a bandwidth of 2 kHz, are integrated into the micro manipulator. For further details regarding the mechanical design and sensor integration, the reader is referred to [Puzik et al., 2009; Puzik et al., 2010; Puzik, 2011].

3.3 Dynamic Characterization of the Micro Manipulator

Because of the inherent resonant character of the mechanical design—which is a result of the flexure elements utilized—and the nonlinear effects which

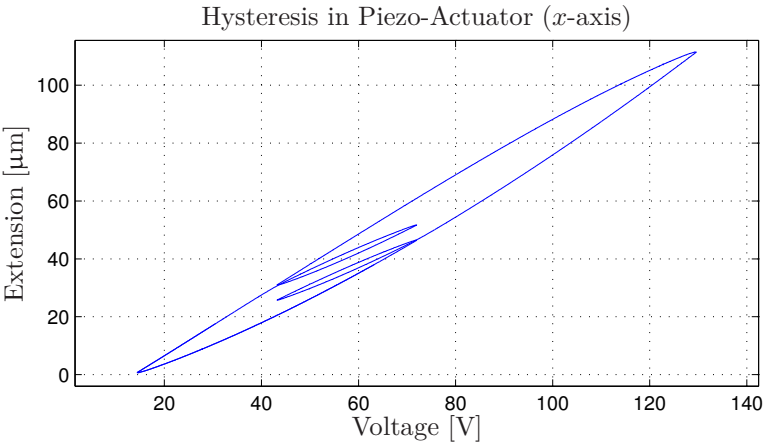

Figure 3.2 Characterization of hysteresis in the dynamics along the x-axis of the micro manipulator in the case of a linear, alternatingly increasing and decreasing, input with changing amplitude. Note the complex behavior of the hysteresis, which exhibits both rate and amplitude dependency.

appear in piezo-actuators, accurate positioning control of the micro manipulator without oscillations under milling process disturbances is a challenging control problem. A model-based solution is here pursued in order to control the tool position.

Nonlinear Phenomena in the Piezo-Actuators

It is well-known that piezo-actuators exhibit a nonlinear relationship between the applied input voltage and the corresponding position extension. Experiments have been performed on the micro manipulator in order to quantify the effect of the nonlinear phenomena in the piezo-actuators. The experiments indicated that the main nonlinearities that need to be handled are hysteresis and the creep phenomenon, where the latter means that the extension of the piezo-actuator is increasing over time for constant input voltage. Results from experiments where the input voltages to the piezo-actuators were alternatingly increasing and decreasing are shown in Figure 3.2. It is obvious that the hysteresis needs to be handled actively for accurate positioning. It is also noted that the hysteresis is both rate and amplitude dependent. Further, experiments showed that the nonlinear creep phenomenon in the actuator is a much slower process, and thus easier to handle.

Although different in nature, both of these nonlinear effects can be reduced by using high-gain feedback. The control design will be described in Section 3.5. The nonlinear dynamics of the micro manipulator is further considered in Chapter 4.

Frequency Characterization of the Mechanical Design

In order to characterize the frequency properties of the mechanical design of the micro manipulator, several frequency response experiments have been performed. The frequency spectra in the different actuation directions, displayed in Figure 3.3, were estimated using the periodogram method. An important property of the system is the location of the first natural eigenfrequency. It is noted that the characteristics are quite different in the three Cartesian actuation directions. In particular, two natural eigenfrequencies are visible in the x- and z-axes, whereas only one is visible in the y-axis. The first eigenfrequency appears in the frequency range 33–47 Hz for all of the three axes.

The locations of the eigenfrequencies are important since they limit the achievable bandwidth—*i.e.*, the velocity that can be achieved in the position control loop—in the final closed-loop control system. Increasing the bandwidth beyond the resonance frequencies requires a lot of control actuation and the sensitivity to model errors becomes significant.

3.4 Modeling of the Mechanical Construction

In order to design position control algorithms, it is advantageous to perform modeling of the micro manipulator prior to the design. Two different methods for modeling can be chosen. As a first approach, modeling based on mechanical relations can be established, where the construction specific parameters are either analytically calculated or experimentally identified.

The other approach is to consider black-box input-output models without investigating the internal mechanical design. This is a common approach in model-based control, which results in satisfactory control performance given that the model captures the essential input-output dynamics of the system. This approach is investigated in this chapter for modeling of the linear dynamics of the micro manipulator.

Identification Based on Black-Box Models

Using system identification methods [Johansson, 1993], mathematical models describing the dynamics of the micro manipulator were determined. The axes can, in the modeling phase, be assumed to be decoupled provided that the mechanical design is made such that the motions of the different axes are sufficiently independent. During the dynamic characterization of the micro manipulator, minor cross coupling between the x- and z-axes was observed, which is further investigated using multi-input multi-output identification in the next section. However, since the influence of the coupling is minor, the assumption on decoupling was made in the subsequent model-based control design. Consequently, each axis is considered as a system with one input and

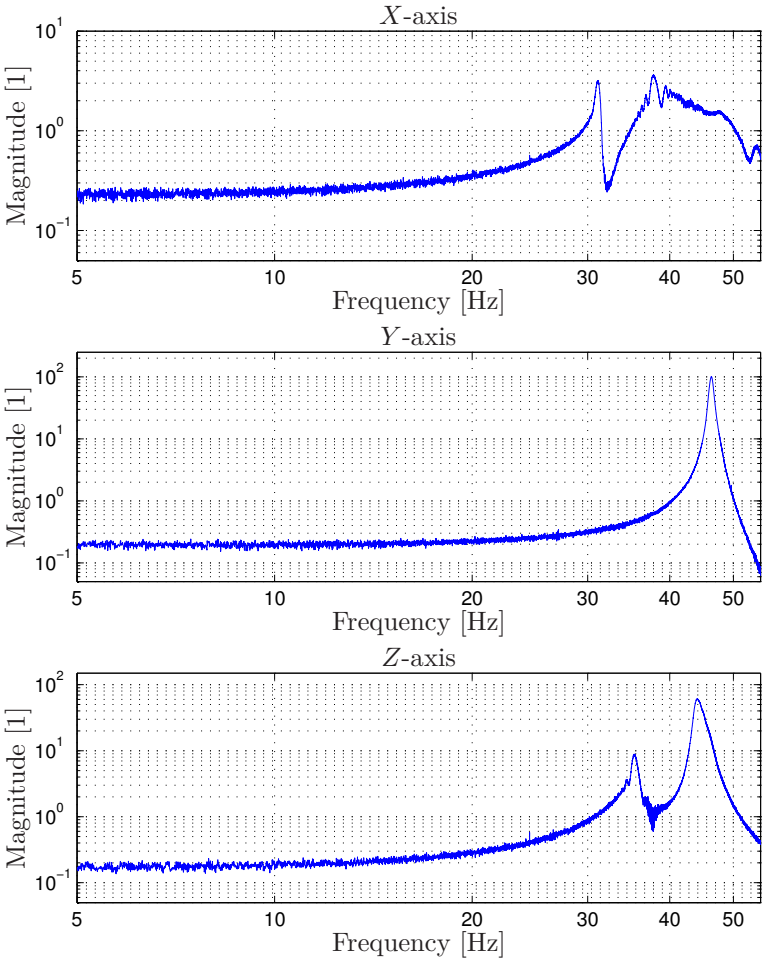

Figure 3.3 Estimated power spectral densities in the Cartesian actuation directions of the micro manipulator. The significant resonance frequencies occurring for the input-output dynamics along each of the axes are to be noted.

one output. Identification of the models was done in the System Identification Toolbox [Ljung, 2010] in MATLAB and the State-Space Model Identification (SMI) Toolbox [Haverkamp and Verhaegen, 1997] for identification of state-space models. Accordingly, consider discrete-time state-space models of the innovation form

$$\begin{cases} x_{k+1} &= \Phi x_k + \Gamma u_k + K e_k \\ y_k &= C x_k + D u_k + e_k \end{cases}, \tag{3.1}$$

where $u_k \in \mathbb{R}^m$ is the input, $x_k \in \mathbb{R}^n$ is the state vector, $y_k \in \mathbb{R}^p$ is the output, and e_k is a white-noise sequence. The system model matrices $\mathcal{S} : \{\Phi, \Gamma, C, D\}$ in the state-space representation are identified using one of the available implementations of subspace-based identification methods. In particular, the N4SID-method [Overschee and De Moor, 1994] and the MOESP algorithm [Verhaegen and Dewilde, 1992] were investigated for model identification in this thesis. During the identification of the models, the gain vector K in a Kalman filter [Kalman, 1960] for a minimum-variance estimate of the states in the model is also determined based on the noise properties of the identification data.

The subspace-based identification methods were found to result in models with superior fit to experimental data. In particular, the natural eigenfrequencies of the micro manipulator were identified with significantly higher accuracy with subspace-methods compared to identification of time-series models of autoregressive moving-average with exogenous input (ARMAX) type. For further details on time-series modeling, see, *e.g.*, [Madsen, 2008; Johansson, 1993].

Collection of Input-Output Data

The collection of experimental input-output data was performed in such a way that the input u_k was considered to be a scaled version of the input voltage to the piezo-actuator, whereas the output y_k was defined to be the Cartesian position of the micro manipulator end-effector, as measured by the capacitive sensor.

When performing system identification, an appropriate input signal has to be chosen, such that the system is excited properly. In this work, a chirp-signal was chosen—*i.e.*, a sinusoid with constant amplitude and linearly increasing frequency—as input, since this signal gives excitation in a well-defined frequency range. Consequently, the start and end frequencies of the chirp-signal have to be chosen based on the frequency range of interest. Given the frequency spectra displayed in Figure 3.3, a suitable range of excitation is 10–60 Hz, see Chapter 8 in [Johansson, 1993].

Preprocessing of the Data and Model-Order Selection

Prior to the identification, the input-output data was processed such that the mean and the linear trend were removed. In addition, the data, which was acquired at a sampling rate of 1 kHz, was low-pass filtered and subsequently decimated in order to avoid aliasing, to a sample rate of $1000/6 \approx 167$ Hz. This sampling frequency is suitable given the location of the eigenfrequencies of the dynamics in the different actuation axes.

MIMO Identification for Investigation of Cross-Coupling When performing identification of the state-space models for each axis of the micro manipulator, possible cross coupling dynamics between the axes is of interest. To this purpose, a single-input multi-output identification was made for investigation of the complete system model order. Here, the applied voltage to the piezo-actuator was considered as input—*i.e.*, only one axis was actuated at a time—whereas the measured positions of the respective Cartesian axis were considered as outputs. Hence, a single-input multi-output system is obtained where possible cross coupling between the axis is taken into account. The singular values related to the Hankel matrices of the experimental input and output data are calculated during the identification procedure using the N4SID or MOESP algorithms. By plotting these singular values in a diagram with logarithmic scale, the gap between the essential dynamics of the system and the noise level is identified. Based on this information, a sufficient order of the model can be chosen. The singular values plots for three experiments, with actuation in the respective Cartesian axis, are displayed in Figure 3.4. From the plot, it is clear that the resonances observed in the experimental data collected from the system make the singular values appear pairwise, corresponding to a pair of complex poles.

Identified Models for Control Design

Experimentally identified discrete-time state-space models of the form (3.1) for the dynamics in the x-, y-, and z-directions of the open-loop system were estimated. For the control design, single-input single-output models were considered. All models are of the same format. However, the model orders vary in the different actuation directions, reflecting the number of natural eigenfrequencies, *cf.* the frequency spectra in Figure 3.3. The determined model orders for the axes of the micro manipulator are 4, 2, and 5, for the x-, y-, and z-axis, respectively. The model order selection was based on a singular values analysis during the identification procedure, similarly to what was described in the previous paragraph. The frequency spectra of the identified models are shown in Figure 3.5. It is noted that there is good correspondence with the estimated periodograms in Figure 3.3. Further, the poles and zeros of the identified models in the x- and y-directions are displayed in Figure 3.6 and Figure 3.7, respectively. A measure of the fit of the models to the experimen-

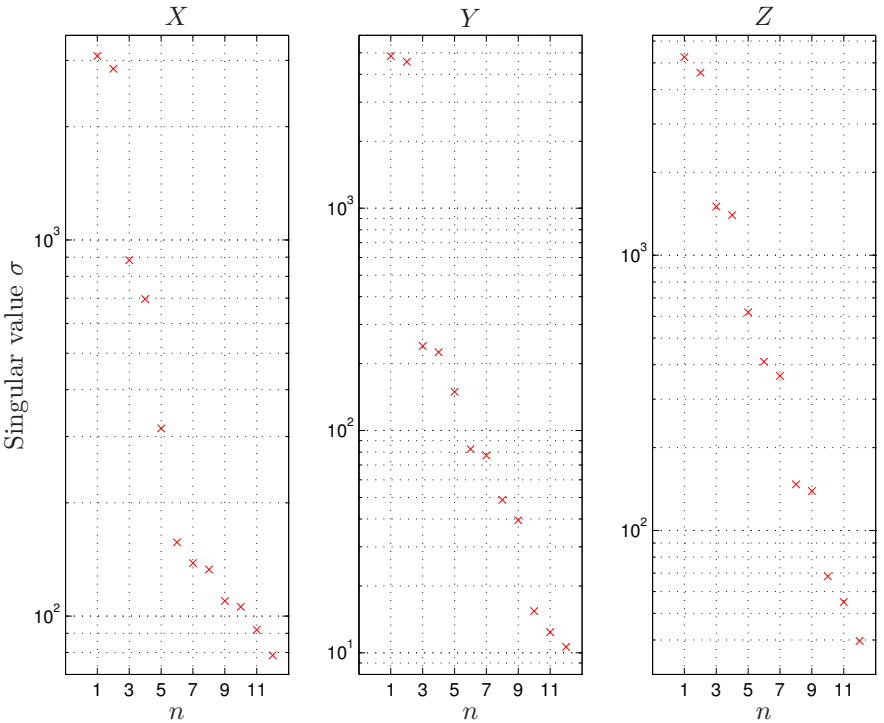

Figure 3.4 Singular value analysis of experimental data for single-input multi-output model identification of the micro manipulator dynamics. The three plots correspond to three different experiments, with actuation in the respective direction. When collecting the data, each axis was actuated while measuring the response along all three Cartesian axes. Using the singular values, the model order n of the system can be estimated.

tally collected identification data, is the *variance accounted for* (VAF) values, $\tau_{\text{VAF}} \in [0, 100]$. This quantity is, for an identification data series consisting of N measurements, defined as [Johansson, 1993]

$$\tau_{\text{VAF}} = \left(1 - \frac{(\mathcal{Y}_N - \hat{\mathcal{Y}}_N)^{\text{T}}(\mathcal{Y}_N - \hat{\mathcal{Y}}_N)}{\mathcal{Y}_N^{\text{T}}\mathcal{Y}_N}\right) \times 100, \tag{3.2}$$

where $\mathcal{Y}_N$ is a vector with the identification data and $\hat{\mathcal{Y}}_N$ is the corresponding vector with the model output data. This figure is 92.5, 99.5, and 97.1 for the identified models in the x-, y-, and z-directions, respectively. The obtained values indicate that the identified models capture the essential dynamics of the micro manipulator.

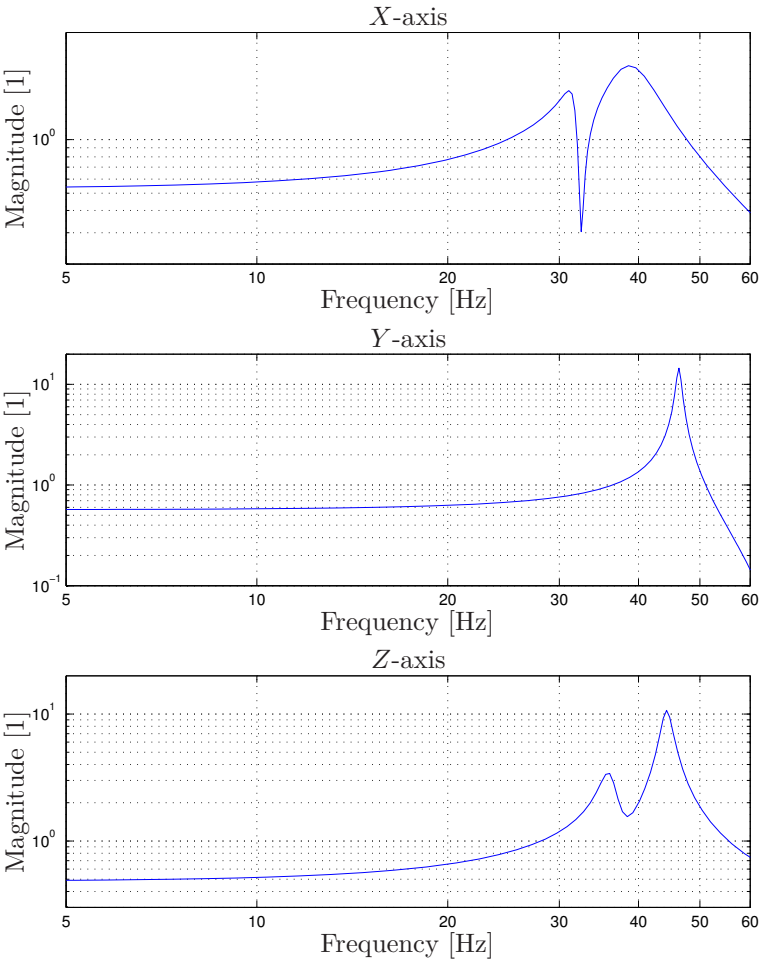

Figure 3.5 Bode diagrams of the discrete-time state-space models identified using subspace identification, for the dynamics along the x-, y-, and z-axes of the micro manipulator.

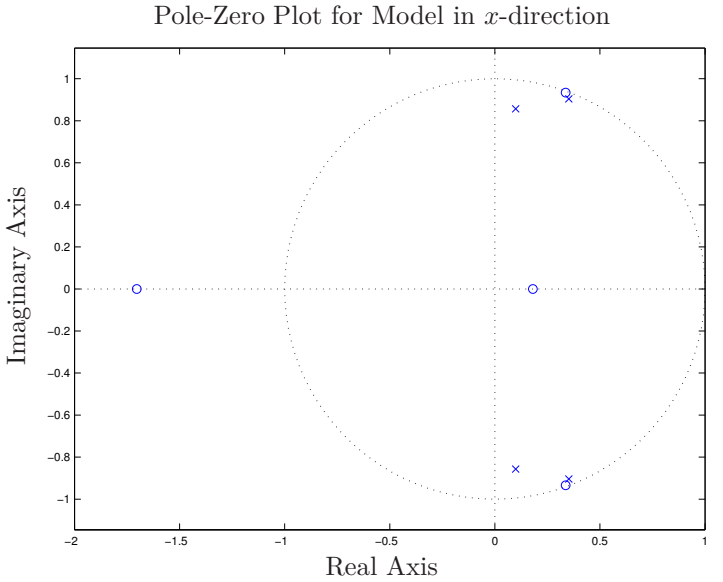

Figure 3.6 Poles and zeros of the identified model for the dynamics in the x-direction of the micro manipulator.

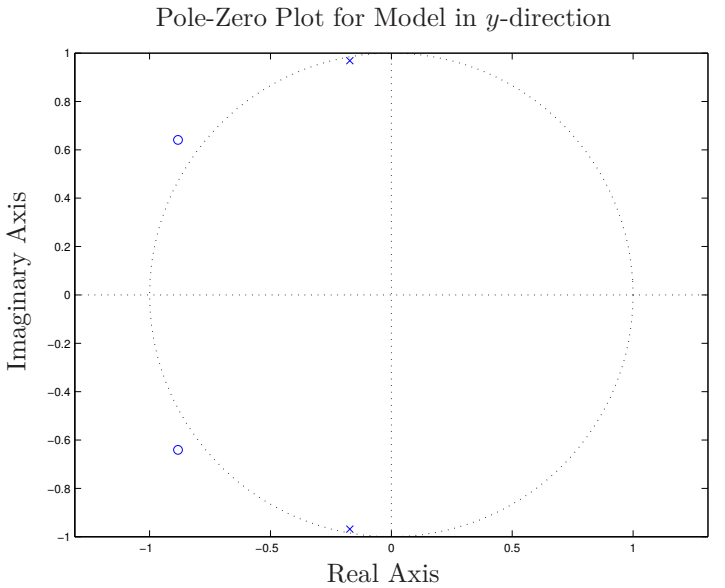

Figure 3.7 Poles and zeros of the identified model for the dynamics in the y-direction of the micro manipulator.

3.5 Position Control of the Micro Manipulator

The position control problem of the micro manipulator can be divided into two parts. First, the effects of the nonlinear dynamics in the piezo-actuators need to be reduced. Second, the oscillatory mechanical structure needs to be accurately position controlled. The specific control structure chosen in this thesis to handle these challenges is described next.

Inner Piezo-Actuator Control Loop

Two different approaches to control of nonlinear systems can be chosen: Model-based feedforward control and feedback control. Several methods and strategies for modeling of the nonlinear hysteresis dynamics and subsequent model-based control design have been discussed in the literature. Models such as the Prandtl-Ishlinskii model [Krasnosel'skii et al., 1989] and the Preisach model [Preisach, 1935] have been proposed, which is further investigated in Chapter 4 for the micro manipulator control design. However, as the extensions of the piezo-actuators in the micro manipulator are available for measurement with the strain gauge sensors, a more straightforward solution is investigated in a prototype version of the control architecture, where an inner feedback loop is closed around the nonlinear actuator. The prototype controller is a PID controller, with continuous-time transfer function according to

$$C(s) = K_p + \frac{K_i}{s} + \frac{sK_d}{1 + sK_d/N}, \tag{3.3}$$

where K_p, K_i, and K_d are controller parameters to be determined as part of the design procedure. The derivative part in the controller is low-pass filtered, in order to reduce the amplification of high-frequency noise contaminating the measured signal from the strain gauge sensors. Considering the intended application scenario for the micro manipulator—*i.e.*, milling tasks—disturbances from the cutting process are to be expected. The cut-off frequency in the low-pass filter is determined by the parameter N. The PID controller also has to be accompanied by an anti-windup scheme, to handle the case when the controller saturates the actuators. Discretization of the continuous-time controller (3.3) for subsequent implementation in a digital signal processor is straightforward, [Åström and Wittenmark, 1997].

In order to reduce the effects of the nonlinear dynamics in the piezo-actuators on the position control, the proportional gain K_p and the integral gain K_i should be increased as much as possible, while not resulting in too high sensitivity to disturbances occurring during the milling. Here, the derivative part is important since it contributes with lead compensation in the system. It will be shown by experimental results in Chapter 5 that this approach, combined with model-based feedforward described in Chapter 4,

results in satisfactory performance of the control of the piezo-actuators for the intended application. The performance is here measured by the position accuracy achieved in the milling task execution.

Model-Based Feedback Control of the Micro Manipulator

By utilizing the identified state-space models of the linear dynamics, a state feedback control loop can be designed for each of the three Cartesian actuation directions of the micro manipulator. However, new models need to be identified after closing the inner feedback control loop for the piezo-actuators, where the reference signal to the inner PID control loop is considered as the input signal instead. Since the difference compared to the open-loop models presented in the previous section is small, the models with the closed inner loop are not presented here.

State feedback is an appropriate control structure for this kind of systems, since damping of the resonant modes in the micro manipulator can be introduced in the construction by suitable control design. The control law for state feedback control of the system (3.1) is as follows

$$u_k = -Lx_k + u_{ff}, \tag{3.4}$$

where the controller parameter vector $L \in \mathbb{R}^n$ is to be chosen and u_{ff} is the feedforward control signal. The design procedure is to determine the parameter vector L by linear-quadratic (LQ) optimal control [Åström and Wittenmark, 1997], *i.e.*, such that the cost function

$$J(\mathcal{U}) = \sum_{k=1}^{\infty} x_k^{\mathrm{T}} Q x_k + u_k^{\mathrm{T}} R u_k, \tag{3.5}$$

where $\mathcal{U}$ is the sequence of control inputs, is minimized. Here, the matrices $Q \in \mathbb{R}^{n \times n}$ and $R \in \mathbb{R}^{m \times m}$ are user-defined weights in the optimization.

Since all states in the state-space axis models of the micro manipulator are not available for direct measurement, a Kalman filter [Kalman, 1960] is introduced for estimation of the states, based on the measured position signal, the system input, and the identified model. Consequently, the proposed control law is a Linear-Quadratic Gaussian (LQG) controller. The Kalman filter is organized as [Åström and Wittenmark, 1997]

$$\begin{cases} \hat{x}_{k+1} &= \Phi \hat{x}_k + \Gamma u_k + K(y_k - C\hat{x}_k) \\ \hat{y}_k &= C\hat{x}_k \end{cases}, \tag{3.6}$$

where the estimated states $\hat{x}_k$ and the estimated output $\hat{y}_k$ have been introduced and it was assumed that $D = 0$. Since the identified axis models are based on experimental data, where the mean are subtracted from the

original measured data, a *disturbance state* is added to the observer—*i.e.*, an additional constant state $\hat{x}_k^e$ with dynamics according to

$$\hat{x}_{k+1}^e = \hat{x}_k^e, \tag{3.7}$$

is introduced. By adding this state, the correct static gain for the estimation is achieved [Åström and Wittenmark, 1997]. The Kalman filter gain vector K for minimum-variance estimate of the states in the model is obtained from the identification procedure, since the noise model component is also included in the innovation model structure. In particular, the subspace-based identification methods employed provide the Kalman filter gain vector for each of the models. The corresponding pole placement—*i.e.*, equivalently the eigenvalues of the matrix $(\Phi - KC)$—is used also in the Kalman filter for the system with the disturbance state, but with one additional pole corresponding to the additional disturbance state $\hat{x}_k^e$.

The control law for the state feedback control is based on the estimated states according to

$$u_k = -L\hat{x}_k + u_{ff}. \tag{3.8}$$

In order to eliminate stationary errors in the position control loop, integral action is also introduced in the state feedback controller. This is done by extending the state vector with the integral state

$$x_i(t) = \int_0^t (r(\tau) - y(\tau))\mathrm{d}\tau, \tag{3.9}$$

where the position reference signal r has been introduced. With this extra state, it is also required that the state feedback vector L is augmented with one element, *i.e.*, $L_e = \begin{bmatrix} L & l_i \end{bmatrix}$, where l_i is the integral gain. Also, it is to be noted that the integral state needs to be discretized prior to design and subsequent implementation in a digital signal processing system.

Different approaches can be chosen to handle the feedforward control signal. In the scheme presented in this thesis, the feedforward control u_{ff} is chosen as a direct term from the reference signal, $u_{ff} = l_r r$. The parameter l_r determines the gain of the closed-loop system, and is chosen such that desired response to changes in the reference signal is obtained.

Tuning of Controller Parameters

In order to determine the state feedback vector L in the control law (3.8), the weight matrices Q and R in (3.5) for the LQ design need to be determined. Based on the identified models of the dynamics of the micro manipulator in the different actuation directions, each axis controller was tuned. Here, the dynamics in the y-direction is investigated as an example. The characteristics of the closed-loop system was determined for different weight matrices.

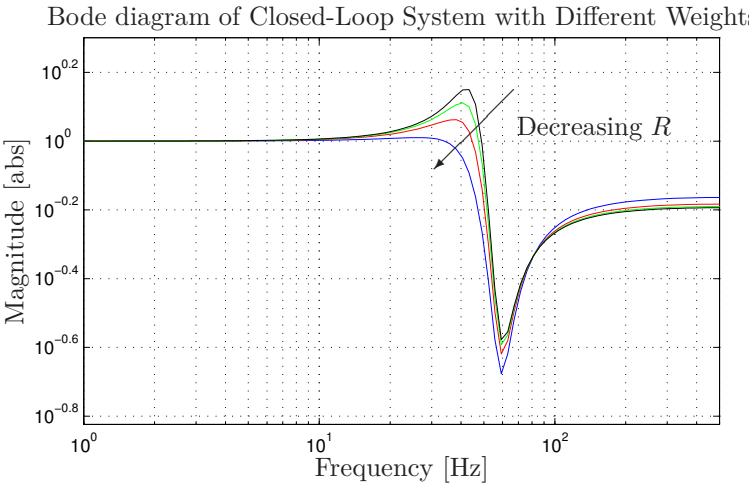

Figure 3.8 Bode diagram for the closed-loop system in the y-direction of the micro manipulator for $Q = I$ and different choices of the matrix R in the LQG design. The choices of R are in the set $\{1.0, 2.0, 3.0, 4.0\}$ for the blue, red, green, and black line, respectively.

In particular, the choice of the matrix R determines the control signal utilization. Bode diagrams for the closed-loop system for different choices of R, where the matrix Q has been chosen as the identity matrix, are displayed in Figure 3.8. It is to be noted that a lower weight results in a more aggressive controller, where the resonant mode in the system is well damped, at the cost of increased control signal utilization. Hence, the controller needs to be tuned as a trade-off between the attenuation of the poorly damped resonance in the system and the control signal utilization. A controller design with too aggressive tuning may result in unsatisfactory control performance, or even instability, when applied to the experimental setup, depending on the model accuracy.

Outlier Detection Scheme

In order to make the micro manipulator position controller more robust to unexpected large variations in the position measurements, an outlier detection scheme was implemented. Since optical tracking systems were utilized for online measurement of the robot end-effector position, the outliers in the current setup are mainly caused by aluminium chips emitted from the milling process, crossing the laser beam and resulting in a temporary deviation from the correct measurement. Even though the outliers are infrequent, they have to be handled actively in order to avoid surface inaccuracies in the workpiece to be machined. Consequently, an online outlier detection scheme with pre-

diction of measurements, see, *e.g.*, [Menold et al., 1999], was implemented in the control architecture. A measurement value is considered as an outlier if it deviates more than a certain threshold d from the median value of the M previous measurements. The predicted measurement is determined by a moving-average filter over the 10–20 previous measurements—*i.e.*, the predicted measurement $\hat{y}_k$ at time k is given by

$$\hat{y}_k = \frac{1}{N}(y_{k-1} + y_{k-2} + \ldots + y_{k-N}), \tag{3.10}$$

where N is the length of the moving-average filter.

Control Architecture

To the purpose of establishing a macro/micro manipulator configuration for milling with industrial robots, a control architecture including the micro manipulator position control law proposed in the previous section was developed. The proposed control architecture for the industrial robot and the micro manipulator is displayed in Figure 3.9. It consists of three main components; the robot controller, an optical tracking system, and the micro manipulator controller. Each of these components and its relation to the control architecture is discussed next.

Robot Controller The macro manipulator—*i.e.*, the industrial robot—is controlled by a conventional robot controller. The path to be tracked is planned offline using appropriate software and any position deviation of the robot from this path during the milling process is measured by an online tracking system and subsequently compensated for by the micro manipulator.

Tracking System and Path Deviation Measurement An optical system is utilized for tracking of the position of the workpiece. The workpiece is, in the proposed setup, held by the robot since the machining spindle is attached to the micro manipulator. As a prototype measurement system, laser-based sensors are utilized for tracking of the position of the workpiece. However, any optical tracking system with sufficient resolution and sample rate can be utilized. Sufficient resolution in this context is determined by the desired milling accuracy.

Micro Manipulator Controller The position of the workpiece, as measured by the tracking system, is compared to the nominal position calculated in the robot controller. Deviations from the nominal path are fed to the micro manipulator controller, *i.e.*, the reference value r_k at time step k for the micro manipulator is calculated as

$$r_k = p_k^d - p_k^m, \tag{3.11}$$

where p_k^d is the nominal path of the robot and p_k^m is the measured position of the robot end-effector at time step k.

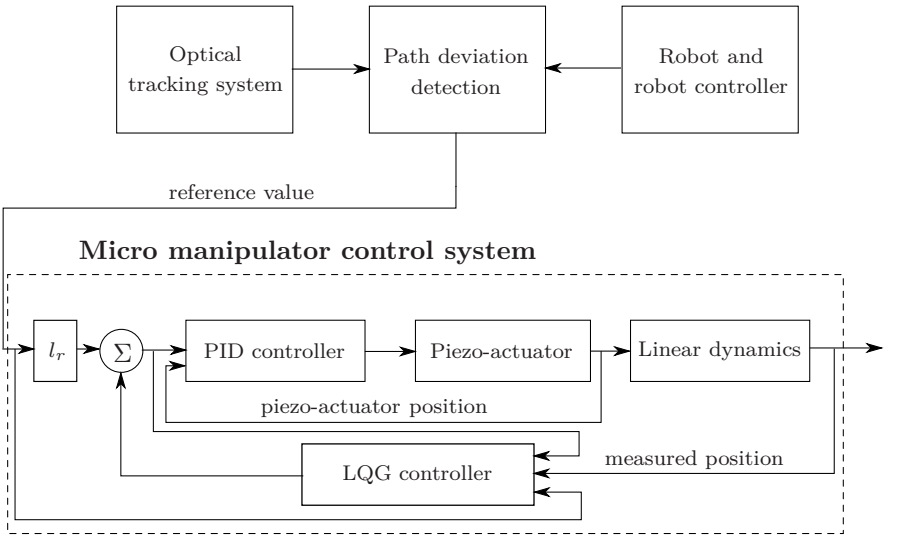

Figure 3.9 Control architecture for online compensation of position errors during milling tasks with industrial robots. The micro manipulator controller positions the machining tool based on the reference value calculated as the deviation of the workpiece, attached to the robot end-effector, from the nominal path.

Experimental Verification In order to verify the operation of the control architecture, a milling experiment with online compensation along the x-axis of the micro manipulator was performed. The results of the experiment are displayed in Figure 3.10. It is clear that the controller is working satisfactory in this experiment, with a control error below ± 10 µm. The control architecture is further validated in extensive milling experiments in Chapter 5.

3.6 Conclusions

In this chapter, a model-based position control architecture for a micro manipulator for milling tasks with industrial robots was proposed. Experimental data was collected, whereby models describing the linear dynamics of the system were determined. A control law based on a LQG controller was presented. Finally, a control architecture integrating the micro manipulator controller with the robot controller and an optical tracking system for arm-side measurements of the robot position was discussed. The chapter was concluded with experimental results obtained in a milling experiment with online compensation, verifying the operation of the control structure.

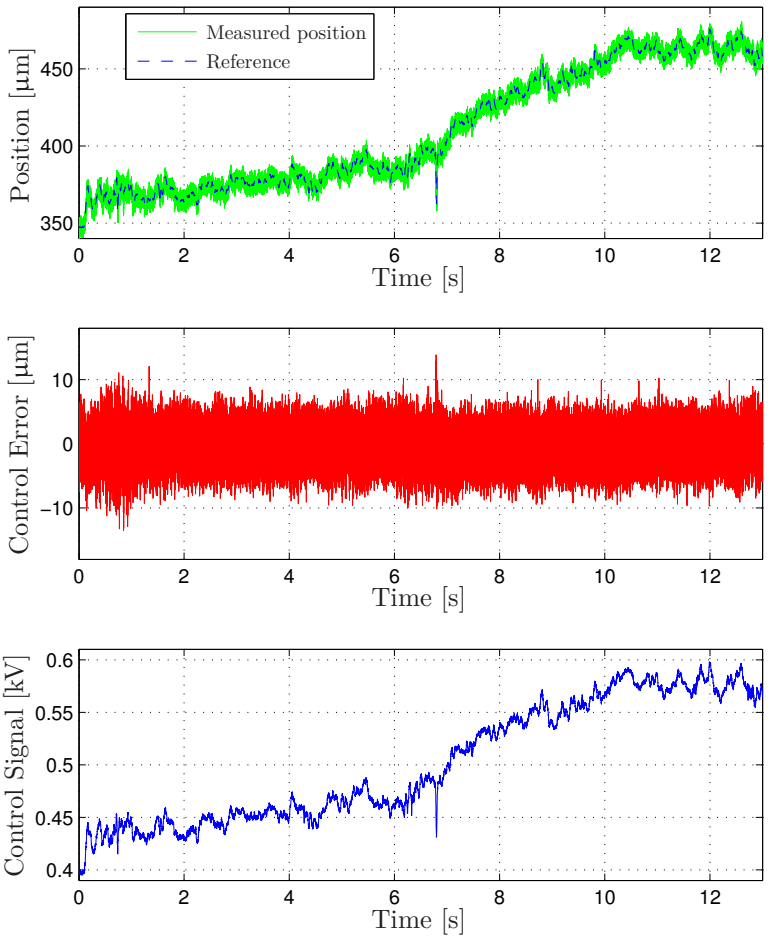

Figure 3.10 Experimental verification of the proposed control architecture in milling scenario with compensation along the x-axis of the micro manipulator. The control signal is the voltage applied to the piezo-actuator.

4

Nonlinear Model-Based Control of the Micro Manipulator

4.1 Introduction

As described in Section 3.3 in the previous chapter, the piezo-actuators in the micro manipulator exhibit nonlinear dynamics. Hence, it is plausible that explicit modeling of the nonlinear elements of the micro manipulator and subsequent model-based control can improve the positioning accuracy. The main contribution in this chapter of the thesis is the development and application of a model-based controller for the nonlinear dynamics of the micro manipulator, as well as an analysis of the proposed feedforward controller based on describing functions. Furthermore, an experimental verification showing a significantly higher accuracy of the position control with the proposed controller, compared to a linear controller based on pure feedback, is presented. This chapter of the thesis is based on the publication [Olofsson et al., 2012].

The structure of this chapter is as follows: In Section 4.2, a background to the investigated control problem is given. The theory for the nonlinear models of the piezo-actuators is given in Section 4.3, whereas the identified models and the controller for the nonlinear dynamics of the micro manipulator are presented in Section 4.4. Experimental results are presented and evaluated in Section 4.5, and finally a summary is provided and conclusions are drawn in Section 4.6.

4.2 Background

This section briefly reviews the nonlinear dynamics of the developed micro manipulator, so as to provide a basis for the control design. The micro ma-

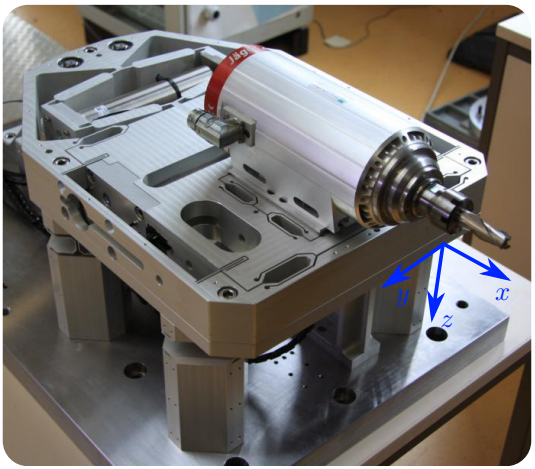

Figure 4.1 The micro manipulator actuated by three piezo-actuators, which exhibit nonlinear dynamics. The Cartesian coordinate system in blue indicates the actuation axes.

nipulator is displayed in Figure 4.1, together with its Cartesian actuation axes.

Nonlinear Phenomena in the Micro Manipulator

During the initial dynamic characterization of the micro manipulator—see Section 3.3 in the previous chapter—it was noted that the nonlinear dynamics in the piezo-actuators is significantly influencing the positioning accuracy. The most apparent nonlinear dynamics were *hysteresis* and *creep* effects. The characteristics of the former phenomenon were displayed in Figure 3.2. The creep effect has been quantified for the piezo-actuators in the different actuation axes to an approximate rate of 0.02 µm/s.

Consequently, modeling of the nonlinear hysteresis effect is beneficial in order to improve the accuracy of the position controller, which was proposed in the previous chapter for the micro manipulator. Since the creep phenomenon exhibits significantly slower dynamics than the hysteresis, this effect can be handled without explicit modeling. Instead, feedback from the strain gauge sensors on the actuators is utilized. In particular, integral feedback from the control error is considered.

4.3 Theory of Nonlinear Hysteresis Models

Several approaches to modeling of the hysteresis dynamics have been discussed in the literature. Three main categories of hysteresis models can be

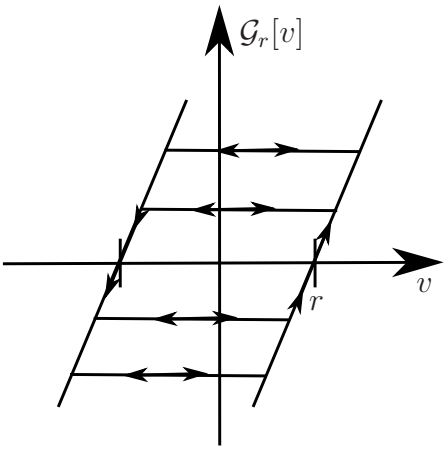

Figure 4.2 Play operator $\mathcal{G}_r[\cdot]$ with symmetric threshold r.

identified; approaches based on the *Preisach model* [Preisach, 1935; Ge and Jouaneh, 1996; Lei et al., 2011], the *Prandtl-Ishlinskii model* [Krasnosel'skii et al., 1989; Al Janaideh et al., 2009; Krejci and Kuhnen, 2001; Sun and Yang, 2009], and *neural networks* [Hastie et al., 2008; Xu, 1993].

In this thesis, the focus will be on the Prandtl-Ishlinskii model and the neural network approach for modeling of the nonlinear hysteresis dynamics from input voltage v to piezo-actuator position in the micro manipulator. Hence, the theoretical foundations of these approaches will be discussed next.

Prandtl-Ishlinskii Model

The Prandtl-Ishlinskii model is based on the play operator $\mathcal{G}_r[\cdot]$ depicted in Figure 4.2. Following [Brokate and Sprekels, 1996], a continuous function $v(t) \in \mathcal{C}[0,T]$, piecewise monotone in each of the subintervals

$$[t_i, t_{i+1}],\ 0 = t_0 < t_1 < \ldots < t_N = T, \tag{4.1}$$

is assumed as input. Hence, the play operator $\mathcal{G}_r[\cdot]$ can in each subinterval $[t_i, t_{i+1}],\ i = 0, \ldots, N-1$, be written as

$$\mathcal{G}_r[v](t) = \max(v(t) - r, \min(v(t) + r, \mathcal{G}_r[v](t_i))),\ t_i < t \leq t_{i+1}, \tag{4.2}$$

with the initial value

$$\mathcal{G}_r[v](0) = \max(v(0) - r, \min(v(0) + r, 0)). \tag{4.3}$$

Utilizing the definition of the play operator in (4.2), the Prandtl-Ishlinskii operator $\mathcal{H}[v](t)$ can be written as a superposition of play operators [Brokate

and Sprekels, 1996] according to

$$\mathcal{H}_1[v](t) = \alpha v(t) + \int_0^R \rho(r)\mathcal{G}_r[v](t)\mathrm{d}r, \tag{4.4}$$

where $\rho(r)$ is a positive density function and α is a constant parameter.

The *generalized Prandtl-Ishlinskii operator* [Al Janaideh et al., 2009], is an extension of the standard Prandtl-Ishlinskii operator (4.4) in that the input $v(t)$ is shaped with a continuous and strictly increasing function $\varphi(\cdot)$. The generalized Prandtl-Ishlinskii operator can be written as [Al Janaideh et al., 2009]

$$\mathcal{H}_2[v](t) = \alpha(\varphi \circ v)(t) + \int_0^R \rho(r)\mathcal{G}_r[\varphi \circ v](t)\mathrm{d}r. \tag{4.5}$$

To the purpose of implementation, a finite-dimensional Prandtl-Ishlinskii operator is established by discretization of the integral in (4.5). This results in the finite-dimensional Prandtl-Ishlinskii model

$$y_k = \alpha\varphi(v_k) + \sum_{i=1}^{n} \rho(r_i)\bar{\mathcal{G}}_{r_i}[\varphi(v_k)], \tag{4.6}$$

where $Y = \{y_k\}$ and $V = \{v_k\}$ are considered as discrete time-series and $\bar{\mathcal{G}}_{r_i}[\cdot]$ denotes the play operator acting on discrete-time input.

Inverse Model Based on Prandtl-Ishlinskii Operator

The advantage of using the Prandtl-Ishlinskii operator for modeling of the hysteresis dynamics is that the analytic inverse of the model (4.6) with a finite number of play operators exists. The inverse is given by, *e.g.*, [Al Janaideh et al., 2009],

$$v_k = \varphi^{-1}\left(\frac{1}{\alpha}y_k + \sum_{i=1}^{n} \hat{\rho}(\hat{r}_i)\bar{\mathcal{G}}_{\hat{r}_i}[y_k]\right), \tag{4.7}$$

where

$$\hat{r}_i = \alpha r_i + \sum_{j=1}^{i-1} \rho(r_j)(r_i - r_j) \quad \text{and} \tag{4.8}$$

$$\hat{\rho}(\hat{r}_i) = -\frac{\rho(r_i)}{\left(\alpha + \sum_{j=1}^{i} \rho(r_j)\right)\left(\alpha + \sum_{j=1}^{i-1} \rho(r_j)\right)}. \tag{4.9}$$

It is to be noted that the inverse of the shaping function $\varphi(\cdot)$ exists, which follows from the assumptions on $\varphi(\cdot)$ to be continuous and strictly monotone.

Neural Network Approach

Another approach to modeling of the hysteresis phenomenon is based on neural networks. In particular, neural networks with internal feedback from the output—referred to as *recurrent neural networks*—are of interest for modeling of the nonlinear hysteresis effect, since they capture the inherent memory effect.

Consequently, consider the recurrent neural network in Figure 4.3, which has been used for modeling of hysteresis in, *e.g.*, [Xu, 1993]. Define a discrete-time neural network with input

$$X_k = \begin{bmatrix} v_k & v_{k-1} & y_{k-1} \end{bmatrix}^{\mathrm{T}}, \tag{4.10}$$

output $Y_k = y_k$, one hidden layer, and M neurons. This neural network can be described at time k by the relations

$$Z_m = \sigma\left(\left(w_m^{(1)}\right)^{\mathrm{T}} X_k + b_m^{(1)}\right), \quad m = 1, \ldots, M, \tag{4.11}$$

$$Y_k = \sum_{m=1}^{M} w_m^{(2)} Z_m + b_m^{(2)}, \tag{4.12}$$

where $w_m^{(1)} \in \mathbb{R}^3$, $b_m^{(1)}, w_m^{(2)}, b_m^{(2)} \in \mathbb{R}$, and the activation function $\sigma(\cdot)$ has been chosen according to

$$\sigma(v) = \frac{1}{1 + \exp(-v)}. \tag{4.13}$$

After training of the network—*i.e.*, identification of the model parameters—with experimental input-output data, the neural network output represents the hysteresis model output.

Inverse Hysteresis Model Based on Neural Networks

To the purpose of feedforward control based on the nonlinear model of the hysteresis dynamics, a neural network can be utilized to model the inverse relation as well. By interpreting y_k as the input and v_k as the output, the inverse model can be established based on the recurrent neural network in Figure 4.3.

4.4 Model Identification

Hysteresis models were identified based on experimental input-output data. Since it is desirable that the model represents the hysteresis for different

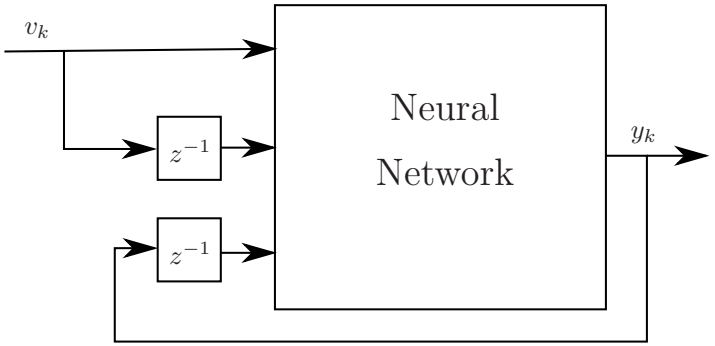

Figure 4.3 Recurrent neural network with internal feedback from the output y_k. The neural network is to model the hysteresis dynamics of the piezo-actuators in the micro manipulator from input voltage to position.

frequencies of the input signal, an excitation signal containing frequencies in the range of interest was chosen. Accordingly, the input signal

$$v(t) = v_0 + \sum_{k=1}^{n_v} a_k \sin(\omega_k t), \tag{4.14}$$

where v_0 is an offset and a_k and ω_k, $k = 1, \ldots, n_v$, are the amplitudes and frequencies of the sinusoids, was applied to the micro manipulator input—*i.e.*, the voltages applied to the piezo-actuators—for each actuation direction. An alternative excitation signal suitable for this kind of identification is a chirp signal.

Models Based on Prandtl-Ishlinskii Operator

The model parameters were identified by formulating a nonlinear optimization problem. The notation p is introduced for the set of model parameters to be identified. To the purpose of parameter identification, the following quadratic cost function is considered

$$J(p) = \sum_{k=1}^{N} (y_k - \hat{y}_k)^2, \tag{4.15}$$

where $\mathcal{Y}_N = [y_1, \ldots, y_N]$ is the identification data and $\hat{\mathcal{Y}}_N = [\hat{y}_1, \ldots, \hat{y}_N]$ is the corresponding model output. With the threshold values r_i of the play operators parametrized in the parameter β according to

$$r_1 = \beta, \; r_2 = 2\beta, \; \ldots \; , \; r_n = n\beta, \tag{4.16}$$

with $\beta > 0$, and the density function $\rho(r) = \gamma \exp(-\delta r)$ with $\gamma, \delta > 0$, several different models with n play operators were identified. In particular, the choice of the shaping function $\varphi(\cdot)$ is of importance in order to obtain good correspondence between experimental data and the model. The following shaping functions, common in the literature, were considered in this work

$$\varphi_1(v) = c_1 v + c_2, \tag{4.17}$$
$$\varphi_2(v) = c_3 \tanh(c_4 v + c_5) + c_6, \tag{4.18}$$

where $c_m,\ m = 1, \ldots, 6$, are model parameters to be identified from experimental data. For the affine shaping function, the following set of parameters are to be identified

$$\mathcal{M}_{\mathrm{PI,a}} \ : \ p = \{\alpha, \beta, \delta, \gamma, c_1, c_2\}\,, \tag{4.19}$$

and for the model with the hyperbolic tangent shaping function, the parameters are

$$\mathcal{M}_{\mathrm{PI,b}} \ : \ p = \{\alpha, \beta, \delta, \gamma, c_3, c_4, c_5, c_6\}\,. \tag{4.20}$$

The selection criterion for the choice of shaping function was the final cost $J(p^*)$, where p^* is the vector of parameter values minimizing $J(p)$.

The output from the identified model of the hysteresis nonlinearity in the x-axis of the micro manipulator, with the shaping function $\varphi_2(v)$ in (4.18) and $n = 6$, is compared to the measurements from the experimental setup in Figure 4.4. It is to be noted that the model exhibits a good fit to the experimental data and that the input-output relation for the input signal of choice is satisfactory. The corresponding models for the dynamics in the y- and z-axes are similar, and are therefore not presented here.

Models Based on Recurrent Neural Network

Hysteresis models based on the recurrent neural network were trained using the cost function in (4.15) and with stochastic initialization of the model parameters

$$\mathcal{M}_{\mathrm{NN}} \ : \ \left\{ b_m^{(1)}, b_m^{(2)}, w_m^{(1)}, w_m^{(2)} \ , \ m = 1, \ldots, M \right\}, \tag{4.21}$$

based on a Normal distribution. A model for the nonlinearity in the x-axis with $M = 25$ neurons was found to result in similar performance as the previous Prandtl-Ishlinskii model. The model output and corresponding experimentally collected data for the x-axis nonlinearity are displayed in Figure 4.5. Further, a neural network was trained for the inverse of the nonlinearity, which can be utilized to the purpose of feedforward control.

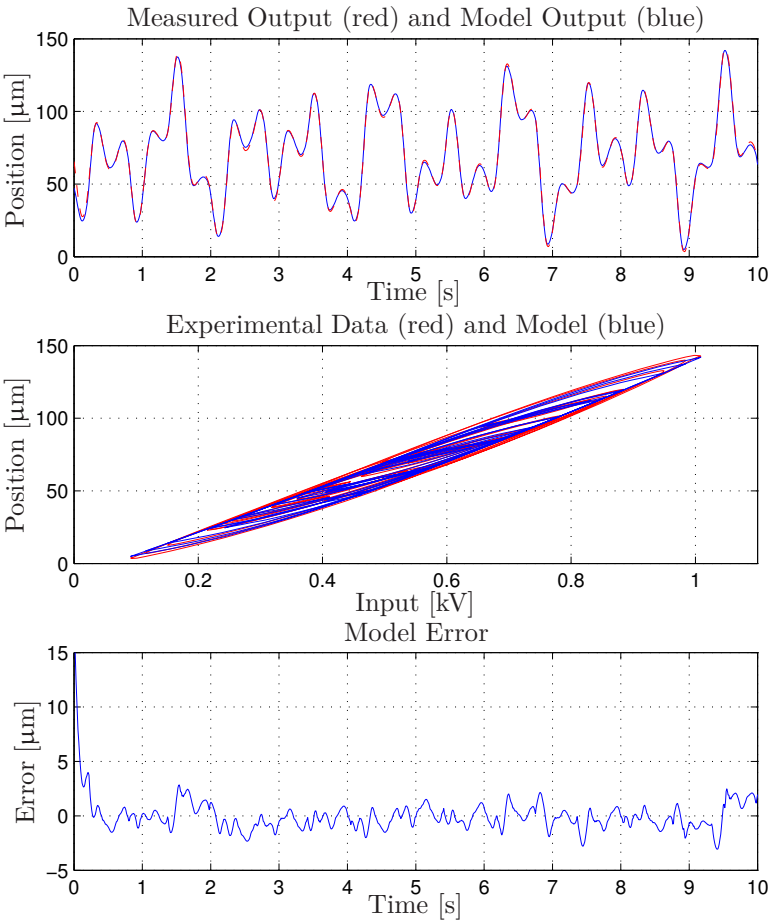

Figure 4.4 Model based on Prandtl-Ishlinskii operator with output as function of time (upper panel), output as function of input (middle panel), and model error (lower panel).

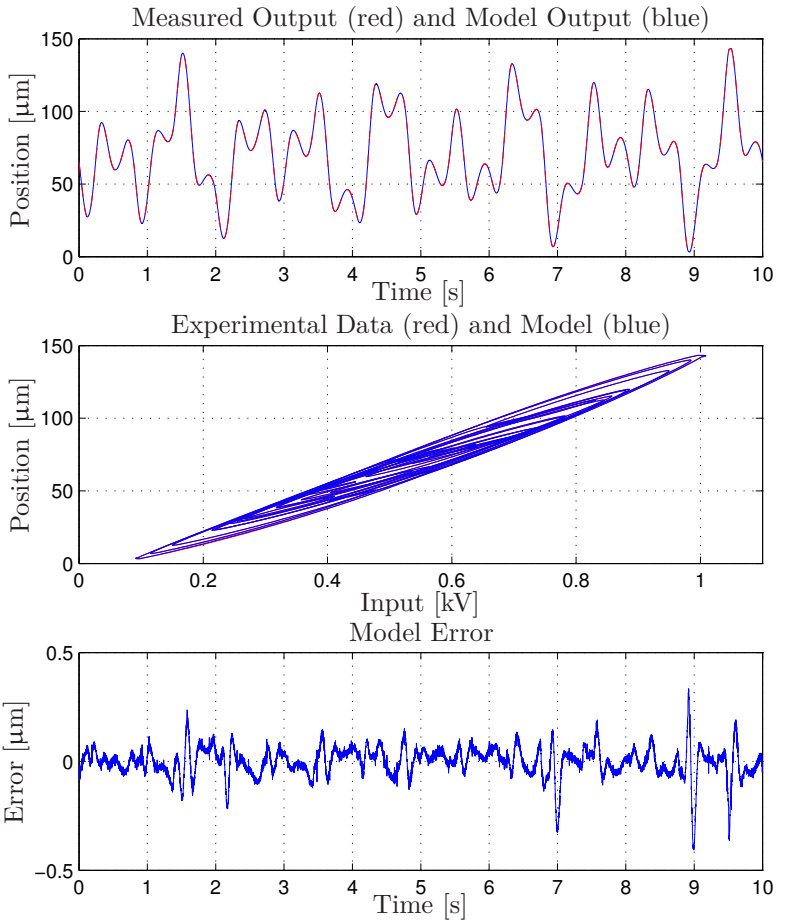

Figure 4.5 Model based on recurrent neural network with output as function of time (upper panel), output as function of input (middle panel), and model error (lower panel).

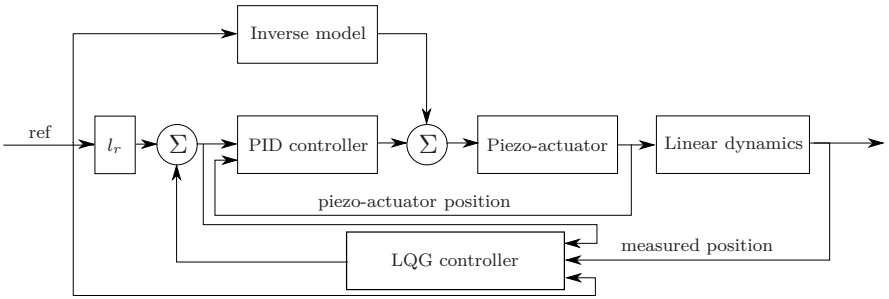

Figure 4.6 Controller diagram for position control of each axis of the micro manipulator, *cf.* Figure 3.9 in Chapter 3. The reference signal to the position controller is determined by an optical robot tracking system, measuring the deflections of the end-effector of the robot during the machining task.

Scheme for Position Control

The control diagram depicted in Figure 4.6 is proposed. This scheme is an extension of the controller presented in Figure 3.9 in the previous chapter, where the nonlinear dynamics of the piezo-actuators is explicitly modeled and subsequently compensated for with feedforward control. In the controller development, each of the Cartesian axes of the micro manipulator is considered separately, *i.e.*, possible cross couplings between the axes are neglected also in the nonlinear feedforward control.

Inner Controller for Piezo-Actuators

Based on the inverse of the previously identified models of the hysteresis nonlinearity in the micro manipulator, a combined feedforward and feedback controller is proposed. A feedforward controller alone is not sufficient, since unmodeled dynamics, parameter uncertainty in the model, and time-variations in the dynamics will degrade the performance significantly. Consequently, feedback from the strain gauge sensors attached to the piezo-actuators is necessary as a complement to the feedforward controller.

The feedforward controller is based on the inverse of the hysteresis nonlinearity in the micro manipulator. The inverse model is established for each Cartesian axis as described in Section 4.3; either from the model based on the Prandtl-Ishlinskii operator or training a neural network for the inverse relationship of the nonlinearity directly.

The feedback controller is chosen as a PID controller, see transfer function (3.3) in Chapter 3. The D-part is essential in systems with hysteresis, since it acts as a lead compensator. Furthermore, the D-part is low-pass filtered in order to avoid amplification of high-frequency noise and the I-part

is accompanied by an anti-windup scheme to avoid degraded performance in case of actuator saturation.

Describing Function Analysis of the Feedforward Controller

In order to analyze the properties of the feedforward controller based on the Prandtl-Ishlinskii operator, *describing function analysis*, see, *e.g.*, [Krylov and Bogoliubov, 1947; Slotine and Li, 1991; Khalil, 2002], is utilized. The describing function analysis is based on a Fourier series expansion of the output from the nonlinear model, with a sinusoidal input. Even though this is an approximate analysis in the frequency domain, it gives valuable information about the global behavior of the feedforward controller. The analysis can further be motivated by considering the fact that the linear dynamics of the micro manipulator is of low-pass character.

Consider the finite-dimensional inverse Prandtl-Ishlinskii model in (4.7). Further, assume continuous-time input and output. With the input

$$y(t) = y_0 + A\sin(\omega t), \tag{4.22}$$

the offset term v_0 and the coefficients a_1, b_1 for the first-order harmonics in the Fourier series expansion of the output are given by

$$v_0 = \frac{1}{2\pi}\int_0^{2\pi} f(y(t))\mathrm{d}(\omega t), \tag{4.23}$$

$$a_1 = \frac{1}{\pi}\int_0^{2\pi} f(y(t))\sin(\omega t)\mathrm{d}(\omega t), \tag{4.24}$$

$$b_1 = \frac{1}{\pi}\int_0^{2\pi} f(y(t))\cos(\omega t)\mathrm{d}(\omega t), \tag{4.25}$$

where $f(\cdot)$ is the inverse hysteresis model mapping. The describing function $N(A)$ is defined based on the a_1 and b_1 coefficients as

$$N(A) = \frac{a_1 + ib_1}{A}. \tag{4.26}$$

Further, introduce $\theta_i = \pi - \arcsin(1 - (2\hat{r}_i)/A)$ and

$$\Gamma_i = \begin{cases} 1\ , & \text{if } A > \hat{r}_i \\ 0\ , & \text{otherwise} \end{cases}. \tag{4.27}$$

The derivation of the describing function is made by assuming that the shaping function $\varphi(v) = 1$ and $y_0 = 0$. It is straightforward to verify that $v_0 = 0$.

The a_1 coefficient can, after simplification, be written as

$$\frac{a_1}{A} = \frac{1}{\alpha} + \frac{1}{\pi}\sum_{i=1}^{n} \hat{\rho}(\hat{r}_i)\Gamma_i \Bigg\{ \frac{3\pi}{2} + \frac{1}{2}\sin(2\theta_i) + 2\left(\frac{2\hat{r}_i}{A} - 1\right)\cos(\theta_i) - \theta_i \Bigg\}. \quad (4.28)$$

A similar calculation for the b_1 coefficient gives

$$\frac{b_1}{A} = \frac{1}{\pi}\sum_{i=1}^{n} \hat{\rho}(\hat{r}_i)\Gamma_i \Bigg\{ -\frac{3}{2} + \frac{1}{2}\cos(2\theta_i) + 2\left(1 - \frac{2\hat{r}_i}{A}\right)\sin(\theta_i) \Bigg\}. \quad (4.29)$$

Hence, the quantity

$$|N(A)| = \frac{\sqrt{a_1^2 + b_1^2}}{A}, \quad (4.30)$$

can be utilized as a measure of the amplitude-dependent gain.

The analysis can be extended to the case when $\varphi(\cdot)$ is a different function than the unity mapping and $y_0 \neq 0$. However, if the complexity of the shaping function is increased, calculation of the required integrals has to be performed using numerical quadrature. The describing function analysis is performed for the model presented in Figure 4.4 with the shaping function $\varphi_2(v)$ in (4.18), whereby the offset and gain shown in Figure 4.7 are obtained. In this analysis, the offset in the input signal has been chosen to $y_0 = 70$, which is in the middle of the working range of the piezo-actuators in the micro manipulator.

It is to be noted that no singularities are visible in the describing function within the amplitude range of interest, which is defined by the working range of the different actuation axes of the micro manipulator. Hence, the describing function analysis indicates stability of the feedforward controller based on the inverse Prandtl-Ishlinskii model.

4.5 Experimental Results

To the purpose of experimental verification of the proposed control law for the piezo-actuators, the feedforward controller based on the Prandtl-Ishlinskii operator, was implemented and tested on the experimental setup with the micro manipulator. In the experiments, the LQG controller with feedback from the end-effector position was not active, since the purpose was to evaluate the inner piezo-actuator controller with the model-based feedforward.

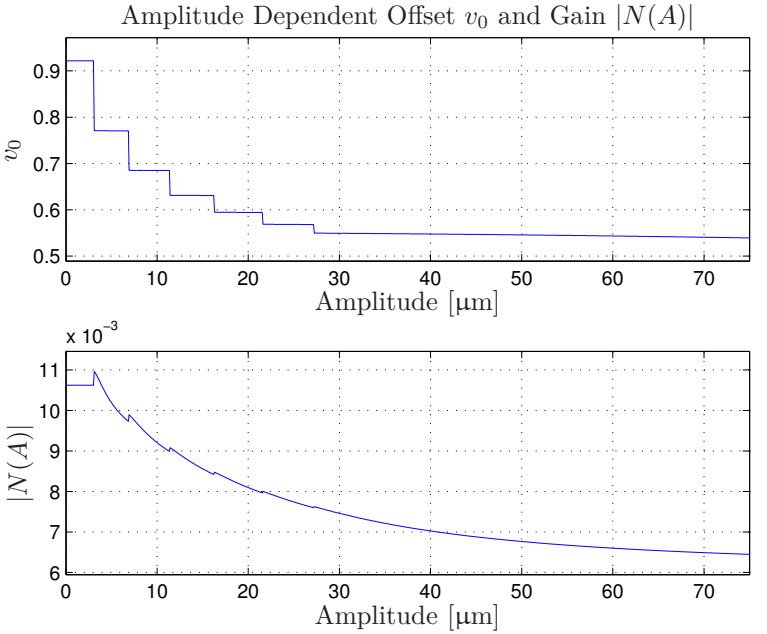

Figure 4.7 Amplitude dependent offset v_0 and gain $|N(A)|$ for the inverse of the hysteresis model in Figure 4.4, calculated using describing function analysis. The discrete character of the inverse model is clearly visible in the plots, where the stairs correspond to the threshold values $\hat{r}_i,\ i = 1, \ldots, n$.

Experimental Setup

The micro manipulator was interfaced *via* a dSPACE DS1103 controller board [dSPACE GmbH, 2007], where the sensor signals were read and the actuator signals were written. The control architecture was implemented in MATLAB Simulink, and then translated to C-code and compiled. The controller was installed in the dSPACE system and executed at a sampling frequency of 10 kHz. The experimental setup is further described in Chapter 5.

Experimental Verification of Controller

The x-axis of the micro manipulator was chosen for evaluation of the proposed controller for the piezo-actuators. The results for the other axes were similar, and are therefore not presented here. The reference signals applied to the experimental setup were of the format

$$v(t) = v_0 + A\sin(2\pi f t), \tag{4.31}$$

where the frequency f was chosen to 1, 5, and 10 Hz, which are frequencies in the range of interest for the intended application. The amplitude and offset, measured on the actuator side of the micro manipulator, were chosen to $A = 30$ µm and $v_0 = 70$ µm, respectively, which means that the major part of the working range of the actuator is covered. The evaluation was performed with the following configurations of the position controller for the piezo-actuator:

A. Pure feedback control using PID control.

B. PID controller combined with feedforward control based on the Prandtl-Ishlinskii model with the affine shaping function $\varphi_1(\cdot)$ in (4.17).

C. PID controller combined with Prandtl-Ishlinskii model with hyperbolic tangent shaping function $\varphi_2(\cdot)$ in (4.18).

Further, for reasons of comparability, the parameter tuning of the PID controller was identical in the different configurations. The controller parameters were chosen such that the gain was increased as much as possible, given robustness to process disturbances. As a measure of the position control accuracy, the control error—*i.e.*, the difference between the desired position of the piezo-actuator and the measured position—was considered. The control errors for the experiments performed on the setup, with the controller configurations and reference signals discussed in the previous paragraph, are displayed in Figure 4.8. The corresponding input-output behavior is displayed in Figure 4.9. Furthermore, the maximum peak-to-peak error e_m as well as the standard deviation σ_e of the control error are shown in Table 4.1 for the different reference signals. Observing the results in Table 4.1 closer, it is clear that the accuracy of the position control is significantly improved using the proposed feedforward controller. Further, the performance of the feedforward controller with the affine shaping function and the hyperbolic tangent shaping function is similar for the investigated input signals. The high-frequency oscillations which can be observed in the response can be derived to the eigenfrequencies of the piezo-actuators. The eigenfrequency of the unloaded piezo-actuator is 2.6 kHz. Taking the loading of the piezo-actuator into account, the measured frequency of approximately 340 Hz agrees well with the observations made in the experimental data. Further, considering the maximum error and standard deviation for the control error in Table 4.1, it can be noted that the feedforward controller based on the Prandtl-Ishlinskii model with hyperbolic tangent shaping function performed slightly better than the corresponding model with affine shaping function for some of the reference signals.

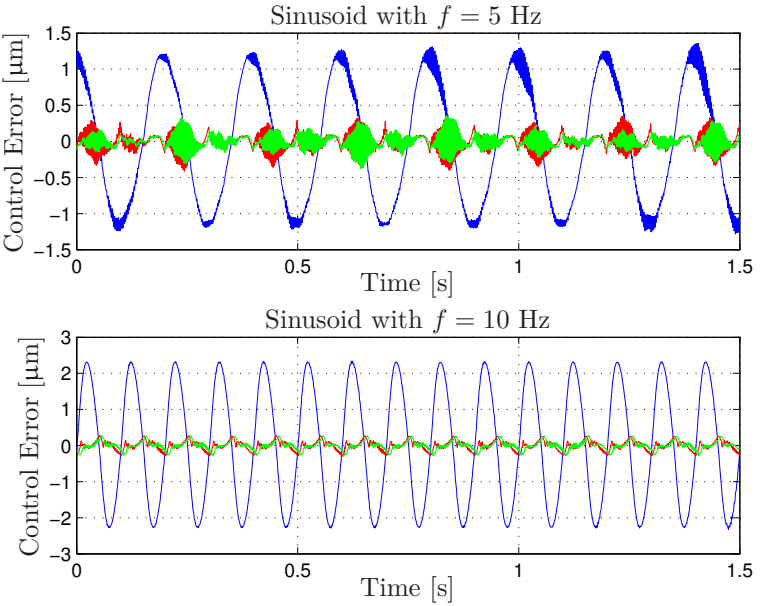

Figure 4.8 Experimental control error for PID controller (blue), Prandtl-Ishlinskii model with affine shaping function (red), and Prandtl-Ishlinskii model with hyperbolic tangent shaping function (green), all with sinusoidal reference signal with frequencies 5 Hz (upper panel) and 10 Hz (lower panel).

4.6 Conclusions

This chapter considered the problem of increasing the positioning accuracy of the micro manipulator by utilizing model-based nonlinear control. Explicit nonlinear models of the major nonlinearity in the manipulator—*i.e.*, the hysteresis dynamics in the piezo actuators—were identified based on experimental data. Two model categories were considered; models based on the Prandtl-Ishlinskii operator and models based on recurrent neural networks. A subsequent control architecture was proposed, where the properties of the feedforward control was analyzed using describing functions.

In an experimental verification, the identified models were utilized in a controller combining feedforward and feedback strategies. Experimental results from the setup showed that the proposed controller for position control of the piezo-actuators increases the accuracy significantly for reference signals with different frequencies, compared to a linear controller. For a sinusoidal input with frequency 10 Hz, the maximum and the standard deviation of the control error were reduced by a factor of approximately ten.

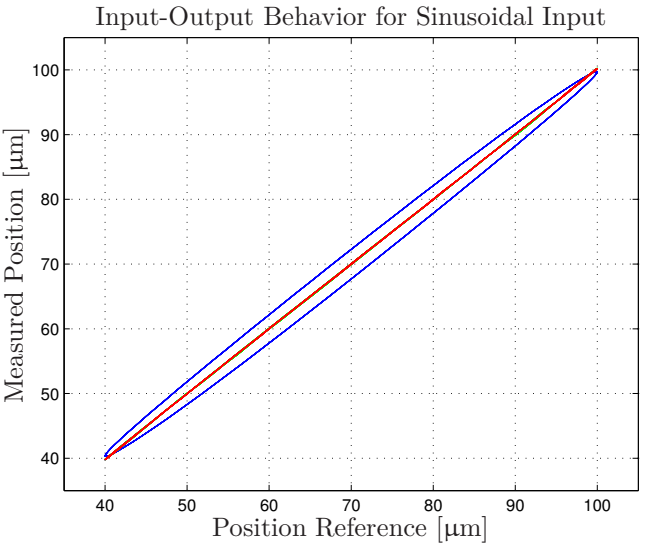

Figure 4.9 Experimental input-output behavior for PID controller (blue), Prandtl-Ishlinskii model with affine shaping function (red), and Prandtl-Ishlinskii model with hyperbolic tangent shaping function (green), all with sinusoidal reference signal with frequency 10 Hz.

Table 4.1 Maximum error e_m and standard deviation σ_e of control error for the different configurations of the controller for the piezo-actuators in the micro manipulator.

Maximum Error e_m [µm]

	Configuration		
Input freq. [Hz]	**A**	**B**	**C**
1	0.83	0.51	0.53
5	2.7	0.82	0.74
10	4.7	0.59	0.59

Standard Deviation σ_e [µm]

	Configuration		
Input freq. [Hz]	**A**	**B**	**C**
1	0.17	0.063	0.063
5	0.84	0.13	0.11
10	1.6	0.13	0.12

5

Experimental Verification of the Micro Manipulator

5.1 Introduction

To the purpose of experimental verification and evaluation of the proposed position control architecture for the micro manipulator in Chapter 3, several milling tasks were executed with online position error compensation. The surface quality achieved with and without compensation is compared and evaluated. This chapter of the thesis is based on the publications [Olofsson et al., 2011a] and [Sörnmo et al., 2012].

The structure of this chapter is as follows: The experimental setup with the robot and the micro manipulator and their interfaces are described in Section 5.2. Section 5.3 presents the results from the performed milling tasks. The achieved experimental results are evaluated in Section 5.4. Further, based on the presented results, a discussion of the results and the proposed control architecture and setup for machining tasks are provided in Section 5.5. Finally, conclusions are drawn in Section 5.6.

5.2 Experimental Setup

The experimental evaluation was performed using a REIS industrial robot of model RV40 [Reis GmbH, 2011], with a maximum payload of 40 kg. The machining spindle was attached to the micro manipulator and the robot held the workpiece, which in the present experimental verification was a block of aluminium of type AlMg3,5. The setup was such that both face milling and peripheral milling, also referred to as radial milling, could be performed, see Figure 2.9 in Chapter 2. It is to be noted that these two strategies for milling are not equivalent, since the required cutting forces are different in magnitude and direction and hence affect the robot differently. Consequently, both face and peripheral milling experiments were performed in this evaluation.

Interface and Sensors

The micro manipulator was interfaced with a dSPACE controller board of model DS1103 [dSPACE GmbH, 2007], where all sensor signals from the micro manipulator are read and the signals to the actuators from the controller are sent. The developed controllers were executed in the controller board at a sampling frequency of 10 kHz. The controllers were implemented in MATLAB Simulink and C-code was automatically generated by the Real-Time Workshop toolbox [MathWorks Inc. 2010]. The compiled C-code was then executed in the dSPACE system.

To the purpose of measuring the deflections of the robot in the milling direction—*i.e.*, the deflections which were to be compensated by the micro manipulator—a Keyence laser sensor of model LK-G87 [Keyence Corp. 2006], with a resolution of 0.2 μm and a sampling frequency of 10 kHz was used as a prototype tracking system. This sensor is based on the interferometer principle for measuring the distance to the aluminium workpiece attached to the robot.

Compensated and Uncompensated Milling

In order to illustrate the benefit of the micro manipulator, the milling experiments were performed both in a setting where compensation with the micro manipulator was utilized and in a setting with the spindle rigidly attached to a fixed base—*i.e.*, in the latter setup no compensation was performed. The two experimental settings are illustrated in Figure 5.1.

In the experiments without compensation, the robot configuration was mirrored, with respect to the center plane of the robot, compared to the configuration chosen in the experiments with compensation. Consequently, the compliance properties of the robot in the two configurations are equivalent. Mirroring is important in order to make the compensated and uncompensated milling results comparable, since the Cartesian compliance exhibits a configuration dependency.

5.3 Experimental Results

With the experimental setup described in Section 5.2, milling in a rectangular block of aluminium was performed. The industrial robot can be reconfigured such that milling can be executed in all three directions of the micro manipulator. Results obtained during face milling in the x actuation direction and peripheral milling in the y and z actuation directions of the micro manipulator are presented in this thesis. The experiments were performed with a material feed-rate of 7.5 mm/s, a spindle speed of 28 000 rpm, and a depth-of-cut of 1 mm in the face millings and 1×10 mm in the peripheral millings.

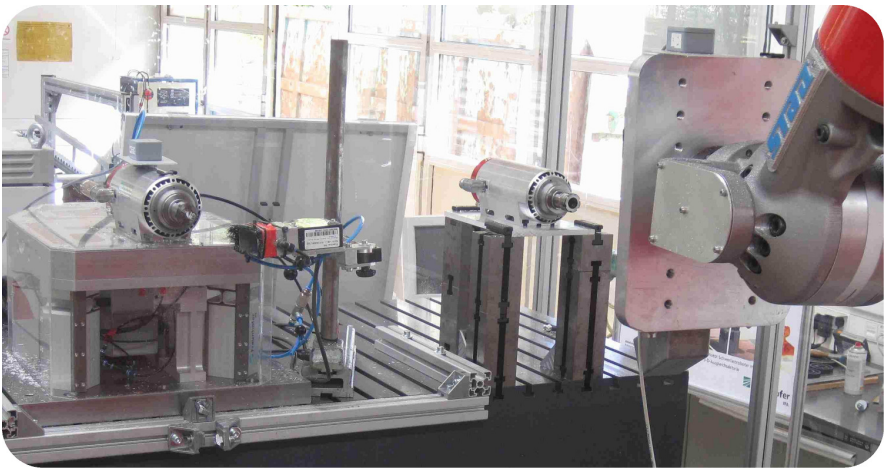

Figure 5.1 Experimental setup at Fraunhofer IPA, Stuttgart, Germany, for evaluation of the performance of the proposed micro manipulator and position control architecture. The micro manipulator is seen to the left. The machining spindle to the right is rigidly attached to the base. The latter setup is utilized for milling experiments without compensation.

Milling Experiments with Compensation

First, a set of milling experiments with online position compensation, utilizing the micro manipulator, was performed. Each of the experiments in the different actuation axes of the micro manipulator is described next.

***X*-direction** In the first setting, a face milling is performed, where the surface orthogonal to the x-axis of the micro manipulator is to be machined. Consequently, the micro manipulator is controlled in this direction. The result of the milling experiment is displayed in Figure 5.2. The control error is defined as the difference between the reference value to the micro manipulator control system and the measurement from the capacitive sensor measuring the position of the micro manipulator in the x-direction.

***Y*-direction** The milling accuracy has further been tested in a peripheral milling experiment, where the compensation was performed along the y-axis of the micro manipulator. It should be noted that this milling task is different from the face milling presented in the previous paragraph, in the sense that the process forces affect the robot differently.

Moreover, the experiment is designed such that the robot, on purpose, is not moving perpendicularly to the compensation direction. This situation can be considered as a result of a poorly calibrated workpiece or industrial robot. By utilizing the micro manipulator, this effect can be compensated for

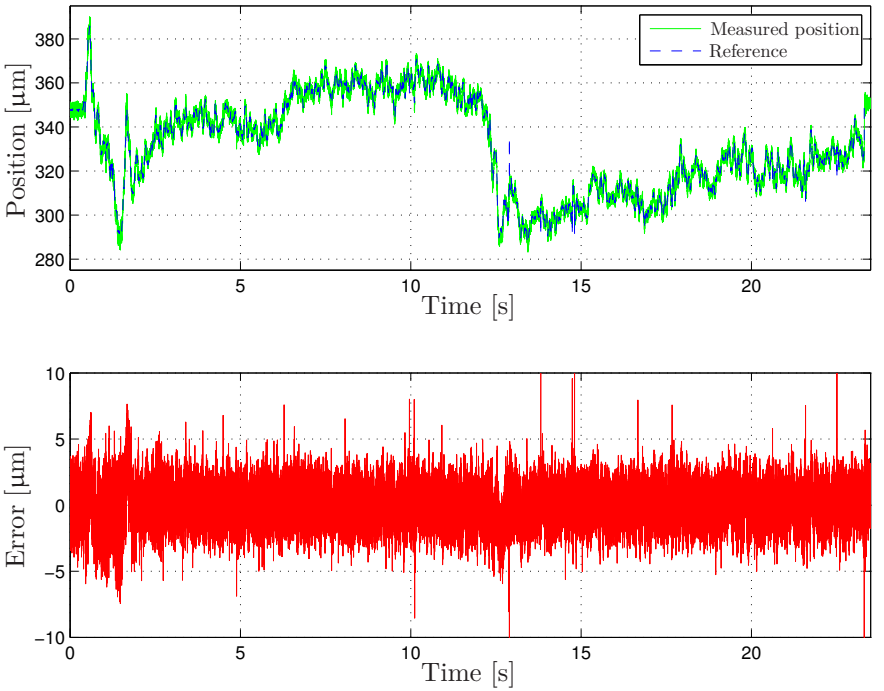

Figure 5.2 Reference value and measured position of the micro manipulator during face milling experiment with compensation along the x-direction (upper panel) and corresponding control error (lower panel).

online, since the motion of the robot is tracked in real-time using the optical tracking system.

The result of the milling experiment is displayed in Figure 5.3. The control error displayed is defined analogously to the case with face milling in the x-direction of the micro manipulator.

***Z*-direction** The third experiment performed was a peripheral milling with compensation along the z-axis of the micro manipulator. The experiment is similar to the one discussed in the previous paragraph; however the compensation is performed along another axis of the micro manipulator and in addition the configuration of the robot is different. The control performance of the micro manipulator in the milling experiment is displayed in Figure 5.4.

Milling Experiments Without Compensation

The same milling experiments described and presented in the previous subsection were repeated, but with the machining spindle rigidly attached to a

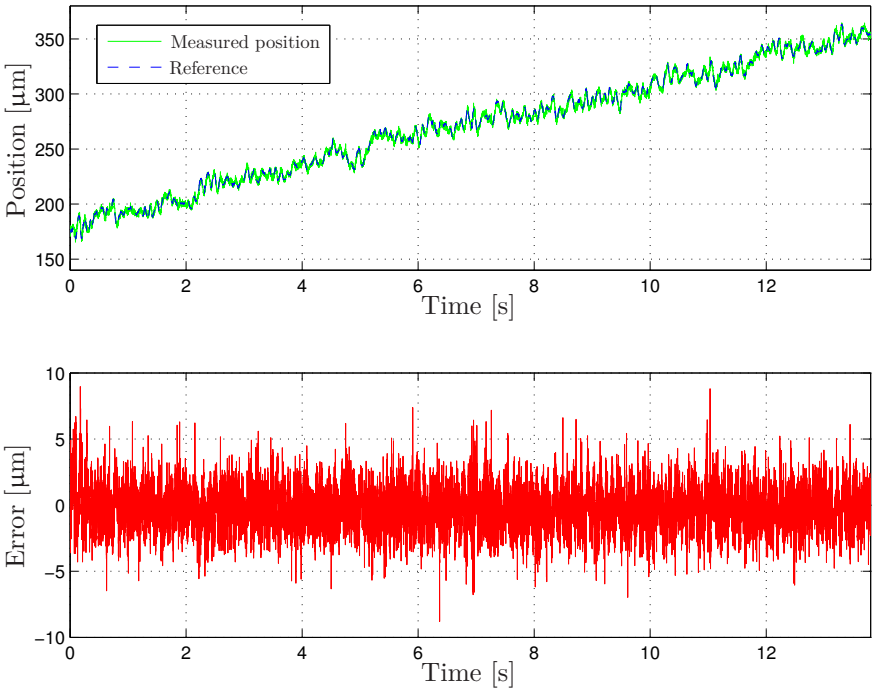

Figure 5.3 Reference value and measured position of the micro manipulator during milling experiment with compensation along the y-direction (upper panel) and corresponding control error (lower panel).

base as shown in Figure 5.1—*i.e.*, no online position compensation was active. The results of the experiments will be evaluated and contrasted to the results obtained with online position compensation in the next section.

5.4 Experimental Evaluation

In this section, the achieved experimental milling results are evaluated using statistical methods. Further, the surface roughness of the machined aluminium workpieces are measured and compared, so as to quantify the milling performance.

Coherence Spectra

An important aspect to consider in the controller design is if the nonlinear dynamics in the piezo-actuators influence the frequency characteristics of the position controlled micro manipulator, or if the proposed control archi-

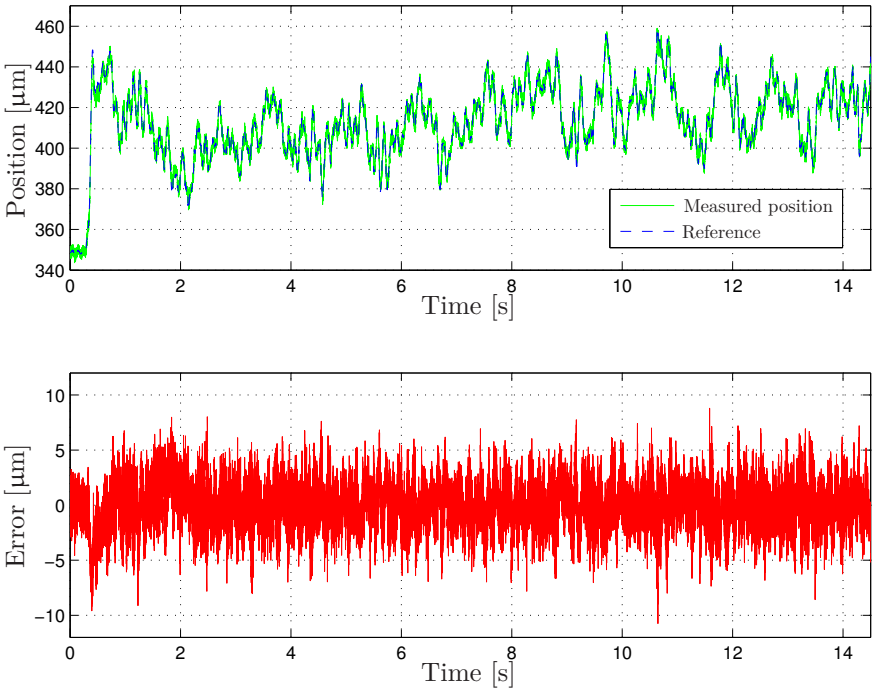

Figure 5.4 Reference value and measured position of the micro manipulator during milling experiment with compensation along the z-direction (upper panel) and corresponding control error (lower panel).

tecture is able to reduce its influence to a sufficient level. To that purpose, the quadratic coherence spectrum [Johansson, 1993], *i.e.*,

$$\gamma_{uy}(\omega) = \frac{|S_{uy}(i\omega)|^2}{S_{uu}(i\omega)S_{yy}(i\omega)}, \tag{5.1}$$

where $S_{uy}(i\omega)$ is the power cross-spectrum between the input u and the output y, $S_{uu}(i\omega)$ and $S_{yy}(i\omega)$ are the autospectra for u and y, respectively, is investigated. The coherence spectra for the dynamics in the x-, y-, and z-axes of the micro manipulator are displayed in Figure 5.5. The diagrams have been obtained with the inner PID controller loops for the piezo-actuators active. It is observed that the relation between input and output in the x-, y-, and z-directions appears to be linear in the major parts of the frequency range of interest. However, in the respective actuation direction, the effects of the natural eigenfrequencies of the structure, of which some exhibit low damping, are clearly visible. Hence, the parts of the frequency range where the coherence

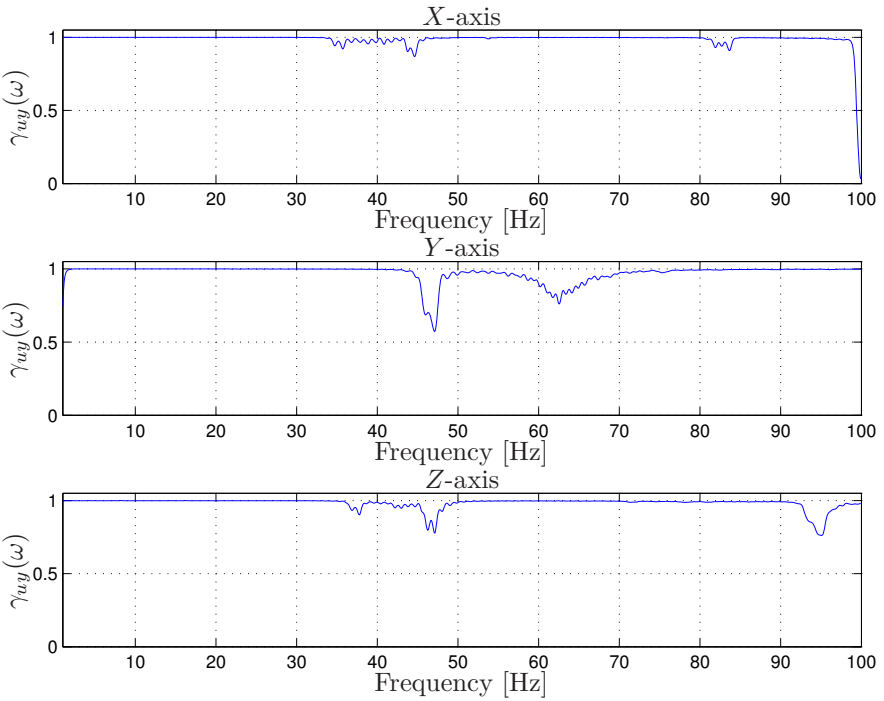

Figure 5.5 Estimated coherence spectra—obtained with the inner PID control loop for the piezo-actuators active—for the dynamics in the x, y, and z actuation directions of the micro manipulator.

is below one can be derived to these frequencies, *cf.* the frequency spectra in Figure 3.3 in Chapter 3. A plausible interpretation of this observation is that when the micro manipulator is in resonance, the nonlinear dynamics in the structure is more prominent and the linear system description is insufficient. Nevertheless, since the major part of the frequency range exhibits a linear relation, it is an indication that the chosen modeling and control approach can be justified.

Frequency Analysis of Control Error

From a control theory point of view, the results obtained from the milling experiments should be evaluated by examining if there is more information available in the control error—*i.e.*, separating the noise in the measurements from the possibly available information, which should be acted upon. To this purpose, auto-regressive moving average (ARMA) models as well as frequency spectra of the control errors presented in Figures 5.2–5.4 are esti-

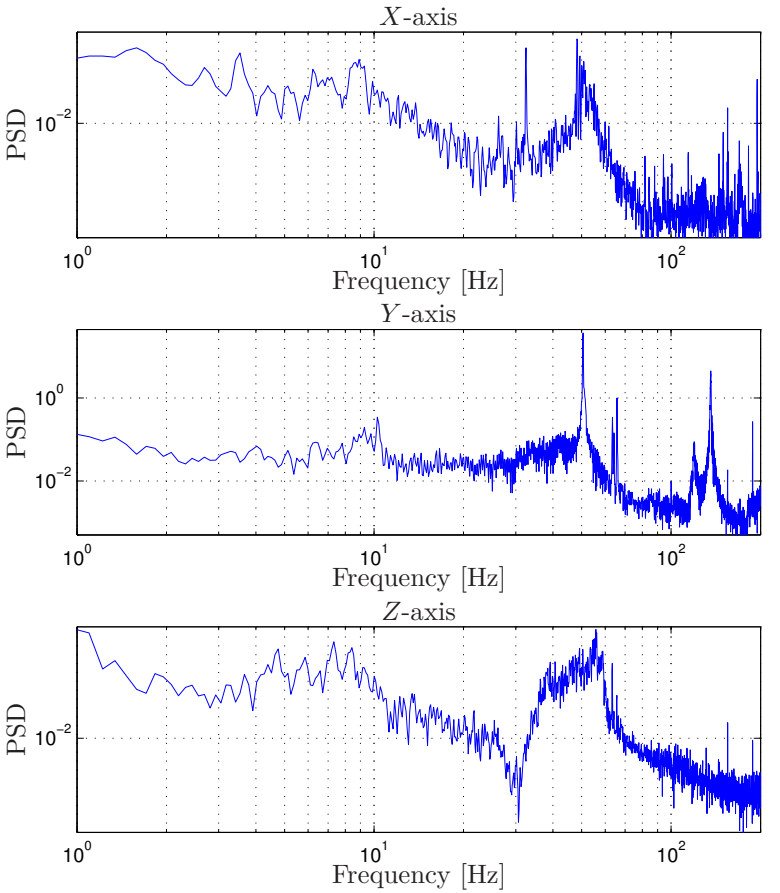

Figure 5.6 Estimated power spectral densities for the control error in Figures 5.2–5.4, measured during milling experiments in all actuation directions of the micro manipulator.

mated. The latter are estimated using Welch's method [Johansson, 1993]. The estimated power spectral densities (PSD) for the control error in the performed milling experiments are displayed in Figure 5.6. The spectra are further discussed in Section 5.5.

Measurement of Milling Profiles

Since the main objective of the micro manipulator is to achieve a high position-accuracy of the machined surface of the workpiece, a Mahr surface

measurement device of model M400 SD26 [Mahr GmbH, 2011] was utilized to measure the surface roughness of the obtained profiles on the aluminium workpieces. The device is equipped with a sensitive probe which was sliding along the surface to be measured while recording the profile. Further, the measurement device was calibrated such that it had a measurement accuracy better than 1 µm.

Milling with Compensation The results of the surface roughness measurements, for the three milling experiments in Figures 5.2–5.4, where online position compensation with the micro manipulator was active, are displayed in Figure 5.7. The measured profiles indicate that the milling accuracy in the x- and y-directions are within ± 7 µm and that the error of the measured milling profile is within approximately ± 12 µm in the z-direction of the micro manipulator. Furthermore, it is noted that the measured profiles correspond well to the measurements from the capacitive sensors attached to the micro manipulator, which are used for the position control feedback. This correspondence provides experimental validation that the measured position of the micro manipulator agrees with the actual position of the milling tool. Photos of the machined surfaces for the experiments in the x-, y, and z-directions are provided in Figures 5.9–5.11.

Milling Without Compensation The resulting surface roughness of the profiles from the uncompensated milling experiments is displayed in Figure 5.8. To evaluate the quality of the measured profiles from the experiments with online compensation, compared to the profiles obtained in milling without compensation, both the maximum peak-to-peak error e_m and the standard deviation σ_e of all profiles are calculated. The standard deviation σ_e is calculated as

$$\sigma_e = \sqrt{\frac{1}{N-1}\sum_{i=1}^{N}(e_i - \bar{e})^2}, \tag{5.2}$$

where N is the number of data points and $\bar{e}$ is the mean of the error. Table 5.1 shows the maximum error of the profiles, calculated as the minimum value subtracted from the maximum value, and the standard deviations from the nominal profile.

5.5 Discussion

Given the results in Table 5.1, it is evident that online compensation with the micro manipulator has improved the milling accuracy significantly, compared to the uncompensated case. From the experimental evaluation presented in this chapter, it can be concluded that the control error in the micro manipulator controller is below ± 12 µm in all axes, which is well below the desired

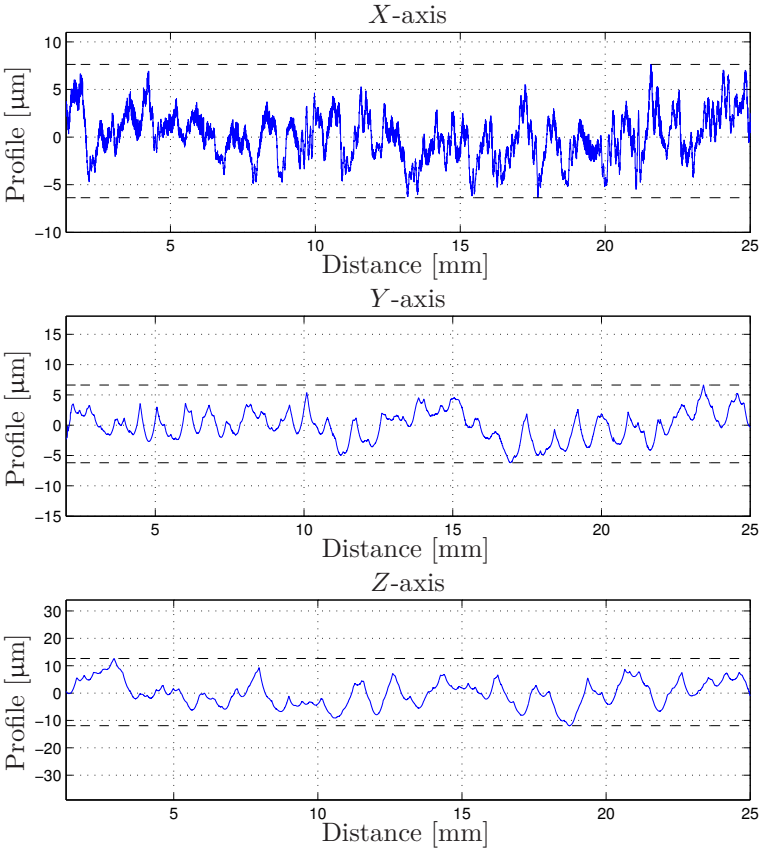

Figure 5.7 Position profiles of machined surfaces after face milling in the x-direction and peripheral milling experiments in the y- and z-directions of the micro manipulator. In all experiments, online compensation with the micro manipulator was utilized, along the corresponding actuation axis. The dotted lines indicate the maximum and minimum values.

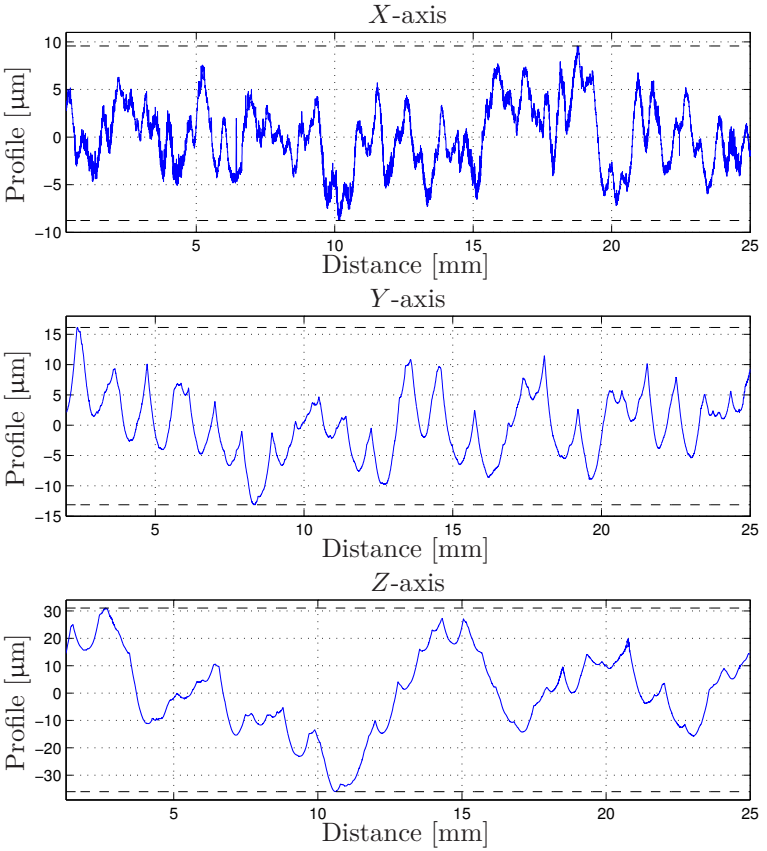

Figure 5.8 Position profiles of machined surfaces after uncompensated milling in the x-, y-, and z-directions of the micro manipulator, respectively. The dotted lines indicate the maximum and minimum values. The profiles should be compared with the profiles in Figure 5.7, obtained with online compensation.

Table 5.1 Maximum error e_m and standard deviation σ_e of milling profiles obtained with and without online position compensation utilizing the micro manipulator.

Axis	e_m compensated (µm)	e_m uncompensated (µm)	Ratio
x	14.0	18.3	1.3
y	12.8	29.3	2.3
z	24.5	67.0	2.7
Axis	**σ_e compensated (µm)**	**σ_e uncompensated (µm)**	**Ratio**
x	2.8	7.6	2.7
y	2.5	5.6	2.2
z	4.7	14.9	3.2

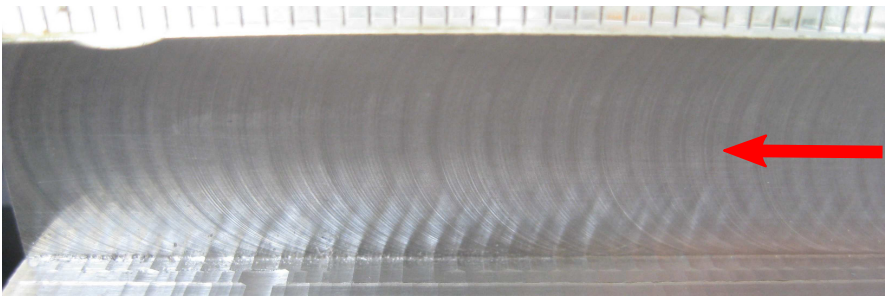

Figure 5.9 Workpiece after face milling on the surface indicated by the red arrow, with compensation along the x-direction of the micro manipulator.

accuracy of 50 µm. Moreover, the standard deviation of the milling profiles has been decreased by using the proposed micro manipulator. This means that the micro manipulator not only increases the accuracy of the milling, but also that the stationary and low-frequency errors in the robot position can be handled.

Several conclusions can be drawn from frequency analysis of the control error. All frequency spectra of the control errors in Figure 5.6 exhibit peaks at approximately 10 Hz and at 50 Hz. The latter is a disturbance from the power network system and hence inherent in an industrial environment with a multitude of potential disturbances. The former frequency peak relates to the eigenfrequencies of the industrial robot in the corresponding Cartesian directions. This is experimentally confirmed by modal analysis of the REIS RV40 robot [Schneider, 2010]. However, while the peaks are visible in the

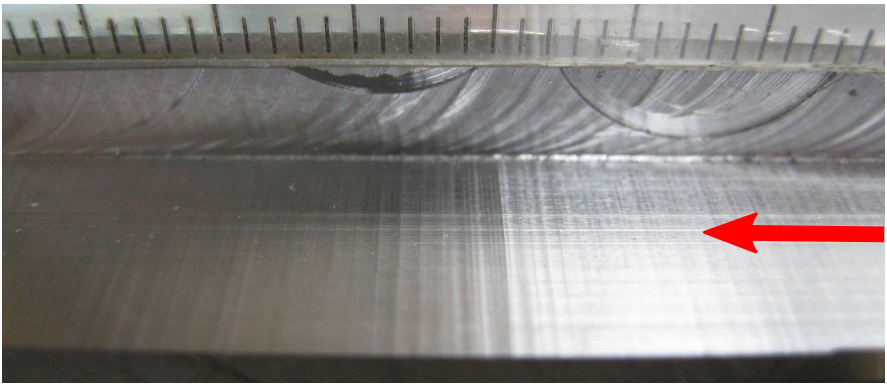

Figure 5.10 Workpiece after peripheral milling on the surface indicated by the red arrow, with compensation along the y-direction of the micro manipulator.

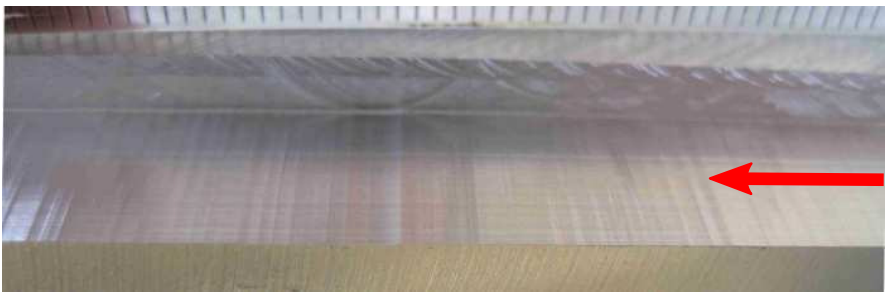

Figure 5.11 Workpiece after peripheral milling on the surface indicated by the red arrow, with compensation along the z-direction of the micro manipulator.

frequency spectra, they are not prominent. This indicates that the micro manipulator controller can attenuate one of the most important disturbances during the milling—*i.e.*, the natural eigenfrequencies of the robot.

The achievable bandwidth of the Cartesian position control for the industrial robot is limited by the natural eigenfrequencies of the mechanical construction and the noncolocated sensing and actuation—*i.e.*, joint-based actuation and task space measurements of the position and orientation of the workpiece [Fasse and Hogan, 1995]. The advantage of utilizing the proposed micro manipulator as a complement to the industrial robot is the significantly increased bandwidth of the end-effector position control. This is the result of the colocation of the actuation—with the micro manipulator—and the task space sensors, as theoretically investigated in [Sharon et al., 1993].

In the current experimental setup, the bandwidth of the micro manipulator is 3–4 times higher than that of the industrial robot, which means that the oscillations of the robot with its eigenfrequencies are possible to compensate for using the micro manipulator.

Further, the influence of the mechanical design of the micro manipulator on the milling performance is visible in the frequency spectra of Figure 5.6. The zero in the z-direction of the micro manipulator at 30 Hz is clearly visible in the corresponding frequency spectrum. Similarly, one of the natural eigenfrequencies of the micro manipulator in the x-axis at 32 Hz is visible. The bandwidth of the closed-loop position control for the micro manipulator is consequently limited by the mechanical design.

5.6 Conclusions

This chapter has investigated the milling accuracy of industrial robots by utilizing a high bandwidth, piezo-actuated, micro manipulator for demanding machining processes. It was shown in an experimental validation procedure, comprising several different milling experiments with online position compensation with the micro manipulator, that the proposed method offers significantly higher accuracy in terms of surface roughness, compared to the standard method for milling without online compensation.

6

Conclusions and Future Work

In this part of the thesis, methods for increasing the accuracy of machining processes with industrial robots were investigated. In particular, a macro/micro configuration with a conventional robot and an additional piezo-actuated micro manipulator with significantly higher bandwidth than the robot was considered. Modeling of the micro manipulator was performed and a subsequent model-based control architecture for the micro manipulator and the robot was proposed and experimentally verified. In a subsequent experimental milling verification, the proposed configuration and control architecture were evaluated and compared to the standard uncompensated case with a robot only. The conclusion from these results is that a significant increase in the position accuracy of the machined parts can be obtained with the proposed configuration and control architecture.

For the future, the controller will be implemented and experimentally verified on an improved version of the micro manipulator, with a complete redesign of the mechanical actuation principle, for increased bandwidth of the position controller. In addition, an implementation of a mid-ranging control strategy for simultaneous control of the robot and the micro manipulator, while keeping the latter within its limited working range, is required when the forces in the cutting process are increased. Further, the online compensation strategy discussed in this thesis should be combined with offline compensation approaches. To this purpose, results from ongoing research on robot joint modeling and subsequent parameter identification, see [Lehmann et al., 2013], can be used. By integration of the micro manipulator with a model-based path-planning strategy in a CAM software, the final goal is to be able to machine with industrial robots based on a CAD specification with a position accuracy better than 50 μm also for materials such as steel, where the required process forces in the milling are increased compared to aluminium that was investigated in this thesis.

Part II

Optimal Control of Vehicles

7

Introduction

Development of mathematical models and model-based control strategies for optimal road-vehicle maneuvers in time-critical situations have emerged as powerful tools during the past decade, see [Funke et al., 2012]. This is motivated to a large extent by the desire to devise improved future safety systems for road-vehicles and driver assistance technologies. Advanced vehicle safety systems of today, such as the Electronic Stability Program (ESP) systems, Anti-Lock Braking systems (ABS), and Active Slip Regulation (ASR) systems, see, *e.g.*, [Isermann, 2006], [Liebemann et al., 2005], and [Bauer et al., 2000], are still behind the maneuvering performance achievable by professional race car drivers in critical situations. Even though the solution of an optimal control problem depends on the particular choice of model and cost function, the fundamental behavior and control strategies found in the optimization can be used as inspiration for, or even integrated in, future safety systems. Hence, the research aim of the work presented in this thesis is the following:

- Develop a methodology for solving optimal control problems for road-vehicles in time-critical situations;
- Test the methodology on different vehicle maneuvering situations, so as to increase the understanding of vehicle dynamics in extreme situations;
- Investigate the influence of the road-surface on the optimal maneuver;
- Analyze the obtained results to the purpose of design of new driver assistance technologies with improved performance, compared to state-of-the-art systems of today.

As previously investigated in the literature, the optimal solution itself usually cannot be employed directly for online control of an automotive, as described in the following quote from [Sharp and Peng, 2011]:

> Most often, the optimal control itself will be interesting mainly insofar as it enables the discovery of the best possible system performance. Occasionally, the optimal control will provide a basis for the design and operation of practical systems.

The vehicle–road interaction in an aggressive vehicle maneuver is complex, and consequently requires careful vehicle and tire modeling in order for the optimal control to provide significant results. In particular, if optimal control with time-optimality as criterion is considered, the control inputs and state variables are often at their limits and the vehicle and tire models must perform even outside their normal range of operation. Another challenge with tire modeling is the experimental measurements of model parameters. An experimental evaluation presented in [Carlson and Gerdes, 2005] exhibits large variability of the measurement of the longitudinal tire stiffness—*i.e.*, the slope of the longitudinal force-slip curve. Further, when considering combined longitudinal and lateral slip, the tire force modeling is even more demanding, considering that the tire model needs to capture the combinations of slip which result in maxima and minima in the resulting tire force. In addition, it is of interest to be able to model the tire forces on different road-surfaces, such as asphalt, snow, and ice. To that purpose, scaling of nominal tire model parameters have been proposed and experimentally measured, see [Pacejka, 2006; Braghin et al., 2006]. This strategy is investigated for optimal maneuvers on different road-surfaces in this thesis.

Vehicle modeling has previously been investigated extensively in the literature, see, *e.g.*, [Kiencke and Nielsen, 2005; Isermann, 2006; Schindler, 2007; Ellis, 1994]. However, most modeling approaches have been employed and tested in simulations, and are not tailored for optimal control purposes. In [Lundahl et al., 2011] it was shown how simplified vehicle models—identified from experimental data collected with a test vehicle on a race track—were able to capture essential dynamic properties of the car. Previous work in the subject of optimal control of vehicles in certain time-critical situations such as T-bone collisions and cornering can be found in, *e.g.*, [Chakraborty et al., 2011; Velenis and Tsiotras, 2005; Velenis, 2011; Kelly and Sharp, 2010]. In [Anderson et al., 2010; Anderson et al., 2012], methods for constraint-based trajectory planning for optimal maneuvers are presented. Further, the papers [Sundström et al., 2010; Andreasson, 2009] discuss optimal control of over-actuated vehicles, where similar optimization tools as those employed in this thesis are utilized.

8

Optimization Methodology for Road-Vehicle Maneuvers

8.1 Introduction

In this chapter, a methodology for solving optimal control problems for road-vehicles in time-critical situations is presented. The challenge here is to find the correct combinations of vehicle and tire models and optimization formulations. To verify the proposed methodology, a hairpin maneuver, a double lane-change maneuver, as well as a 90°-turn maneuver are investigated. In all of these maneuvers, a time-optimal criterion is considered, which results in that the vehicle—and in particular the tires—are performing at their limits. Hence, the solution provided gives an indication of the maneuverability of the vehicle in this particular situation. Further, different chassis modeling and tire modeling principles are employed and compared to each other. This chapter of the thesis is based on the publications [Olofsson et al., 2013], [Berntorp et al., 2013b], and [Lundahl et al., 2013].

The structure of this chapter is as follows: In Section 8.2, the problem description is presented. Vehicle and tire modeling and the specific models utilized in this work are discussed in Section 8.3, followed by a section on the formulation and solution methodology for the studied time-optimal maneuvering problems in Section 8.4. Optimization results and a subsequent discussion of the obtained results are provided in Section 8.5. Finally, a summary is provided and conclusions are drawn in Section 8.6.

8.2 Problem Description

The research aim of the optimization methodology presented in this chapter is twofold. First, by investigating the solutions of the optimal control problems for a set of different vehicle maneuvers—such as the hairpin turn displayed in Figure 8.1—it is plausible that the understanding of vehicle dynamics in

Figure 8.1 An example of an aggressive maneuver with a car, known as a hairpin turn. Photo courtesy of RallySportLive. Reprinted with permission.

time-critical situations can be increased. The second goal of the investigation is to explore whether different vehicle and tire models yield fundamentally different solutions, not only in the resulting cost function value but also in the internal states and variables of the vehicle model. Vehicle and tire models written as differential-algebraic equation (DAE) systems of the format

$$G(\dot{x}(t), x(t), z(t), u(t)) = 0, \tag{8.1}$$

where G is a twice continuously differentiable nonlinear function of the vehicle state time-derivatives $\dot{x}(t)$, states $x(t)$, algebraic variables $z(t)$, and control inputs $u(t)$, are considered. The time-dependency of the DAE variables will be implicit in the rest of the thesis for notational convenience.

The motivation for the model comparison presented in this chapter is that most comparisons presented earlier in the literature are based on simulation results rather than optimal control results. In the latter, the control signals are typically at their limits and thus time-optimal control solutions tend to push the vehicle and tire models more to extreme performance levels than simulations do. Hence, it is plausible that different conclusions about model behavior can be made from such a comparison.

8.3 Modeling

The vehicle dynamics modeling in this section incorporates the vehicle motion modeling and the tire force modeling. Several different approaches to chassis modeling are investigated. In addition, two approaches to tire modeling are considered. The tire model calibration procedure is also briefly discussed.

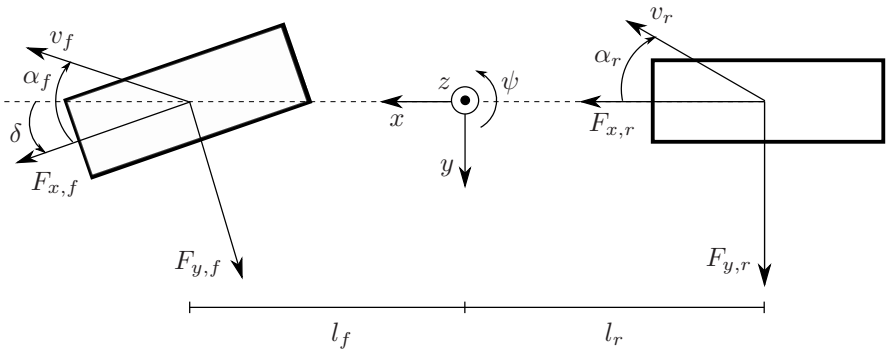

Figure 8.2 The single-track model utilized as a base model in the optimal control formulation in this chapter.

Vehicle Modeling

As a basis for the vehicle dynamics model, a two-dimensional single-track model where the left and right wheels are lumped together, having two translational and one rotational degree of freedom, is used, see Figure 8.2. The motion equations are straightforward to derive from basic mechanical relationships, see, *e.g.*, [Schindler, 2007; Ellis, 1994], and can be expressed as follows

$$\dot{v}_x - v_y\dot{\psi} = \frac{1}{m}(F_{x,f}\cos(\delta) + F_{x,r} - F_{y,f}\sin(\delta)), \tag{8.2}$$

$$\dot{v}_y + v_x\dot{\psi} = \frac{1}{m}(F_{y,f}\cos(\delta) + F_{y,r} + F_{x,f}\sin(\delta)), \tag{8.3}$$

$$I_{zz}\ddot{\psi} = l_f F_{y,f}\cos(\delta) - l_r F_{y,r} + l_f F_{x,f}\sin(\delta), \tag{8.4}$$

where m is the vehicle mass, I_{zz} is the vehicle inertia, $\dot{\psi}$ is the yaw rate, δ is the wheel steering angle, $v_{x,y}$ are the longitudinal and lateral velocities, $l_{f,r}$ are the distances from center-of-gravity to the front and rear wheel base, and $F_{x,y}$ are the longitudinal and lateral forces acting on the front and rear wheels.

The wheel dynamics is modeled such that the input torque affects the wheel angular velocity *via* a first-order system and is given by

$$T_i - I_w\dot{\omega}_i - F_{x,i}R_w = 0, \quad i \in \{f, r\}. \tag{8.5}$$

Here, ω_i is the wheel angular velocity, T_i is the driving and braking torque, I_w is the wheel inertia, and R_w is the loaded wheel radius. Following [Pacejka,

2006], the slip angles $\alpha_{f,r}$ and slip ratios $\kappa_{f,r}$ are described by

$$\frac{\sigma\dot{\alpha}_f}{v_{x,f}} + \alpha_f = \delta - \arctan\left(\frac{v_y + l_f\dot{\psi}}{v_x}\right), \tag{8.6}$$

$$\frac{\sigma\dot{\alpha}_r}{v_{x,r}} + \alpha_r = -\arctan\left(\frac{v_y - l_r\dot{\psi}}{v_x}\right), \tag{8.7}$$

$$\kappa_f = \frac{R_w\omega_f - v_{x,f}}{v_{x,f}}, \tag{8.8}$$

$$\kappa_r = \frac{R_w\omega_r - v_{x,r}}{v_{x,r}}, \tag{8.9}$$

$$v_{x,f} = v_x\cos(\delta) + (v_y + l_f\dot{\psi})\sin(\delta), \tag{8.10}$$

$$v_{x,r} = v_x, \tag{8.11}$$

where σ is the relaxation length.

Vehicle Motion Model Extensions To the purpose of investigating the model complexity required for accurate modeling of the vehicle motion in an aggressive maneuver, different extensions of the basic single-track model in (8.2)–(8.4) are considered. In particular, the double-track model in Figure 8.3 is employed. This model is a more realistic description of the vehicle, where each wheel is modeled independently, in contrast to the single-track model. More specifically, the following model configurations are studied:

A. Single-track model as described in the previous paragraph;

B. Single-track model with roll dynamics—*i.e.*, an additional degree of freedom about the x-axis;

C. Single-track model with pitch dynamics—*i.e.*, an additional degree of freedom about the y-axis and with longitudinal load transfer in the corresponding direction;

D. Double-track model with roll dynamics and lateral load transfer;

E. Double-track model with roll and pitch dynamics and both longitudinal and lateral load transfer.

The double-track model with roll and pitch dynamics is illustrated in Figure 8.3. For the complete derivation of the equations for this model, see [Berntorp, 2013].

Pitch and Roll Dynamics For modeling of the roll and pitch dynamics and the corresponding roll angle ϕ and pitch angle θ, it is assumed that the

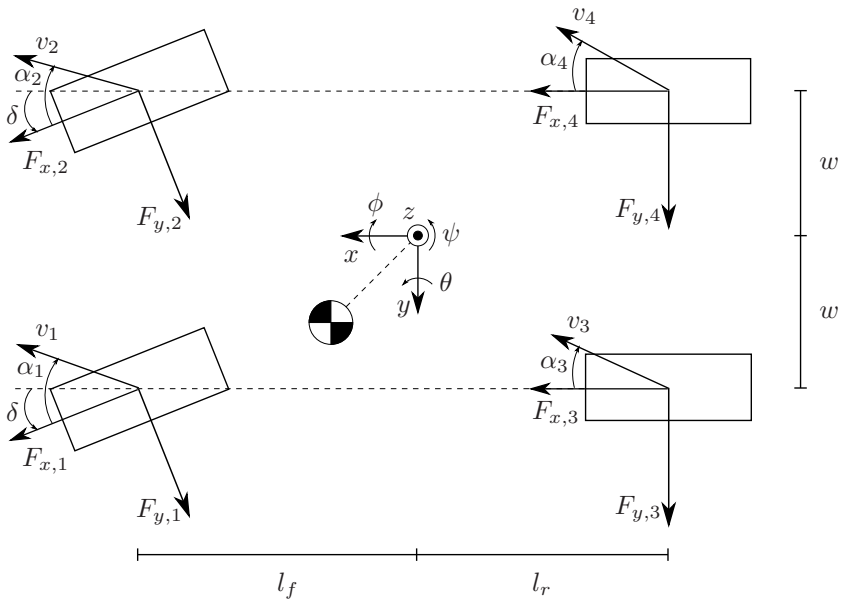

Figure 8.3 The double-track model with pitch and roll dynamics.

suspension system of the vehicle can de described by a rotational inertia-spring-damper system. Hence, the effect on the roll dynamics by the suspension system can be written as

$$\tau_\phi = -D_\phi \dot{\phi} - K_\phi \phi, \tag{8.12}$$

where τ_ϕ is the torque produced by the suspension system, K_ϕ is the stiffness, and D_ϕ is the damping. The pitch dynamics is characterized similarly by the corresponding parameters K_θ and D_θ.

Load Transfer The load transfer in the roll and pitch directions, respectively, is modeled utilizing the same assumptions as for the roll and pitch dynamics—*i.e.*, the rotational spring-damper system models the torque rotating the vehicle in the corresponding degree of freedom. In addition, it is assumed that the roll angle ϕ and pitch angle θ are small and that the load transfer in the two directions can be modeled independently of each other. Under these assumptions, the change in the normal force $\Delta F_{z,\phi}$ in the roll direction can be determined from the relation

$$4w\Delta F_{z,\phi} = -D_\phi \dot{\phi} - K_\phi \phi, \tag{8.13}$$

for the left wheels and from

$$4w\Delta F_{z,\phi} = D_\phi \dot{\phi} + K_\phi \phi, \tag{8.14}$$

for the right wheels. Similarly, the load transfer $\Delta F_{z,\theta}$ in the pitch direction is given by the relation

$$2l\Delta F_{z,\theta} = D_\theta \dot{\theta} + K_\theta \theta, \tag{8.15}$$

for the front wheels and from

$$2l\Delta F_{z,\theta} = -D_\theta \dot{\theta} - K_\theta \theta, \tag{8.16}$$

for the rear wheels. In the single-track models with the lumped wheels, the effects of the pitch load transfer are added for the respective wheel pair. The numerical values for the vehicle model parameters used in this study are provided in Table A.1 in Appendix A.

Tire Modeling

When developing a methodology for investigation of optimal maneuvers, it is of interest to be able to handle and compare different tire characteristics. Hence, the capability of the developed methodology to handle different tire models is essential. In this work, two different model principles for tire modeling are considered, whose characteristics are described next.

The nominal tire forces—*i.e.*, the forces under pure longitudinal or lateral slip conditions—are computed with the *Magic Formula model* [Pacejka, 2006], given by

$$F_{x0,i} = \mu_x F_{z,i} \sin(C_{x,i} \arctan(B_{x,i}\kappa_i)), \tag{8.17}$$

$$F_{y0,i} = \mu_y F_{z,i} \sin(C_{y,i} \arctan(B_{y,i}\alpha_i)), \ i \in \{f, r\}, \tag{8.18}$$

$$F_{z,i} = mg(l - l_i)/l, \ i \in \{f, r\}, \text{ with } l = l_f + l_r, \tag{8.19}$$

where, μ_x and μ_y are the friction coefficients, B and C are model parameters to be calibrated from experimental data, and g is the constant of gravity.

Under combined slip conditions—*i.e.*, both the longitudinal slip κ and the lateral slip α are nonzero—the resulting tire forces will depend on both of these slip quantities. The strategy for modeling this coupling effect on the tire forces is a crucial part of the tire modeling in aggressive vehicle maneuvers. In a time-optimal maneuver, the resulting control solution will use the best combination of longitudinal and lateral force, and these forces are coupled *via* the physics of the specific tire. Tire modeling under combined slip behavior and subsequent experimental measurements of tire model parameters have been discussed extensively in the literature previously, see, *e.g.*, [Kiencke and Nielsen, 2005; Rajamani, 2006; Pacejka, 2006; Braghin et al., 2006; Isermann, 2006]. In this work, two approaches to this purpose have been adopted from the literature: the *friction ellipse* and the Pacejka *weighting functions*.

Friction Ellipse The friction ellipse is an established method for calculating the lateral force F_y based on the longitudinal force and the normal force. The relation is given by

$$F_{y,i} = F_{y0,i}\sqrt{1 - \left(\frac{F_{x0,i}}{\mu_x F_{z,i}}\right)^2},\ i \in \{f, r\}. \tag{8.20}$$

In simulations, the force F_x is often used as an input variable. However, in the optimal control problem studied in this chapter, the driving and braking torques on the wheels are used as inputs, since these are variables that can be actuated in a physical setup of a vehicle. Consequently, the force F_x is determined dynamically from the relation (8.5).

Weighting Functions A second approach to modeling of the combined slip, described in [Pacejka, 2006], is to scale the nominal forces in (8.17)–(8.18) with weighting functions $G_{x\alpha,i}$ and $G_{y\kappa,i}$. These functions are dependent of the slip quantities α and κ. The relations in the longitudinal direction are

$$B_{x\alpha,i} = B_{x1,i}\cos(\arctan(B_{x2,i}\kappa_i)), \tag{8.21}$$
$$G_{x\alpha,i} = \cos(C_{x\alpha,i}\arctan(B_{x\alpha,i}\alpha_i)), \tag{8.22}$$
$$F_{x,i} = F_{x0,i}G_{x\alpha,i},\ i \in \{f, r\}. \tag{8.23}$$

The corresponding relations in the lateral direction are given by

$$B_{y\kappa,i} = B_{y1,i}\cos(\arctan(B_{y2,i}(\alpha_i - B_{y3,i}))), \tag{8.24}$$
$$G_{y\kappa,i} = \cos(C_{y\kappa,i}\arctan(B_{y\kappa,i}\kappa_i)), \tag{8.25}$$
$$F_{y,i} = F_{y0,i}G_{y\kappa,i},\ i \in \{f, r\}. \tag{8.26}$$

Tire Model Parameters

The parameters of the respective tire model should be determined based on experimental data. However, when comparing an optimal maneuver based on two different tire modeling principles, it is not obvious how to calibrate the models with respect to the measured tire force characteristics. One approach is to have the same average resultant force and another is to equalize the longitudinal stiffness. In this study, the same parameters have been used for the nominal lateral force—*i.e.*, the lateral force characteristics are the same for all models when considering pure lateral slip.

Two different tire models are calibrated and subsequently evaluated in this chapter. The resulting tire force, defined as

$$F_{i,\text{res}} = \sqrt{F_{x,i}^2 + F_{y,i}^2},\ i \in \{f, r\}, \tag{8.27}$$

is illustrated with two-dimensional surfaces as a function of the longitudinal slip κ and lateral slip angle α in Figures 8.14–8.17 in Section 8.5. The first tire is assumed to be isotropic, in the sense that it has the same properties in lateral and longitudinal directions. The second tire is described by model parameters presented in [Pacejka, 2006], which were identified from experimental data. The model is thus considered empirical in the sense that it represents the behavior of a realistic tire. In contrast to the first tire, this model gives a clearly nonisotropic behavior. For each tire, both a model based on the friction ellipse and a model based on the parametrization with weighting functions are fitted. The parameters for the respective model are presented in Table A.2 in Appendix A. The weighting functions model parameters were fitted to the original Pacejka model using least-squares approximations. Hence, both the friction ellipse model and the weighting functions model will exhibit equivalent tire characteristics for pure slip conditions for the nonisotropic tire configuration.

8.4 Optimal Control Problem

Based on the vehicle and tire dynamics described in the previous section, the time-optimal maneuvers for the different time-critical situations are to be determined. Mathematically, the control signals for achieving these maneuvers are calculated as the solution of a dynamic optimization problem. Considering the physical setup of the problem, it is clear that an optimal solution exists. The resulting optimization problem is more challenging than thought at first sight, since the desired time-optimality implies that the friction model of the tires operates on the boundary of its validity. Also, solving dynamic optimization problems where the time horizon is free, is more demanding than a problem with fixed end-time. Further, during the course of the development of the optimization methodology, it was found that numerical issues easily arise and that the optimization does not converge without proper initialization. In order to make the convergence more robust from a numerical point of view, scaling of the optimization variables to the same nominal interval is essential.

Formulation of Dynamic Optimization Problem

Consider the time horizon $t \in [0, t_f]$, where t_f is the free final time to be determined as part of the solution procedure. The vehicle dynamics—see (8.2)–(8.11) for the equations of the single-track model—is expressed as a differential-algebraic equation (DAE) system according to

$$G(\dot{x}, x, z, u) = 0, \tag{8.28}$$

where x are the state variables, z are the algebraic variables, and $u = \begin{pmatrix} T & \delta \end{pmatrix}$, where $T = \begin{pmatrix} T_f & T_r \end{pmatrix}$ is a vector with the driving and braking torques. The wheel driving and braking torques T on the wheels and the steering angle δ are considered as the input variables; in the double-track models the front and rear torques are distributed equally between the right and left wheels. Furthermore, the DAE system $h(x, z, u) = 0$ is introduced for the tire force model. The dynamic optimization problem to be solved can then be stated as follows:

$$
\begin{aligned}
\text{minimize} \quad & t_f && (8.29)\\
\text{subject to} \quad & T_{i,\min} \le T_i \le T_{i,\max},\ i \in \{f, r\} && (8.30)\\
& |\delta| \le \delta_{\max} \quad , \quad |\dot{\delta}| \le \dot{\delta}_{\max} && (8.31)\\
& |F_{x,i}| \le F_{x,i,\max},\ i \in \{f, r\} \text{ or } \{1, 2, 3, 4\} && (8.32)\\
& |F_{y,i}| \le F_{y,i,\max},\ i \in \{f, r\} \text{ or } \{1, 2, 3, 4\} && (8.33)\\
& \left(\frac{X_p}{R_1^j}\right)^{\gamma_j} + \left(\frac{Y_p}{R_2^j}\right)^{\gamma_j} \ge 1,\ j = 1, \ldots, n_l && (8.34)\\
& \left(\frac{X_p}{R_1^j}\right)^{\gamma_j} + \left(\frac{Y_p}{R_2^j}\right)^{\gamma_j} \le 1,\ j = n_{l+1}, \ldots, n && (8.35)\\
& x(0) = x_0 \quad , \quad x(t_f) = x_{t_f} && (8.36)\\
& z(0) = z_0 \quad , \quad z(t_f) = z_{t_f} && (8.37)\\
& G(\dot{x}, x, z, u) = 0 \quad , \quad h(x, z, u) = 0, && (8.38)
\end{aligned}
$$

where x_0 is the initial state vector, x_{t_f} is the desired state vector at $t = t_f$, z_0 and z_{t_f} are the corresponding vectors for the algebraic variables, and (X_p, Y_p) is the position of the center-of-mass of the vehicle. The track constraint for the different investigated maneuvers is formulated using n super-ellipses of degree $\gamma_j,\ j = 1, \ldots, n$, and the shape of the path is determined by the radii R_1^j and $R_2^j,\ j = 1, \ldots, n$. Further, the constraints on the driving and braking torques and tire forces are specified according to

$$
\begin{aligned}
-\mu_x F_{z,f} R_w \le T_f \le 0, && (8.39)\\
-\mu_x F_{z,r} R_w \le T_r \le \mu_x F_{z,r} R_w, && (8.40)\\
|F_{x,i}| \le \mu_x F_{z,i}, && (8.41)\\
|F_{y,i}| \le \mu_y F_{z,i},\ i \in \{f, r\} \text{ or } \{1, 2, 3, 4\}. && (8.42)
\end{aligned}
$$

Solution of Optimal Control Problem

Because of the complex nature of the nonlinear and nonconvex optimization problem in (8.29)–(8.38), analytical solutions are intractable. Instead, numerical methods based on simultaneous collocation [Biegler et al., 2002] are

utilized. In particular, direct collocation was used, where all state and input variables, originally described in continuous time, were discretized prior to the optimization. This results in a discrete-time nonlinear program (NLP). The collocation procedure transforms the original infinite-dimensional problem to a finite-dimensional problem with a large, however finite, number of optimization variables, on which numerical optimization methods can be applied.

Implementation and Tools

The vehicle and tire dynamics are implemented using the modeling language Modelica [Modelica Association, 2013]. Since the primary feature of Modelica is simulation, the language does not support explicit formulation of optimal control problems. Consequently, Optimica [Åkesson, 2008], which is an extension of Modelica for high-level description of dynamic optimization problems based on Modelica models, are utilized to that purpose. The Modelica and Optimica code required for implementation of the single-track vehicle model and tire dynamics for the isotropic tire model based on the friction ellipse described in Section 8.3, and the optimal control problem for the hairpin turn maneuver, is given in Appendix B as an example. The implementation of the other maneuver situations and model configurations are similar and are therefore not presented here.

The collocation procedure and solution of the optimization problem are performed using the open-source software platform JModelica.org [Åkesson et al., 2010; JModelica.org, 2013]. The user interacts with the software using the scripting language Python, see Figure 8.4. In JModelica.org, orthogonal collocation is implemented, where Lagrange polynomials are used for representation of the state profiles in each element and the location of the collocation points are chosen as the corresponding Radau points. The resulting NLP is solved internally using the numerical solver Ipopt [Wächter and Biegler, 2006], which is a solver based on interior-point methods opted for large, but sparse, optimization problems. Since collocation procedures often result in this kind of optimization problems, Ipopt is an appropriate solver for the current optimal control problem.

Initialization Procedure

Robust convergence to a solution of the NLP in Ipopt relies on proper initialization. Two approaches are available to this purpose: Simulation of an initial guess using driver models and division of the problem into smaller subproblems, respectively. In this thesis, the latter approach has been utilized. Consequently, each optimal control problem is solved as a sequence of smaller optimization problems. The optimal control problems for the 90°-turn and the double lane-change maneuvers are solved in one or two steps, depending

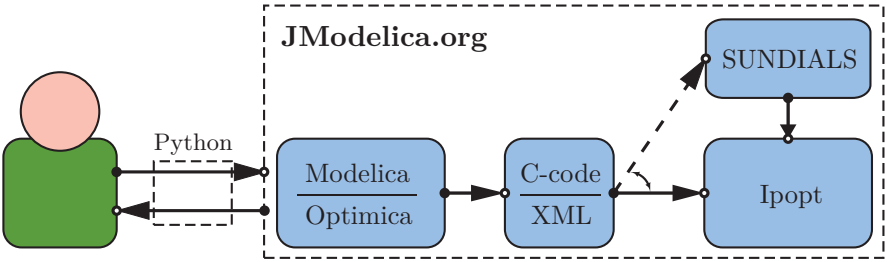

Figure 8.4 In the figure, the usage of the optimization software JModelica.org is illustrated. The user utilizes the scripting language Python in order to communicate with JModelica.org. The Modelica and Optimica models are compiled to C-code and an XML description. The NLP is subsequently solved using the solver Ipopt. Simulation of DAE systems for verification purposes is possible using the software SUNDIALS [SUNDIALS, 2013].

on model configuration. However, the hairpin-turn problem is solved in four steps, see Figure 8.5. The results from the solution of each subproblem are used for initialization of the subsequent problem. Hence, the final optimal maneuvers are determined stepwise.

8.5 Results

In this section, the results obtained for the studied vehicle and tire models in the different time-critical maneuvers are presented and subsequently evaluated and compared. First, the vehicle models are in focus and evaluated in two different maneuvers. Second, the tire models are investigated in the hairpin maneuver.

For the evaluations, the maximum allowed steering angle δ and steering angle change rate $\dot{\delta}$ were specified to 30 deg and 60 deg/s, respectively, which are reasonable parameters, both seen from physical and driver limitations. It should be noted that these limitations correspond to the wheel angle δ, not the steering wheel angle. Further, it is assumed in the vehicle model that the car considered is rear-wheel driven as indicated by the constraints (8.39)–(8.40).

Optimal Maneuvers for Different Vehicle Models

The different chassis model configurations A–E were evaluated in a double lane-change maneuver and in a 90°-turn. The tire dynamics was modeled using the Pacejka weighting functions with model parameters corresponding to the nonisotropic behavior. The initial velocity of the vehicle in the 90°-turn maneuver and double lane-change maneuver was $v_0 = 70$ km/h and

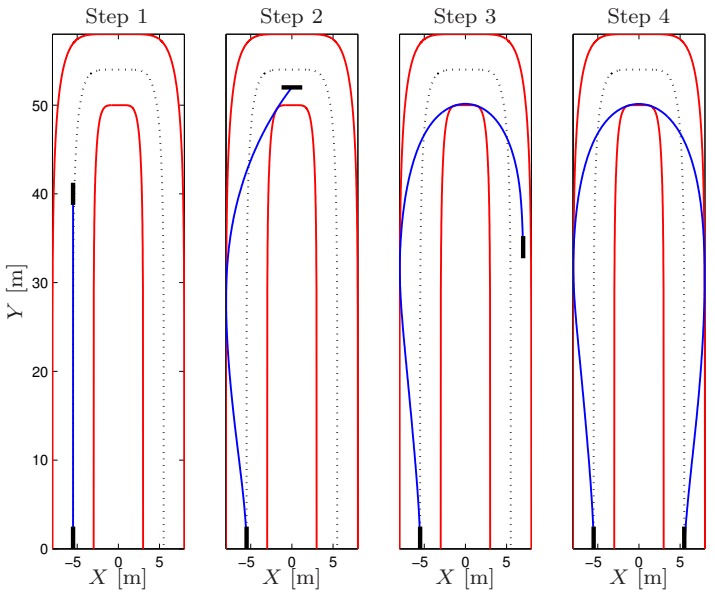

Figure 8.5 Initialization procedure for solving the time-optimal hairpin turn maneuver problem. The whole problem is solved by stepwise solving four successive problems. The black rectangles in the figure indicate the position and direction of the vehicle at the initial and final state in each subproblem.

$v_0 = 80$ km/h, respectively. The optimal control problem with a minimum-time criterion was solved for each of the configurations, which resulted in the vehicle trajectories displayed in Figures 8.6–8.7 and model state variables displayed in Figures 8.8–8.9. In the figures, the body slip β is defined as

$$\beta = \arctan\left(\frac{v_y}{v_x}\right), \tag{8.43}$$

and the tire forces for the right and left wheels have been added for the double-track models for visualization purposes. In the double lane-change maneuver, the vehicle starts in the lower left corner of the track and in the 90°-turn the vehicle starts in the lower right corner.

Several interesting observations can be made when comparing the different model configurations for the respective maneuver. The geometric trajectories in the XY-plane in Figures 8.6–8.7 obtained for the different models are approximately the same, with only minor discrepancies visible for the turn maneuver in the approach phase to the target position. Initially, in the turn maneuver, the vehicle is accelerating, while steering to the right in order

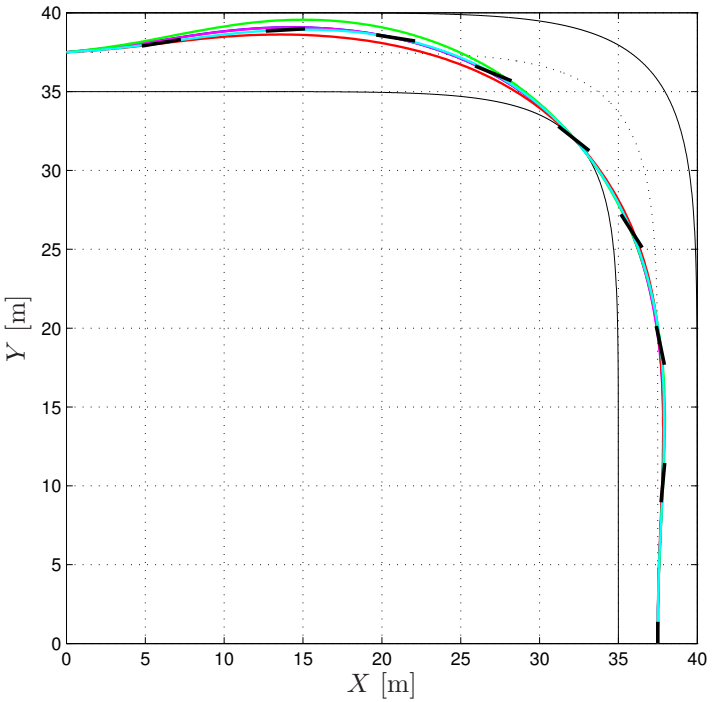

Figure 8.6 Geometric trajectory for the time-optimal maneuver obtained for the 90°-turn, for the single-track (blue), single-track with roll (magenta), single-track with pitch (red), the double-track with roll (green) and the double-track with roll and pitch (cyan) models. The black rectangles indicate the orientation of the vehicle every half second.

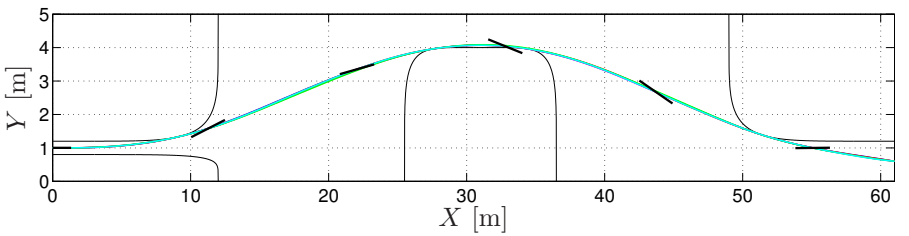

Figure 8.7 Geometric trajectory for the time-optimal maneuver obtained for the double lane-change situation. Same models and color scheme as in Figure 8.6. Note that the trajectories are close to each other for the different models. The black rectangles indicate the orientation of the vehicle every half second.

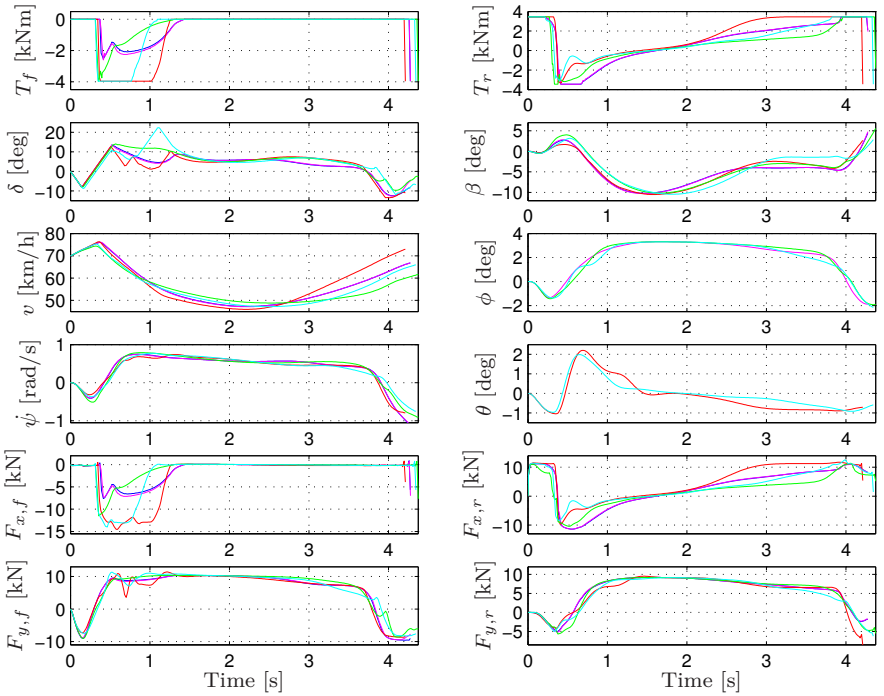

Figure 8.8 Model variables during the time-optimal maneuver obtained for the 90°-turn. Same models and color scheme as in Figure 8.6.

to allow for wider curve taking for all models. When approaching the sharp turn, the vehicle is decelerating by applying negative torques on the wheels, and then again accelerating when it has passed the turn and approaches the target position. Similarly, in the double lane-change maneuver, the optimal geometric trajectory is close to each other for all models. However, investigating the internal model variables in Figure 8.8 and Figure 8.9 closer, significant differences can be observed. These differences are discussed for each of the maneuvers next.

Turn Maneuver Considering the results for the 90°-turn in Figure 8.6 and Figure 8.8, it can be seen that the steering angle for the vehicle models with pitch dynamics and load transfer in the corresponding direction has a significant peak during the approach phase of the maneuver, not visible in the other models. The reason for this can be derived to the corresponding tire forces, where it is seen that these vehicle models have significantly larger longitudinal forces on the front tire than the other models have. Further, the pitch dynamics with load transfer results in significantly increased accel-

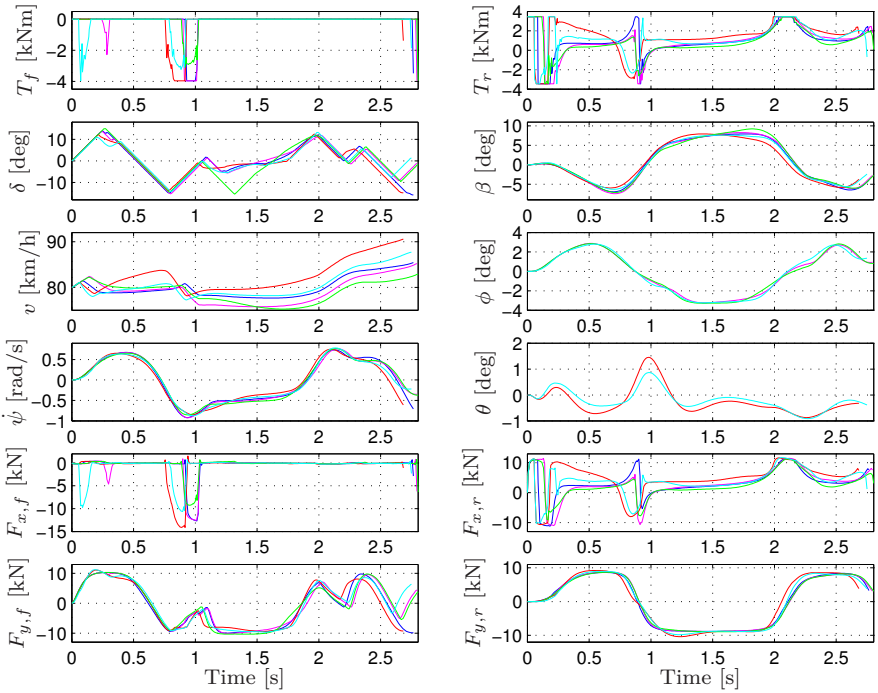

Figure 8.9 Model variables during the time-optimal maneuver obtained for the double lane-change situation. Same models and color scheme as in Figure 8.6.

eration and deceleration of the vehicle. To be specific, this means that the normal force on the rear driving wheels can be increased during the acceleration phases and similarly in the deceleration phases of the maneuvers. Thus, the velocity of the vehicle can be increased, which results in faster maneuver execution. The calculated times for completion of the optimal maneuver for the different model configurations A–E, are 4.27 s, 4.28 s, 4.21 s, 4.37 s, and 4.34 s, respectively.

Double Lane-Change Maneuver Investigating the optimal maneuvers in Figure 8.7 and Figure 8.9 for the different model configurations in the double lane-change situation, it is clear that the trajectories in the XY-plane are similar. This implies that the optimal geometric trajectory in this maneuver is not dependent on model configuration. However, as for the 90°-turn maneuver, the differences between the models appear in the internal state variables and inputs, in particular in the steering angle and the resulting tire forces. Specifically, the constraints on the steering angle and corresponding

change rate are active during a major part of the maneuver, indicating that the steering wheel input is essential in this maneuver. Further, it is interesting to consider the roll angle ϕ and the pitch angle θ. As can be seen in Figure 8.9, the roll angle is at most close to 4 deg, while the pitch angle is at most 1.5 deg during the maneuver. The roll angles in this case indicate that the vehicle is not overbalancing in the aggressive maneuver. Further, the noticeable pitch angle explains why the load transfer has effect on the achievable path velocity, similarly as for the turn maneuver discussed in the previous paragraph. The calculated execution times of the lane-change maneuver are 2.76 s, 2.79 s, 2.68 s, 2.80 s, and 2.75 s for model configurations A–E, respectively.

Optimal Maneuvers for Different Tire Models

In order to evaluate the different tire models, the time-optimal maneuver in the hairpin turn was determined for each of the four tire configurations. The vehicle chassis is modeled with the single-track model in (8.2)–(8.11), and is the same in all four cases. Further, the relaxation length was neglected for simplicity and the start, (X_p^0, Y_p^0), and final vehicle position,

$$(X_p^{t_f}, Y_p^{t_f}), \tag{8.44}$$

were set to be in the middle of the road. The initial velocity of the vehicle was $v_0 = 25$ km/h. Figures 8.10–8.13 display the geometric vehicle trajectory together with the internal model variables and steering input for the four different tire models. It is clear that all models have similarities: The vehicle starts with maximum acceleration, while turning in order to allow for wider curve taking. When entering the curve, the vehicle starts to brake with both wheels, which it does approximately until reaching the half-way point. Furthermore, all models exhibit large vehicle slip. The trajectory plots show that the slip—*i.e.*, the angle between the velocity vector and the longitudinal direction of the vehicle—is significant, exceeding 30 deg in the most critical parts of the maneuver.

The maneuvering of the vehicle, which achieves this behavior, is similar to techniques known to rally drivers as drifting, where the rear wheel driving and braking torque is used to control the rear lateral tire force, while the front wheels are only controlled with the steering angle. In addition, counter steering is utilized if necessary. Also, the qualitative slip behavior is congruent with the driving behavior often seen when rally drivers perform similar maneuvers, indicating that the obtained optimization results manage to replicate behavior utilized in reality. Furthermore, it also shows that even a few-state single-track model using the friction ellipse for tire modeling manages to capture fundamental and relevant behavior, also for minimum-time optimization problems resulting in aggressive behavior of the vehicle.

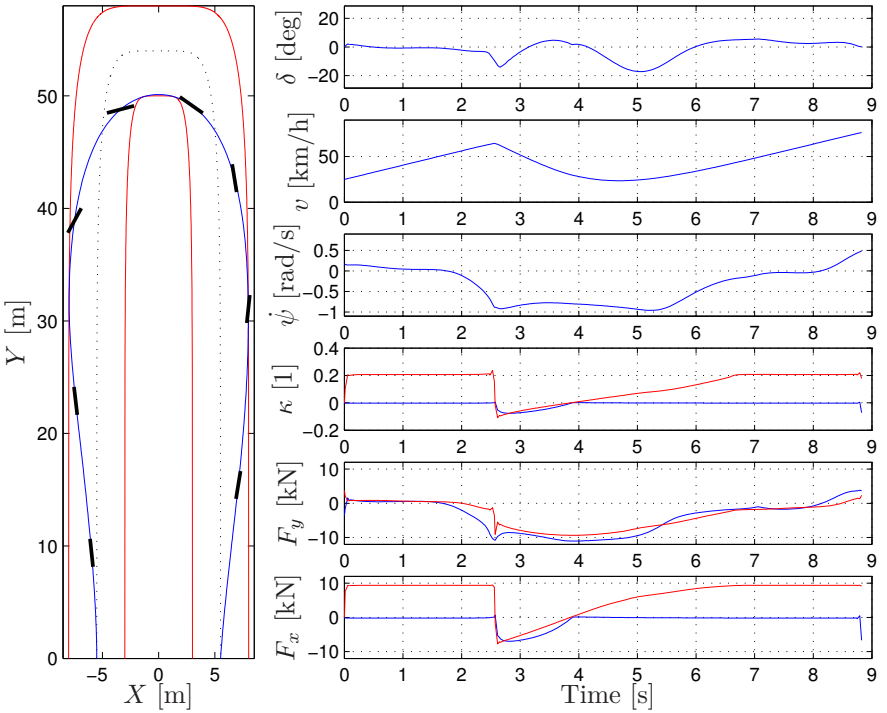

Figure 8.10 Optimization results for friction ellipse model with isotropic behavior with parameters as in column two in Table A.2 in Appendix A. In the κ, F_x, and F_y plots the blue curves visualize the front wheel and the red curves the rear wheel. The black rectangles in the XY-trajectory plot show the sideslip angle each second of the maneuver.

For the four different tire model configurations with parameters as in Table A.2 in Appendix A, the times for execution of the hairpin maneuver are for the respective column: 8.82 s, 8.42 s, 8.80 s, and 8.44 s. It is to be noted that the difference between the friction ellipse models and the weighting functions models for the respective tire is only minor. The main differences are between the isotropic and nonisotropic tire. This is not surprising, since the tire models for each category of tire were calibrated to be equal. The interesting observation is rather the essential effect of the tire characteristics on the resulting time-optimal maneuver.

Comparison of Isotropic Models The differences between the results obtained with the isotropic model with friction ellipse and weighting functions are minor, which is expected. However, this is a verification that the developed methodology is able to handle both of these tire models, and also that

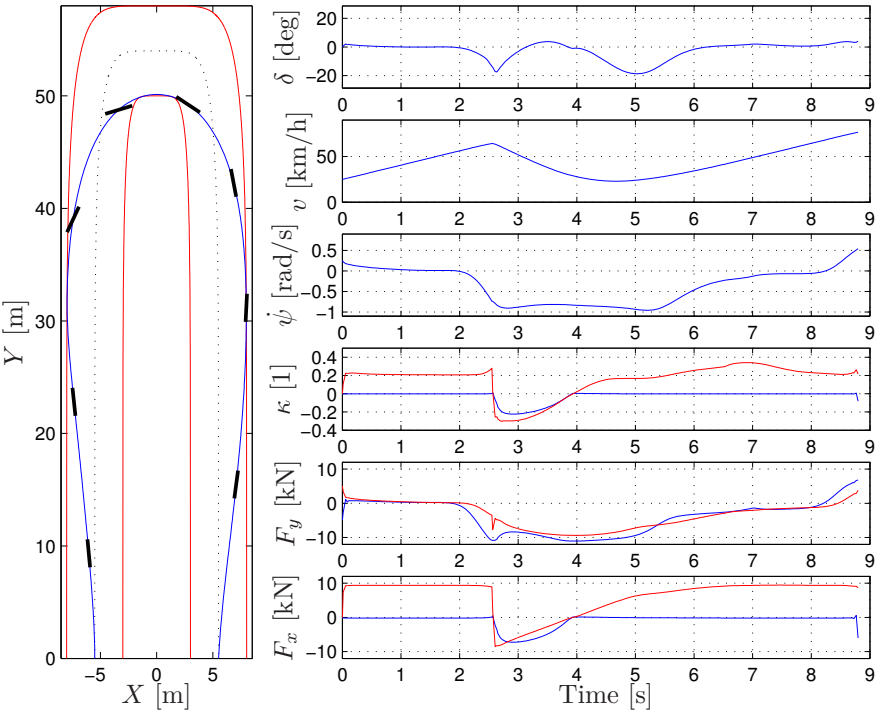

Figure 8.11 Optimization results for weighting functions model with isotropic behavior with parameters as in column four in Table A.2 in Appendix A. Same notation and colors as in Figure 8.10.

two completely different model categories, parametrized to achieve equivalent resultant force characteristics, give similar results for the optimal maneuver. Moreover, it is an indication that the optimization does not converge to different local minima for the considered model configurations.

To visualize the tire utilization, the tire forces for the front and rear wheels during the maneuver are plotted as function of the longitudinal slip κ and lateral slip α in the resulting tire force surfaces in Figures 8.14–8.15. These kind of plots are hereafter referred to as *Force-Slip (FS)-diagrams*. It is noted that the α and κ quantities, and consequently the resulting tire force trajectory, vary more for the rear wheels, which is natural since the vehicle is rear-wheel driven and thus implying more slip on these wheels.

Comparison of Nonisotropic Models When considering Figure 8.12 and Figure 8.13, it is observed that there are fundamental differences. First, the maximum steering angle δ in Figure 8.13 is twice as large as δ in Figure 8.12. Second, the maximum yaw rate is larger for the weighting func-

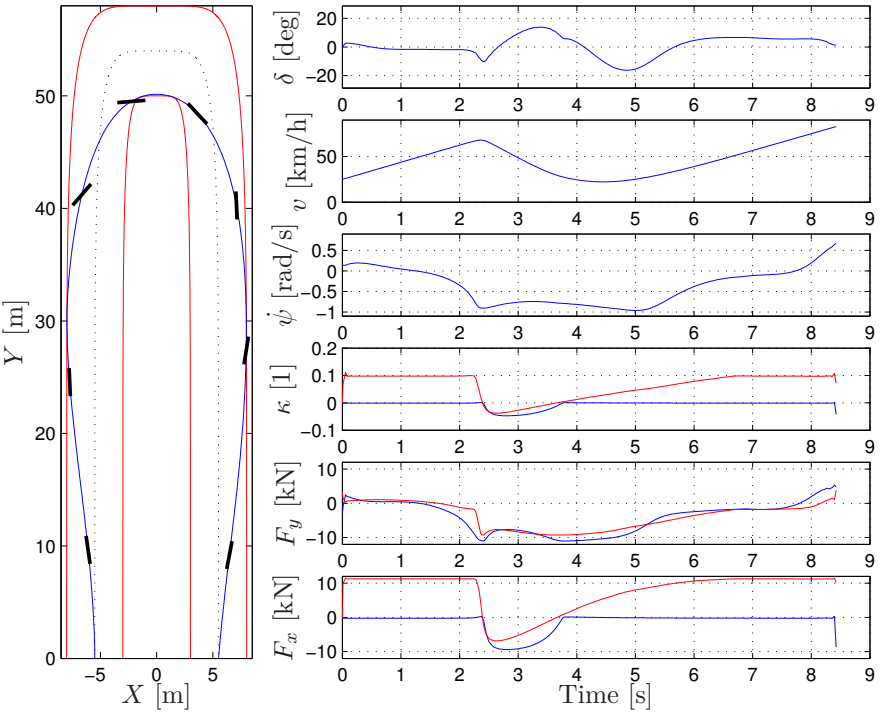

Figure 8.12 Optimization results for friction ellipse model with parameters as in column three in Table A.2 in Appendix A. Same notation and colors as in Figure 8.10.

tions model, but the yaw rate when in the turn—*i.e.*, in the time interval $t \in [3.5, 4.5]$ s—is smaller. Third, the weighting functions model seldom uses the rear wheel for braking. Rather, it maximizes the braking force on the front wheel instead of distributing the braking force to both wheels. It is plausible that this behavior is originating from that the weighting functions model provide, in addition to the low-slip solution, a large-slip alternative—*i.e.*, does not penalize combined slip—for a given resulting force. The FS-diagrams for the respective model are displayed in Figures 8.16–8.17. These plots indicate that this is indeed the case for this model. Further, the observations indicate that the obtained behavior is model dependent, rather than parameter dependent.

Considering the slip ratio κ for the different models, significant discrepancies can be observed. For the weighting functions model, a large peak occurs when increasing the yaw rate at $t \approx 2.3$ s. At this stage in the maneuver, when trying to turn the vehicle quickly, it is desired to have a small lateral

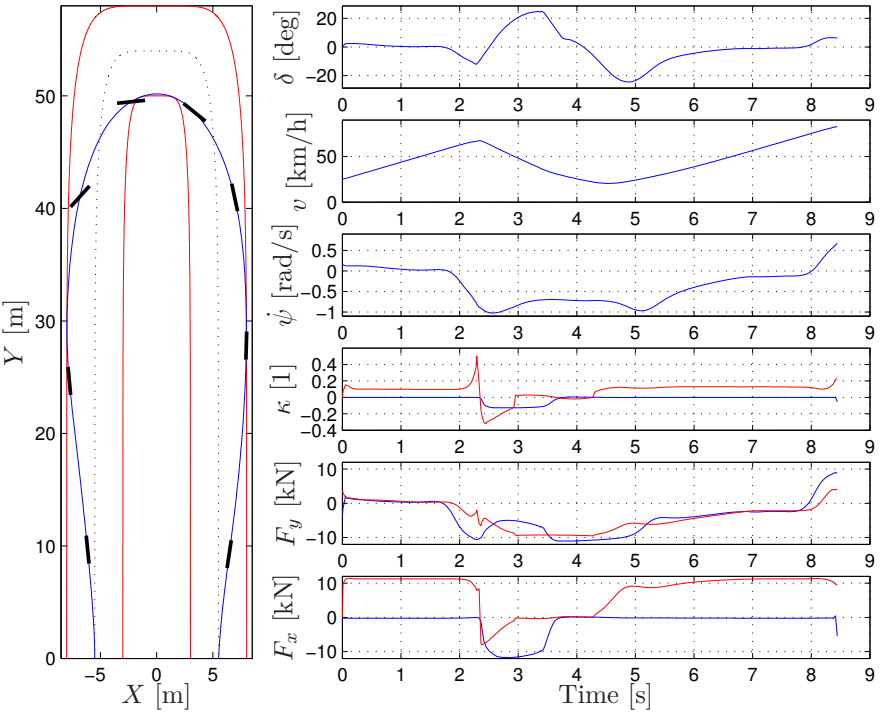

Figure 8.13 Optimization results for weighting functions model with parameters as in column five in Table A.2 in Appendix A. Same notation and colors as in Figure 8.10.

force at the rear, which, in the weighting functions model, can be achieved by increasing the slip ratio as much as possible.

Comparison of Isotropic and Nonisotropic Models Finally, when comparing the friction ellipse model for the two different parameter sets corresponding to two different tires—*i.e.*, the results displayed in Figure 8.10 and Figure 8.12—interesting observations can be made. The peak of the steering angle δ is more accentuated in Figure 8.12. Also, the longitudinal force, and thereby the longitudinal velocity, is larger in magnitude for the nonisotropic tire model, which is attributed to the larger longitudinal friction coefficient μ_x, see Table A.2 in Appendix A. This, in turn, is a result of the tire model calibration procedure used, described in Section 8.3. It is plausible that the difference in steering angle also can be derived to this, since a larger velocity will require more aggressive steering to counteract the larger forces. When comparing the tire forces during the maneuver in the FS-diagrams for these models, Figure 8.14 and Figure 8.16, it is clear that they are similar.

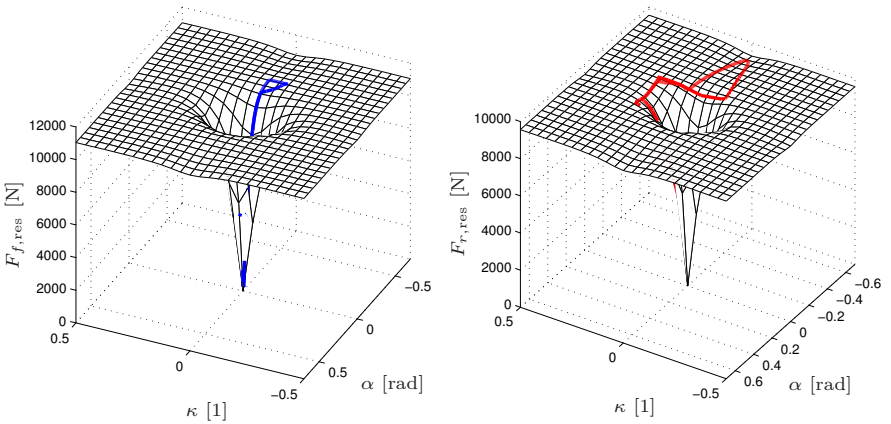

Figure 8.14 FS-diagram for the friction ellipse model with isotropic behavior. Blue (front wheel) and red curves (rear wheel) are the solution of the optimal control problem.

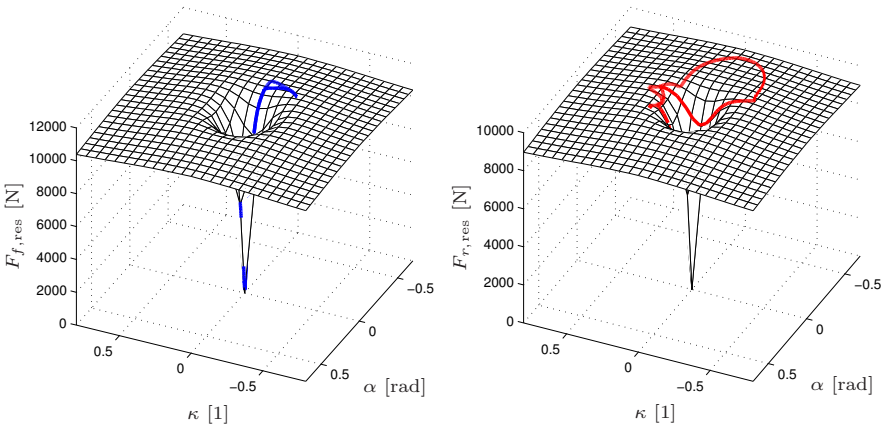

Figure 8.15 FS-diagram for the weighting functions model with isotropic parameters. Blue (front wheel) and red curves (rear wheel) are the solution of the optimal control problem.

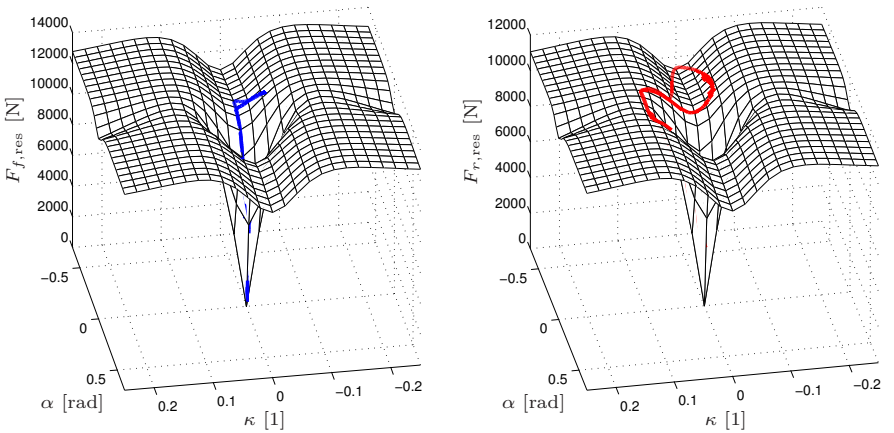

Figure 8.16 FS-diagram for the friction ellipse model with parameters according to column three in Table A.2 in Appendix A. Blue (front wheel) and red curves (rear wheel) are the solution of the optimal control problem.

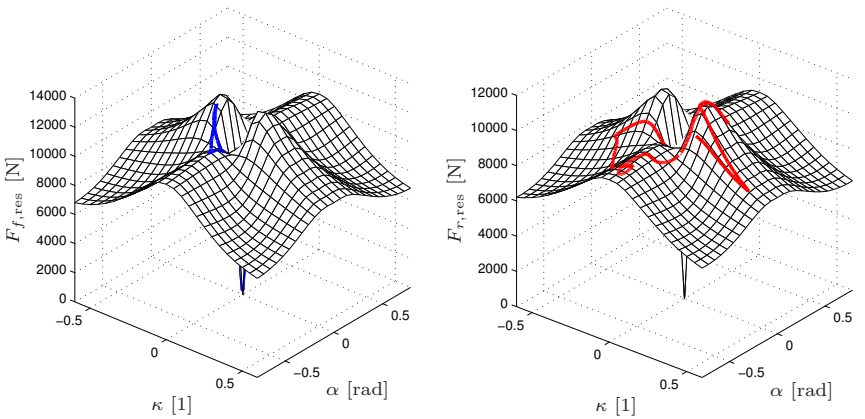

Figure 8.17 FS-diagram for the weighting functions model with parameters according to column five in Table A.2 in Appendix A. Blue (front wheel) and red curves (rear wheel) are the solution of the optimal control problem.

The models based on the weighting functions have more pronounced differences: First, the steering angle δ in Figure 8.11 is negative during the major part of the maneuver. Second, the yaw rate is larger in Figure 8.13. Third, the forces differ significantly. To some extent, the differences can be attributed to the difference in the longitudinal friction coefficient. A further explanation for this is the prominent peaks visible in the FS-diagram in Figure 8.17 for the nonisotropic tire model. Hence, the optimal solution in the two cases will depend on which slip combinations that result in maxima in the tire force surfaces.

8.6 Conclusions

This chapter of the thesis presented a methodology for determining optimal vehicle maneuvers in time-critical situations. Vehicle and tire models frequently encountered in the literature were employed and an optimal control problem was subsequently formulated. The overall aim was to give insight into improved safety systems. A comparison of the vehicle behavior for minimum-time optimal control in different maneuvers was presented. Five different vehicle models were compared in two maneuvers; a 90°-turn and a double lane-change situation. Two different tire models, with two parametrizations each, and a single-track vehicle model were used and evaluated in an aggressive hairpin maneuver.

Although the results differed in some respects, the qualitative behavior was similar for all models. It was shown that even a few-state single-track model using the friction ellipse for tire modeling managed to capture fundamental and relevant behavior. This implies that for future optimization-based safety systems, rather simplistic vehicle and tire models may be sufficient. However, the friction ellipse model and weighting functions model showed some dissimilarities. This might influence model choice in safety system development, especially when considering systems such as yaw-rate controllers where the brakes typically are utilized as the actuators. Further, the chassis modeling incorporating pitch dynamics as well as load transfer, exhibited significant differences compared to the basic single-track model. Consequently, adding this degree-of-freedom in the vehicle model might be necessary when, for example, considering optimal distribution of braking power to the different wheels in ESP systems.

9

Optimal Maneuvers on Uncertain Road-Surfaces

9.1 Introduction

In the previous chapter, a methodology for determining optimal road-vehicle maneuvers was presented. In this chapter, this methodology is applied to a case where the road-surface is uncertain—*i.e.*, the road is covered with snow or ice. The road-surface has, of course, significant effect on the tire forces that can be realized, and hence on the optimal control strategy for the vehicle in a maneuver. Scaling of nominal tire models for describing the behavior on different surfaces is theoretically described in [Pacejka, 2006] and subsequently experimentally measured and verified in [Braghin et al., 2006]. Even though the vehicle and tire models utilized in this thesis are similar to those discussed in the mentioned references, most investigations focus on a particular vehicle model on a specific surface. Comparisons of optimal control maneuvers for different road conditions have been made, see, *e.g.*, [Chakraborty et al., 2011], but are limited to varying the friction coefficient in the tire force model. In this chapter, it is shown that important tire-force characteristics in aggressive maneuvering situations are neglected with this approach. Consequently, the aim of this chapter is to propose a comprehensive approach to perform comparisons of optimal control maneuvers for different road conditions. This chapter is based on the publication [Olofsson et al., 2013].

The structure of this chapter is as follows: A background to and a description of the problem studied are given in Section 9.2. The modeling approach employed in this study is presented in Section 9.3. Section 9.4 presents the results achieved and a discussion of the optimal control solutions for the different road-surfaces is provided. Finally, the chapter is summarized and conclusions are drawn in Section 9.5.

9.2 Problem Description

One further step towards increasing the performance of vehicle safety systems is to study the behavior of a vehicle in a time-critical maneuver under varying road-surface conditions, *e.g.*, dry asphalt, wet asphalt, ice, and snow. Therefore, an investigation of the time-optimal vehicle maneuver in the hairpin turn considered in the previous chapter is performed for different road-surfaces. The vehicle and tire modeling principles developed in the previous chapter are utilized as basis models. Further, the optimal control problem proposed in the previous chapter is solved and the results thereof are presented for the different investigated road conditions. In addition, the problem of scaling of the tire models for different road-surface dynamics is discussed. With this study, it is plausible that the understanding of vehicle dynamics in at-the-limit maneuvering situations under road-surface uncertainties can be increased. It is thus probable that the results of such a study can be used for increasing the robustness of future vehicle safety systems.

9.3 Modeling

For modeling of the vehicle chassis and tires, the principles developed in Chapter 8 are employed. Since the primary influence of the road condition is on the tire-road interaction, the focus of the modeling is on the tire aspects. The vehicle chassis dynamics is modeled with a single-track model with roll dynamics, together with a wheel model and a Magic-Formula based tire model with weighting functions for modeling of combined longitudinal and lateral slip behavior.

Vehicle Modeling

The vehicle model used when determining the optimal maneuvers is the single-track model [Isermann, 2006; Ellis, 1994], see Figure 8.2 in Chapter 8. A rotational degree of freedom about the x-axis—*i.e.*, the roll dynamics—has been included in the model. The coordinate system is located in the ground plane at the xy-coordinates of the center-of-mass for zero roll angle. The motivation for the single-track model is twofold; first, the aim is to employ models possible to utilize together with dynamic optimization algorithms which require twice continuously differentiable functions and, second, it is of interest to investigate what properties of a vehicle that can be captured with this comparably simplistic model on the different road-surfaces. The roll dynamics has been included in the chassis model in order to verify that the vehicle is not overbalancing in the aggressive hairpin maneuver on high-friction surfaces. With the same notation as in Chapter 8, the equations for

the chassis model can be stated as

$$m\dot{v}_x = F_X + mv_y\dot{\psi} - mh\sin(\phi)\ddot{\psi} - 2mh\cos(\phi)\dot{\phi}\dot{\psi}, \tag{9.1}$$

$$m\dot{v}_y = F_Y - mv_x\dot{\psi} - mh\sin(\phi)\dot{\psi}^2 + mh\ddot{\phi}\cos(\phi) - m\dot{\phi}^2 h\sin(\phi), \tag{9.2}$$

$$\ddot{\psi} = \frac{M_Z - F_X h\sin(\phi)}{I_{zz}\cos^2(\phi) + I_{yy}\sin^2(\phi)}, \tag{9.3}$$

$$I_{xx}\ddot{\phi} = F_Y h\cos(\phi) + mgh\sin(\phi) + \dot{\psi}^2\Delta I_{yz}\sin(\phi)\cos(\phi) - K_\phi\phi - D_\phi\dot{\phi}, \tag{9.4}$$

$$F_X = F_{x,f}\cos(\delta) + F_{x,r} - F_{y,f}\sin(\delta), \tag{9.5}$$

$$F_Y = F_{y,f}\cos(\delta) + F_{y,r} + F_{x,f}\sin(\delta), \tag{9.6}$$

$$M_Z = l_f F_{y,f}\cos(\delta) - l_r F_{y,r} + l_f F_{x,f}\sin(\delta), \tag{9.7}$$

where h is the height of the center of mass, I_{xx}, I_{yy}, I_{zz} are the vehicle inertias about the x, y, and z-axis, respectively, $\Delta I_{yz} = I_{yy} - I_{zz}$, and F_X, F_Y, M_Z are the forces and moment acting on the center of mass. The roll dynamics was derived by assuming that the suspension system can be modeled as a rotational spring-damper system with stiffness K_ϕ and damping D_ϕ, see (8.12) in Chapter 8.

Wheel and Tire Modeling

The wheel dynamics is given by (8.5)–(8.11) in Chapter 8. However, the relaxation length was neglected in the study presented in this chapter for simplicity. The vehicle and wheel parameters used in this study are presented in Table A.1 in Appendix A.

The nominal tire forces—*i.e.*, the forces under pure slip conditions—are computed with the Magic Formula model [Pacejka, 2006]. In this chapter, a more comprehensive version of the tire model, with an extended set of model parameters, are utilized than what was the case in the study presented in Chapter 8. The model equations are given by

$$F_{x0,i} = \mu_x F_{z,i}\sin(C_{x,i}\arctan(B_{x,i}\kappa_i - E_{x,i}(B_{x,i}\kappa_i - \arctan(B_{x,i}\kappa_i)))), \tag{9.8}$$

$$F_{y0,i} = \mu_y F_{z,i}\sin(C_{y,i}\arctan(B_{y,i}\alpha_i - E_{y,i}(B_{y,i}\alpha_i - \arctan(B_{y,i}\alpha_i)))), \tag{9.9}$$

$$F_{z,i} = mg(l - l_i)/l,\ i \in \{f, r\},\ \text{where } l = l_f + l_r. \tag{9.10}$$

In (9.8)–(9.9), μ_x and μ_y are the friction coefficients and B, C, and E are model parameters. Combined slip is modeled using the weighting functions

presented in [Pacejka, 2006]:

$$B_{x\alpha,i} = B_{x1,i}\cos(\arctan(B_{x2,i}\kappa_i)), \tag{9.11}$$
$$G_{x\alpha,i} = \cos(C_{x\alpha,i}\arctan(B_{x\alpha,i}\alpha_i)), \tag{9.12}$$
$$F_{x,i} = F_{x0,i}G_{x\alpha,i}, \tag{9.13}$$
$$B_{y\kappa,i} = B_{y1,i}\cos(\arctan(B_{y2,i}\alpha_i)), \tag{9.14}$$
$$G_{y\kappa,i} = \cos(C_{y\kappa,i}\arctan(B_{y\kappa,i}\kappa_i)), \tag{9.15}$$
$$F_{y,i} = F_{y0,i}G_{y\kappa,i},\ i \in \{f, r\}. \tag{9.16}$$

The choice of the extended tire model and the weighting functions for modeling combined vehicle slip in this chapter, is based on the desire to be able to calibrate the models to represent the behavior of the tires on different road-surfaces. Moreover, considering the fact that a single-track model with lumped wheels are utilized here, the asymmetric parameters in the original complete Pacejka model have been recomputed such that the resulting model presented in (9.8)–(9.16) is symmetric with respect to the slip angle α and slip ratio κ.

Tire-Force Model Calibration

It is clear that the road-surface has a fundamental impact on the tire forces. Based on a set of tire parameters for a nominal surface, [Pacejka, 2006] proposes to use scaling factors λ_i in (9.8)–(9.16) in order to describe different road conditions. This method was used in [Braghin et al., 2006], where the scaling factors representing surfaces corresponding to dry asphalt, wet asphalt, snow, and smooth ice were estimated based on experimental data. In the investigation performed in this chapter, the scaling factors experimentally determined in [Braghin et al., 2006] are adopted as a basis for calibrating tire models approximately corresponding to the behavior on the different surfaces. The empirical tire model parameters presented in [Pacejka, 2006] are used to represent dry asphalt. With the dry asphalt model as base model, the scaling factors are introduced according to

$$\lambda_{\text{dry}} = 1, \quad \lambda_{\text{wet}} = \frac{\lambda^*_{\text{wet}}}{\lambda^*_{\text{dry}}}, \quad \lambda_{\text{snow}} = \frac{\lambda^*_{\text{snow}}}{\lambda^*_{\text{dry}}}, \quad \lambda_{\text{ice}} = \frac{\lambda^*_{\text{ice}}}{\lambda^*_{\text{dry}}}, \tag{9.17}$$

where λ is the scaling factor used in this study and λ^* is the scaling factor presented in [Braghin et al., 2006]. Considering that a different set of nominal parameters is used in this study, and that there are uncertainties in the estimation of the original scaling factors based on experimental data in [Braghin et al., 2006]—especially for larger slip values, where the experimental conditions are challenging—some inconsistent characteristics appear for the snow and ice models. The original tire model on the snow surface predicts a longitudinal force F_x that changes sign for increasing slip ratios, which is avoided

by slightly adjusting the scaling factor for C_x. For the model representing the ice surface, multiple sharp and narrow peaks in the resultant force occur. This is adjusted by recomputing the scaling factor affecting (9.14), as well as the parameters B_{x2} and B_{y2}. In addition, the lateral curvature factor E_y is also adjusted to smoothen the sharp peak, originating from the relations in (9.8)–(9.9). The complete set of tire model parameters used to represent the different surfaces are provided in Table A.3 in Appendix A. A subset of these parameters has been calculated with expressions depending on the normal force F_z on the wheel. Consequently, the front and rear parameter values differ—*e.g.*, the friction coefficients $\mu_{x,f}$ and $\mu_{x,r}$—because of the asymmetric location of the center-of-gravity of the vehicle chassis. The tire forces for the respective road-surface are visualized in Figures 9.4–9.7 in Section 9.4.

9.4 Results

To the purpose of investigating the time-optimal maneuver in the hairpin turn for the different road-surfaces, the optimal control problem (8.29)–(8.38) proposed in Chapter 8 was solved for each of the surface models discussed in Section 9.3. The road in the current study is 5 m wide and the vehicle is rear-wheel driven. The limitations on the driving and braking torques and tire forces were chosen as follows:

$$T_{f,\max} = 0, \tag{9.18}$$
$$T_{f,\min} = -\mu_x F_{z,f} R_w, \tag{9.19}$$
$$T_{r,\max} = \mu_x F_{z,r} R_w, \tag{9.20}$$
$$T_{r,\min} = -\mu_x F_{z,r} R_w, \tag{9.21}$$
$$F_{x,i,\max} = \mu_x F_{z,i}, \tag{9.22}$$
$$F_{y,i,\max} = \mu_y F_{z,i}, \ i \in \{f, r\}. \tag{9.23}$$

It is to be noted that with this choice of the maximum driving and braking torques, a dependency on the studied surface is introduced *via* the friction coefficients. This is motivated by that the surface models adopted in this study are only identified, and hence validated, for a certain region in the κ–α combined slip plane. Hence, allowing excess input torques might result in inconsistent behavior of the tire force model. Further, from a driver limitation argument, the steering angle and steering angle rate were constrained according to

$$\delta_{\max} = 30 \text{ deg} \quad , \quad \dot{\delta}_{\max} = 60 \text{ deg/s}, \tag{9.24}$$

similarly as for the maneuvers investigated in Chapter 8. In addition, the wheel angular velocities $\omega_{f,r}$ were constrained to be nonnegative—*i.e.*, the wheels were not allowed to roll backwards or back-spin in the maneuver.

With an initial velocity of $v_0 = 25$ km/h of the vehicle, the results displayed in Figures 9.1–9.2 were obtained. For comparison of the different road-surfaces, the model variables are visualized as function of the driven distance s instead of time. By this way of plotting the trajectories, the time dependency is implicit, but the control inputs relation to the different parts of the maneuver is more accentuated. Moreover, the geometric trajectories in the XY-plane corresponding to the time-optimal control strategies are presented in Figure 9.3.

The force–slip tire characteristic surfaces are also used as a basis for analysis, as introduced in Chapter 8. Plotting the optimal trajectory in the FS-diagram for both front and rear wheel, respectively, gives a presentation of the tire utilization, see Figures 9.4–9.7. The calculated times for execution of the maneuver are 8.48 s, 8.79 s, 13.83 s, and 19.18 s for dry asphalt, wet asphalt, snow, and smooth ice, respectively.

Discussion on Characteristics on Different Road-Surfaces

Considering the geometric trajectories in Figure 9.3 for the optimal maneuvers on the different surfaces, it can be concluded that the overall behavior is similar. As expected, the time for completing the maneuver is longer on the snow and ice surfaces than on asphalt. This is a result of that the tire forces that can be realized on these surfaces are significantly lower in magnitude than those on asphalt, *cf.* the friction coefficients for the different models in Table A.3 in Appendix A. Further, the vehicle exhibits high slip in the critical part of the maneuver on all surfaces except smooth ice. The explanation for this can be derived by examining the force characteristics of the smooth ice model compared to, *e.g.*, the dry asphalt model. In Figures 9.8 and 9.9 the longitudinal and lateral tire forces are shown for these surfaces, *cf.* the resulting tire forces in Figures 9.4 and 9.7. It is observed that the tire forces for smooth ice exhibit a considerably sharper peak and thus decay faster, with respect to combined longitudinal and lateral slip, than for dry asphalt. This means that combined slip yields a significantly smaller resulting tire force. Consequently, to achieve the desired time-optimality on the ice surface, it is natural that a small-slip control strategy should be chosen. This is also natural from an intuitive argument, since on the low-friction surfaces, maneuvering of the vehicle is critical and both the velocity and body slip must be reduced in order to be able to fulfill the geometric track-constraint.

Comparison of Control Strategies Investigating the internal variables of the vehicle and tire models during the maneuver closer, as displayed in Figures 9.1–9.2, it is clear that the behavior for dry and wet asphalt is similar. The similarity between dry and wet asphalt is expected, considering the tire force characteristics, see Figure 9.4 and Figure 9.5, which are similar in the two cases. The major difference between the two surfaces is the time for

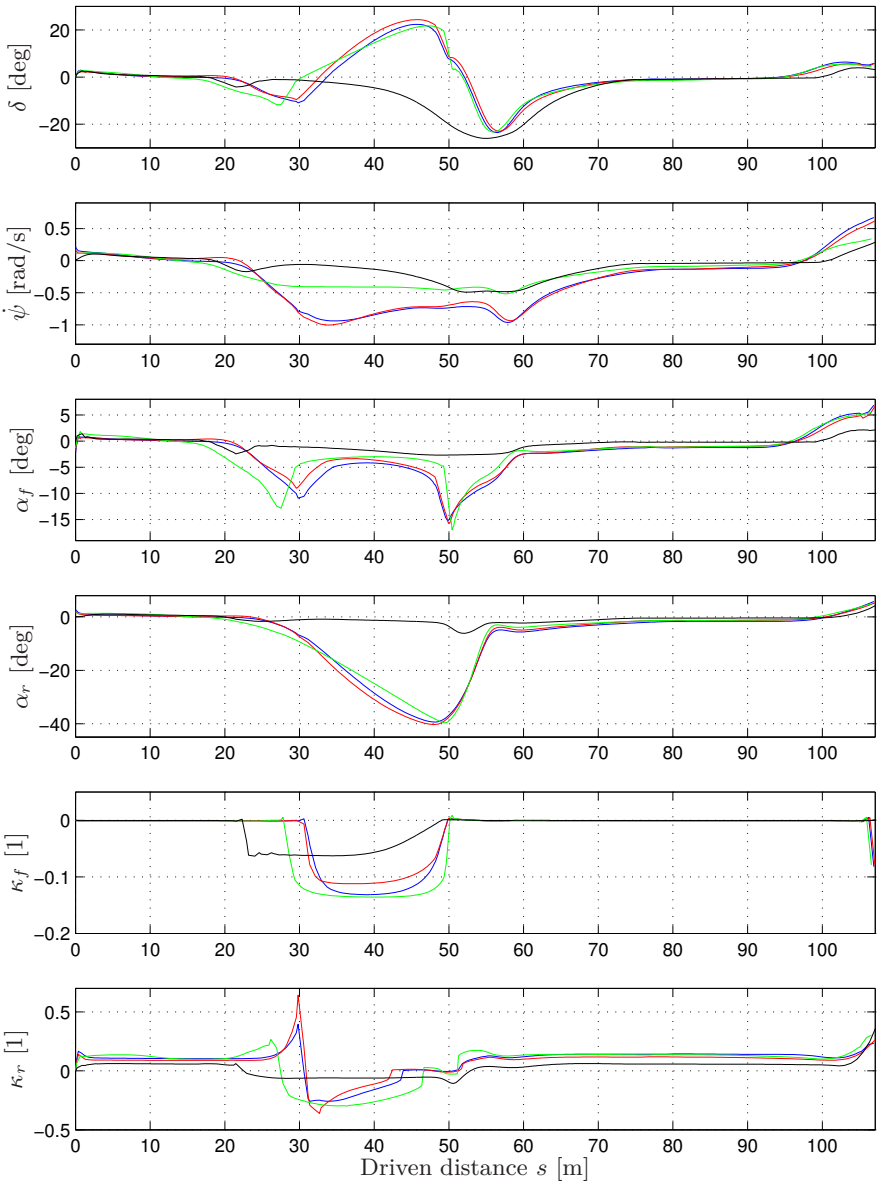

Figure 9.1 Variables of the vehicle model during the time-optimal hairpin maneuver on the different surfaces, plotted as function of the driven distance s. The color scheme is as follows: dry asphalt–blue, wet asphalt–red, snow–green, and smooth ice–black.

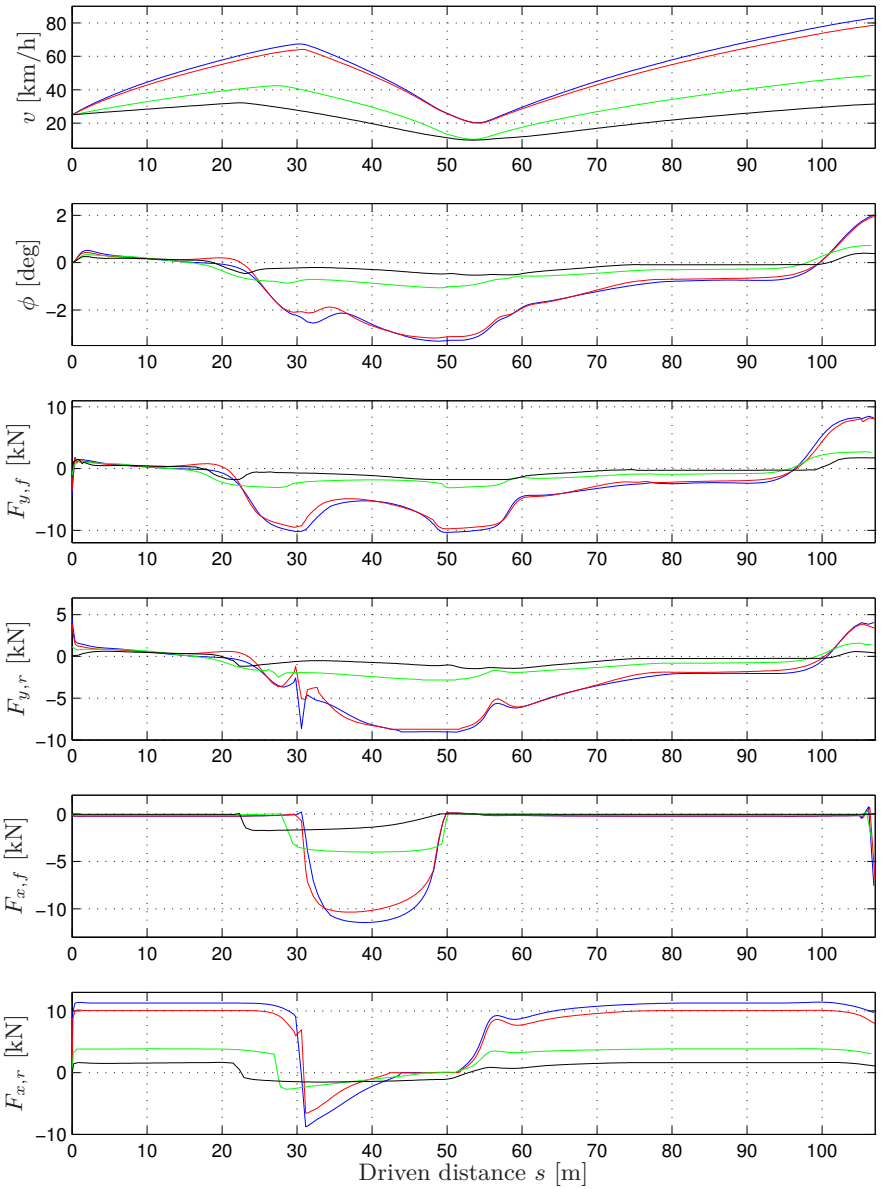

Figure 9.2 Variables of the vehicle model during the time-optimal hairpin maneuver on the different surfaces, plotted as function of the driven distance s. Same color scheme as in Figure 9.1.

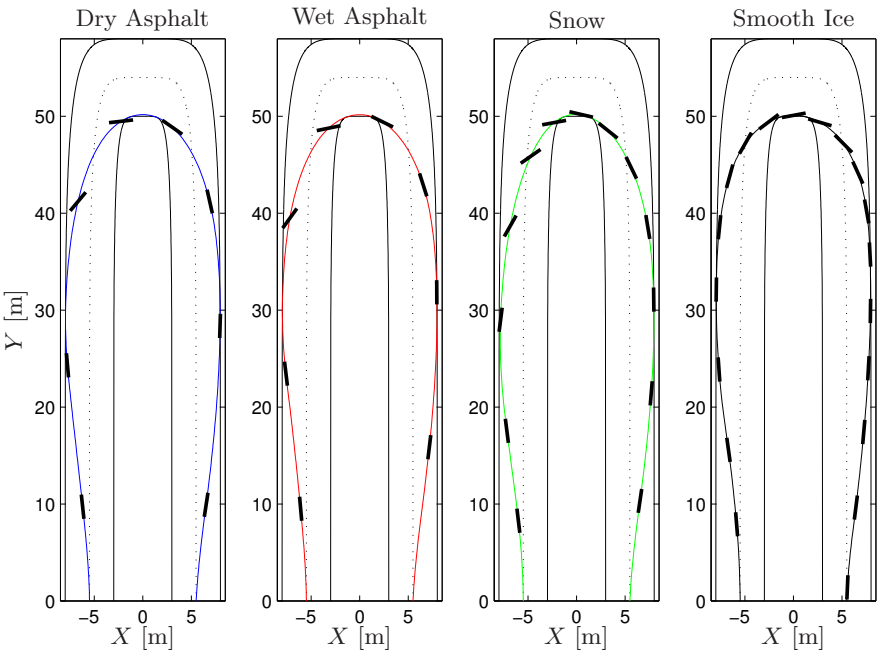

Figure 9.3 Trajectory in the XY-plane for the different road-surfaces. The black rectangles indicate the position and direction of the vehicle each second of the maneuver. The increase in the time for execution of the maneuver on the low-friction surfaces is clearly visible.

execution of the maneuver, which is slightly longer for the wet asphalt surface. This is expected since the friction coefficients—and thus the maximum tire forces that can be realized—are lower than for dry asphalt.

The differences between asphalt, snow, and ice when considering the fundamental control strategy are more pronounced. First, it can be concluded that the optimal maneuver on snow and ice surfaces are more proactive in the sense that both the steering angle δ and braking forces are applied considerably earlier when approaching the hairpin. This is most certainly an effect of the significantly reduced tire forces that can be realized on these surfaces compared to asphalt. Hence, the deceleration phase must be initiated earlier on the low-friction surfaces. The steering angle also differs between ice and the other surfaces. The reason for this is that the vehicle employs counter-steering when it starts to slip on asphalt and snow as it approaches the hairpin. This is not the case on the ice surface, where the slip is much smaller and the steering angle is thus not utilized to the same extent. Moreover, the roll angle is considerably smaller for the low-friction surfaces, which

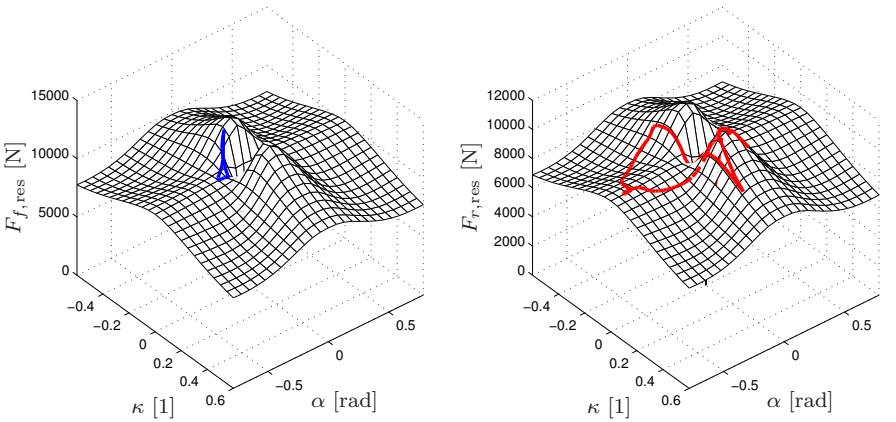

Figure 9.4 The resulting tire forces for the dry asphalt model in the time-optimal hairpin maneuver. The front tire force is shown in blue and the rear tire force is shown in red. The rear tire force exhibits more variation, which is caused by that the vehicle is rear-wheel driven.

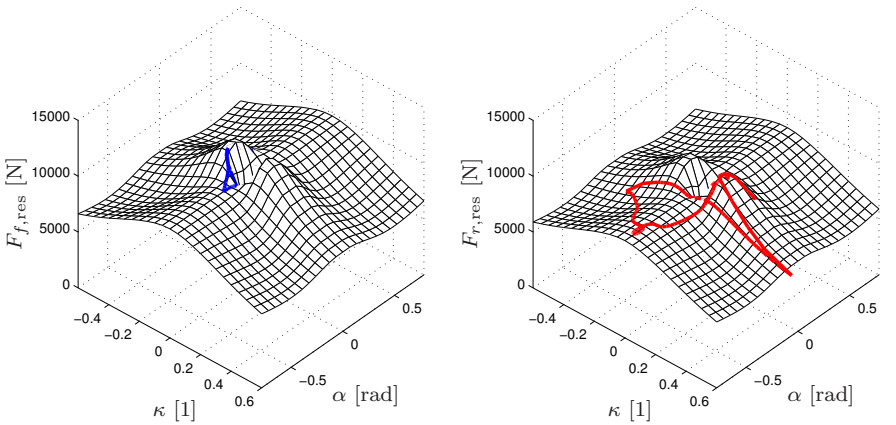

Figure 9.5 The resulting tire forces for the wet asphalt model in the time-optimal hairpin maneuver. The front tire force is shown in blue and the rear tire force is shown in red.

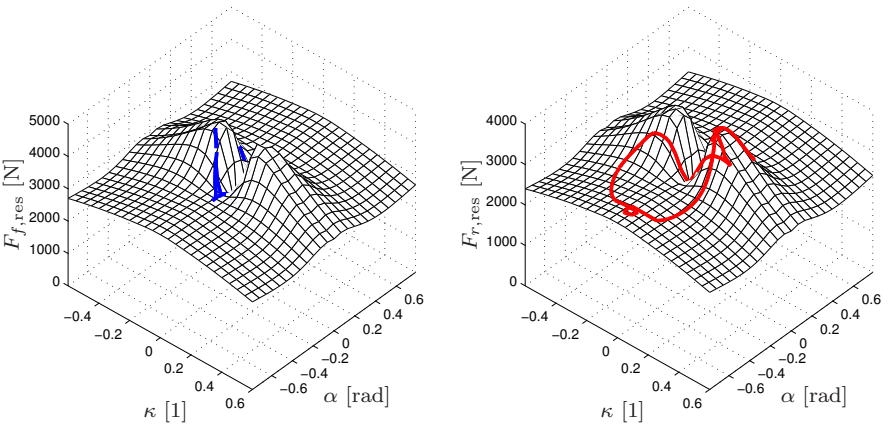

Figure 9.6 The resulting tire forces for the snow model in the time-optimal hairpin maneuver. The front tire force is shown in blue and the rear tire force is shown in red.

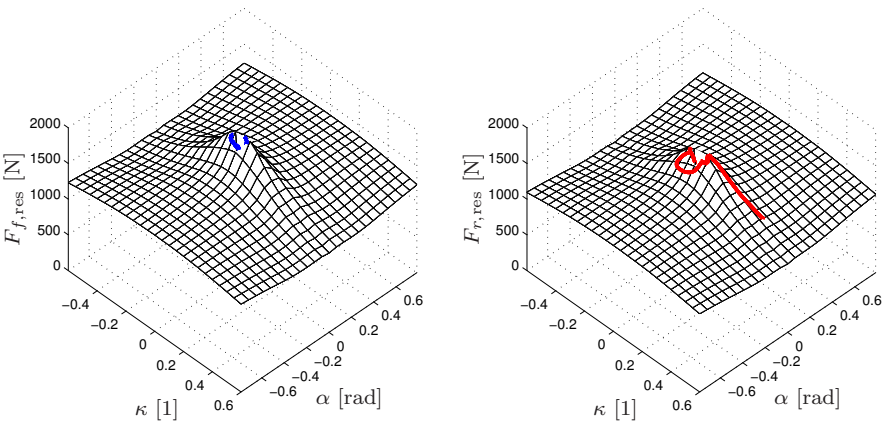

Figure 9.7 The resulting tire forces for the smooth ice model in the time-optimal hairpin maneuver. The front tire force is shown in blue and the rear tire force is shown in red.

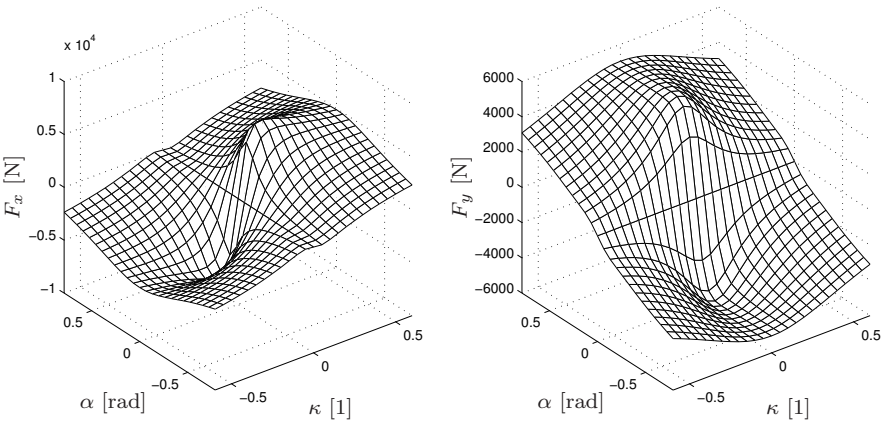

Figure 9.8 Front tire forces in the longitudinal and lateral wheel directions for dry asphalt, corresponding to Figure 9.4.

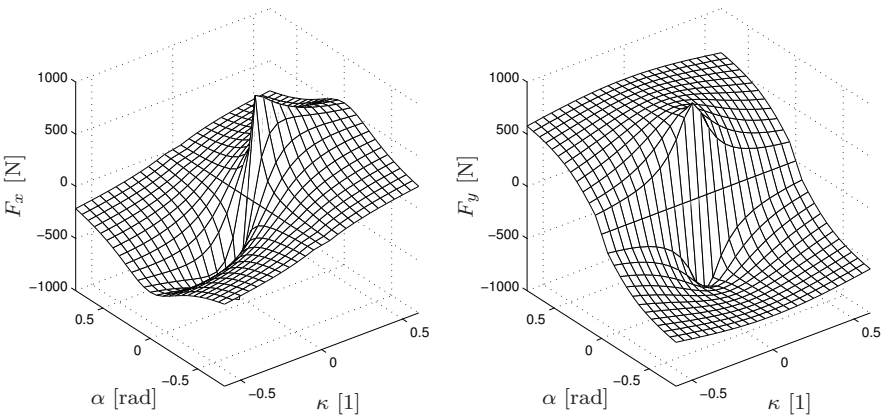

Figure 9.9 Front tire forces in the longitudinal and lateral wheel directions for ice, corresponding to Figure 9.7.

is a consequence of that the torque about the roll axis arising as a result of the tire–road contact is smaller. Further, even on dry asphalt, the roll angle is kept below approximately 3.2 deg, verifying that no unstable modes in the chassis dynamics are excited during the aggressive part of the hairpin maneuver. The slip ratio κ differs in amplitude between the surfaces, which is related to the differences in the acceleration and deceleration phases of the maneuver. More specifically, the reason becomes clear when investigating the tire forces in the FS-diagrams and the corresponding tire utilization, displayed in Figures 9.4–9.7. The peak of the resulting tire force in the κ–α plane occurs at smaller slip values when changing from high-friction to low-friction road surfaces. Consequently, in order to perform the maneuver in minimum time, it is natural that a control solution with smaller slip angles should be chosen.

Influence of Tire-Model on Optimal Maneuver Different approaches to model calibration were investigated prior to the study presented in this chapter. One approach would be to only scale the friction coefficients μ_x and μ_y, as mentioned in Section 9.1 and previously investigated in the literature. However, studying the force characteristics in Figures 9.4–9.7 closer, it can be observed that the maxima and minima in the resulting tire force surfaces occur at different lateral and longitudinal slip combinations. Also, the sharpness and width of the maxima and minima change for the different surface models. Consequently, only changing the friction coefficients will clearly result in different force characteristics compared to when changing the complete set of tire model parameters, as was the case for the models used in the study presented in this chapter. This implies that it is plausible that the resulting optimal maneuver will be different if this tire modeling approach is chosen. This is verified by constructing a tire force model where the dry asphalt model is used together with the friction coefficients corresponding to ice—*i.e.*, all parameters in the constructed model were equal to those in the dry asphalt model, except the friction coefficients. Solving the time-optimal control problem for the constructed model, see Figure 9.10, gives that the optimal solution has significant slip, on the contrary to the results obtained for the empirical smooth-ice model.

9.5 Conclusions

This chapter of the thesis investigated optimal road-vehicle maneuvers under uncertain and varying road conditions. The overall objective of the study was to gain insight into the dynamics when the vehicle and the tires perform at the limit. In addition, tire modeling required for realistic description of the tire force characteristics on different road-surfaces was discussed. It was shown that tire force modeling on different road-surfaces using only

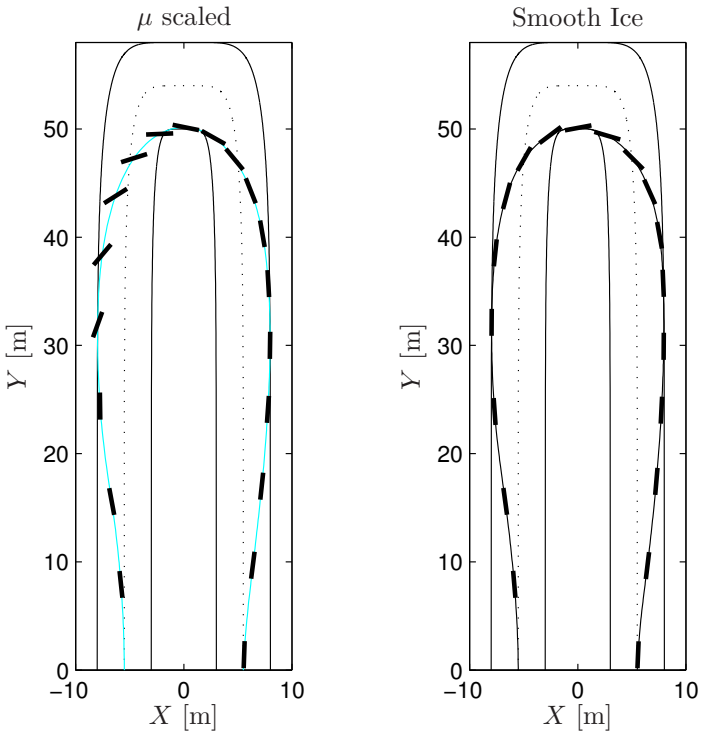

Figure 9.10 Results obtained by using the tire parameters for dry asphalt with the friction coefficients for the ice model (left plot). Comparing with scaling all tire parameters as in the empirical ice model (right plot), the time-optimal solution has significant slip for the constructed model.

a scaling of the friction coefficients seems to be insufficient, at least when considering that the tires perform at their limits. Rather, when combined longitudinal and lateral slip behavior is present, more careful tire modeling capturing the combinations of longitudinal and lateral slip that give maxima and minima in the tire force surface is required. The developed modeling and optimal control methodology proposed in Chapter 8 was applied to the minimum-time hairpin maneuvering problem, where tire models calibrated to describe different road-surfaces were investigated. The main conclusion from the achieved results is that tire models approximately corresponding to different road characteristics, such as dry asphalt and ice, imply fundamentally different driving techniques for achieving the optimal maneuver. This is considered as important findings towards the goal of developing new vehicle safety systems robust to road-surface uncertainties.

10

Conclusions and Future Work

In this part of the thesis, a methodology for solution of optimal control problems for road-vehicles in time-critical situations was proposed. The methodology was subsequently evaluated using different principles for vehicle chassis and tire modeling. A time-optimal criterion was considered in the optimization, with the aim of triggering extreme modes in the vehicle dynamics and find performance limits, thus providing a basis for future development of vehicle safety systems. In addition, the effect on the optimal maneuver when the road-surface is changed was investigated. The main conclusion from the presented simulation results is that even rather simplistic vehicle and tire models, neglecting detailed gear and suspension kinematics for example, are able to replicate behavior observed in reality performed by experienced drivers in similar situations. Further, significant differences between the optimal driving behavior on the different road-surfaces were observed. These are both considered as important results towards the goal of having online optimization-based vehicle safety and driver assistance technologies.

For the future, the optimization results presented in this thesis can be used for creating a library for optimal vehicle maneuvers to be applied online in a vehicle using real-time scheduling. In this context, other optimization criteria than the final time, such as control signal utilization, when determining the maneuvers are of interest. Further, a natural extension of the work presented in this thesis is trajectory generation for path tracking with vehicles. This is of interest in, for example, ESP systems, where it is essential that the vehicle stays within its current road lane even with significant body and side slip. In particular, investigating how the methods developed for trajectory generation for path tracking with stationary and mobile robots, see [Olofsson et al., 2011b] and [Berntorp et al., 2013a], can be extended to the case of road-vehicles are natural future work of the results presented in this thesis.

Bibliography

ABB Robotics (2012). *ABB IRB2400 Industrial Robot Data sheet*. Data sheet nr. PR10034 EN_R7.

Abele, E., J. Bauer, T. Hemker, R. Laurischkat, H. Meier, S. Reese, and O. von Stryk (2011). "Comparison and validation of implementations of a flexible joint multibody dynamics system model for an industrial robot". *CIRP J. Manufacturing Science and Technology* **4**:1, pp. 38–43.

Abele, E., S. Rothenbücher, and M. Weigold (2008). "Cartesian compliance model for industrial robots using virtual joints". *Prod. Eng. Res. Devel.* **2**, pp. 339–343.

Åkesson, J. (2008). "Optimica—an extension of Modelica supporting dynamic optimization". In: *6th Int. Modelica Conf. 2008*. Modelica Association. URL: `https://www.modelica.org/events/modelica2008/Proceedings/sessions/session1b3.pdf`.

Åkesson, J., K.-E. Årzén, M. Gäfvert, T. Bergdahl, and H. Tummescheit (2010). "Modeling and optimization with Optimica and JModelica.org—Languages and tools for solving large-scale dynamic optimization problems". *Computers and Chemical Engineering* **34**:11, pp. 1737–1749.

Al Janaideh, M., Y. Feng, S. Rakheja, C.-Y. Su, and C. Alain Rabbath (2009). "Hysteresis compensation for smart actuators using inverse generalized Prandtl-Ishlinskii model". In: *Proc. Am. Control Conf. (ACC)*. St. Louis, MO, pp. 307–312.

Anderson, S., S. Peters, T. Pilutti, and K. Iagnemma (2010). "An optimal-control-based framework for trajectory planning, threat assessment, and semi-autonomous control of passenger vehicles in hazard avoidance scenarios". *Int. J. Vehicle Autonomous Systems* **8**:2/3/4, pp. 190–216.

Anderson, S., S. Karumanchi, and K. Iagnemma (2012). "Constraint-based planning and control for safe, semi-autonomous operation of vehicles". In: *IEEE Intelligent Vehicles Symp.* Alcalá de Henares, Spain, pp. 383–388.

Andreasson, J. (2009). "Enhancing active safety by extending controllability — How much can be gained?" In: *IEEE Intelligent Vehicles Symp.* Xi'an, Shaanxi, China, pp. 658–662.

Åström, K. J. and B. Wittenmark (1997). *Computer-Controlled Systems*. Prentice Hall, Englewood Cliffs, NJ.

Bauer, H., K.-H. Dietsche, J. Crepin, and F. Dinkler, eds. (2000). *Automotive Handbook*. 5th edition. Robert Bosch GmbH.

Berntorp, K., B. Olofsson, and A. Robertsson (2013a). "Path tracking with obstacle avoidance for pseudo-omnidirectional mobile robots using convex optimization". In: *Proc. Conf. Decision and Control (CDC)*. Firenze, Italy. *Submitted*.

Berntorp, K. (2013). *Derivation of a Six Degrees-of-Freedom Ground-Vehicle Model for Automotive Applications*. Tech. rep. LUTFD2/TFRT–7627–SE. Dept. of Automatic Control, Lund University, Lund, Sweden. URL: `http://www.control.lth.se/Publication/7627.html`.

Berntorp, K., B. Olofsson, K. Lundahl, B. Bernhardsson, and L. Nielsen (2013b). "Models and methodology for optimal vehicle maneuvers applied to a hairpin turn". In: *Am. Control Conf. (ACC)*. Washington, D.C. *Accepted for publication*.

Biegler, L. T., A. M. Cervantes, and A. Wächter (2002). "Advances in simultaneous strategies for dynamic process optimization". *Chemical Engineering Science* **57**, pp. 575–593.

Bittencourt, A. C., E. Wernholt, S. Sander-Tavallaey, and T. Brogårdh (2010). "An extended friction model to capture load and temperature effects in robot joints". In: *Proc. IEEE/RSJ Int. Conf. on Intelligent Robots and Systems (IROS)*. Taipei, Taiwan, pp. 6161–6167.

Blomdell, A., G. Bolmsjö, T. Brogårdh, P. Cederberg, M. Isaksson, R. Johansson, M. Haage, K. Nilsson, M. Olsson, T. Olsson, A. Robertsson, and J. Wang (2005). "Extending an industrial robot controller—Implementation and applications of a fast open sensor interface". *IEEE Robotics & Automation Magazine* **12**:3, pp. 85–94.

Blomdell, A., I. Dressler, K. Nilsson, and A. Robertsson (2010). "Flexible application development and high-performance motion control based on external sensing and reconfiguration of ABB industrial robot controllers". In: *Proc. workshop of "Innovative Robot Control Architectures for Demanding (Research) Applications—How to Modify and Enhance Commercial Controllers", IEEE Int. Conf. on Robotics and Automation (ICRA)*. Anchorage, AK, pp. 62–66.

Braghin, F., F. Cheli, and E Sabbioni (2006). "Environmental effects on Pacejka's scaling factors". *Vehicle System Dynamics: Int. J. Vehicle Mechanics and Mobility* **44**:7, pp. 547–568.

Brokate, M. and J. Sprekels (1996). *Hysteresis and Phase Transitions*. Springer-Verlag, New York.

Carlson, C. and J. Gerdes (2005). "Consistent nonlinear estimation of longitudinal tire stiffness and effective radius". *IEEE Trans. Control Syst. Technol.* **13**:6, pp. 1010–1020.

Chakraborty, I., P. Tsiotras, and J. Lu (2011). "Vehicle posture control through aggressive maneuvering for mitigation of T-bone collisions". In: *IEEE Conf. on Decision and Control (CDC)*. Orlando, FL, pp. 3264–3269.

COMET (2013). EU/FP7-project: *Plug-and-produce COmponents and METhods for adaptive control of industrial robots enabling cost effective, high precision manufacturing in factories of the future*. URL: `http://www.cometproject.eu`.

Denavit, J. and R. S. Hartenberg (1955). "A kinematic notation for lower-pair mechanisms based on matrices". *Trans. ASME J. Appl. Mech.* **23**, pp. 215–221.

dSPACE GmbH (2007). *DS1103 PPC Controller Board—Hardware Installation and Configuration*. dSPACE GmbH, Paderborn, Germany.

Ellis, J. R. (1994). *Vehicle Handling Dynamics*. Mechanical Engineering Publications, London, United Kingdom.

Fasse, E. and N. Hogan (1995). "Control of physical contact and dynamic interaction". In: *Proc. 7th Int. Symp. Robotics Research*. Munich, Germany, pp. 28–38.

Funke, J., P. Theodosis, R. Hindiyeh, G. Stanek, K. Kritatakirana, C. Gerdes, D. Langer, M. Hernandez, B. Muller-Bessler, and B. Huhnke (2012). "Up to the limits: Autonomous Audi TTS". In: *IEEE Intelligent Vehicles Symp.* Alcalá de Henares, Spain, pp. 541–547.

Ge, P. and M. Jouaneh (1996). "Tracking control of a piezoceramic actuator". *IEEE Trans. Control Syst. Technol.* **4**:3, pp. 209–216.

Hastie, T., R. Tibshirani, and J. Friedman (2008). *The Elements of Statistical Learning*. Springer-Verlag, New York.

Haverkamp, B. and M. Verhaegen (1997). *SMI Toolbox: State Space Model Identification Software for Multivariable Dynamical Systems*. Delft University of Technology, Delft, The Netherlands.

Hovland, G., S. Hanssen, S. Moberg, T Brogårdh, S. Gunnarson, and M. Isaksson (2002). *Nonlinear identification of backlash in robot transmissions*. ISR 2002 Int. Symp. on Robotics, Stockholm, Sweden.

Isermann, R. (2006). *Fahrdynamik-Regelung: Modellbildung, Fahrerassistenzsysteme, Mechatronik*. Vieweg-Verlag, Wiesbaden, Germany.

JModelica.org (2013). URL: `http://www.jmodelica.org`.

Johansson, R. (1993). *System Modeling and Identification*. Prentice Hall, Englewood Cliffs, NJ.

Kalman, R. E. (1960). "A new approach to linear filtering and prediction problems". *Trans. of the ASME—J. of Basic Engineering* **82**:D, pp. 35–45.

Kelly, D. P. and R. S. Sharp (2010). "Time-optimal control of the race car: a numerical method to emulate the ideal driver". *Vehicle System Dynamics* **48**:12, pp. 1461–1474.

Keyence Corp. (2006). *LK-G Series User Manual*. Keyence Corp., Osaka, Japan.

Khalil, H. K. (2002). *Nonlinear Systems*. Prentice Hall, Upper Saddle River, New Jersey.

Kiencke, U. and L. Nielsen (2005). *Automotive Control Systems—For Engine, Driveline and Vehicle*. 2nd edition. Springer-Verlag, Berlin Heidelberg, Germany.

Krasnosel'skii, M., A. Pokrovskii, and M. Niezgódka (1989). *Systems with Hysteresis*. Springer, Berlin Heidelberg, Germany.

Krejci, P. and K. Kuhnen (2001). "Inverse control of systems with hysteresis and creep". In: *IEE Proc. Control Theory and Applications*. Vol. 148. 3, pp. 185–192.

Krylov, N. M. and N. N. Bogoliubov (1947). *Introduction to Nonlinear Mechanics*. Princeton University Press, Princeton, NJ.

Lehmann, C., B. Olofsson, K. Nilsson, M. Halbauer, M. Haage, A. Robertsson, O. Sörnmo, and U. Berger (2013). "Robot joint modeling and parameter identification using the clamping method". In: *IFAC Conf. on Manufacturing Modelling, Management, and Control (MIM)*. St. Petersburg, Russia. *Accepted for publication*.

Lei, L., K. K. Tan, S. Huang, and T. H. Lee (2011). "Online parameter estimation and compensation of Preisach hysteresis by SVD updating". In: *Proc. 18th IFAC World Congress*. Milano, Italy, pp. 5249–5254.

Li, Y. and Q. Xu (2011). "A totally decoupled piezo-driven XYZ flexure parallel micropositioning stage for micro/nanomanipulation". *IEEE Trans. Automation Science and Eng.* **8**:20, pp. 265–279.

Liaw, H. C. and B. Shirinzadeh (2010). "Constrained motion tracking control of piezo-actuated flexure-based four-bar mechanisms for micro/nano manipulation". *IEEE Trans. Automation Science and Eng.* **7**:3, pp. 699–705.

Liebemann, K., K. Meder, J. Schuh, and G. Nenninger (2005). "Safety and performance enhancement: the Bosch electronic stability control". Paper Number 05-0471m, Robert Bosch GmbH. Germany.

Ljung, L. (2010). *System Identification Toolbox 7: Users's Guide*. The MathWorks, Inc., Natick, MA.

Lundahl, K., K. Berntorp, B. Olofsson, J. Åslund, and L. Nielsen (2013). "Studying the influence of roll and pitch dynamics in optimal road-vehicle maneuvers". In: *Int. Symp. on Dynamics of Vehicles on Roads and Tracks (IAVSD)*. Qingdao, China. *Accepted for publication*.

Lundahl, K., J. Åslund, and L. Nielsen (2011). "Investigating vehicle model detail for close to limit maneuvers aiming at optimal control". In: *22nd Int. Symp. on Dynamics of Vehicles on Roads and Tracks (IAVSD)*. Manchester, United Kingdom.

Madsen, H. (2008). *Time Series Analysis*. Chapman & Hall/CRC, Boca Raton, FL.

Mahr GmbH (2011). *MarSurf M 400 Flyer*. Mahr GmbH, Göttingen, Germany.

MathWorks Inc. (2010). *Real-Time Workshop 7: Users's Guide*. The MathWorks, Inc., Natick, MA.

Menold, P. H., R. K. Pearson, and F. Allgöwer (1999). "Online outlier detection and removal". In: *Proc. of the 7th Mediterranean Conf. on Control and Automation (MED99)*. Haifa, Israel, pp. 1110–1133.

Modelica Association (2013). URL: `http://www.modelica.org`.

Nikon Metrology (2010). *K-series optical CMM solutions*. Data sheet Optical_CMM_EN_0311.

Nilsson, K. and R. Johansson (1999). "Integrated architecture for industrial robot programming and control". *J. Robotics and Autonomous Systems* **29**:4, pp. 205–226.

Olofsson, B, O Sörnmo, U Schneider, A Robertsson, A Puzik, and R Johansson (2011a). "Modeling and control of a piezo-actuated high-dynamic compensation mechanism for industrial robots". In: *Proc. IEEE/RSJ Int. Conf. on Intelligent Robots and Systems (IROS)*. San Francisco, CA, pp. 4704–4709.

Olofsson, B., H. Nilsson, A. Robertsson, and J. Åkesson (2011b). "Optimal tracking and identification of paths for industrial robots". In: *Proc. 18th World Congress of the Int. Federation of Automatic Control (IFAC)*. Milano, Italy, pp. 1126–1132.

Olofsson, B., O. Sörnmo, U. Schneider, M. Barho, A. Robertsson, and R. Johansson (2012). "Increasing the accuracy for a piezo-actuated micro manipulator for industrial robots using model-based nonlinear control". In: *10th Int. IFAC Symp. on Robot Control (SYROCO)*. Dubrovnik, Croatia, pp. 277–282.

Olofsson, B., K. Lundahl, K. Berntorp, and L. Nielsen (2013). "An investigation of optimal vehicle maneuvers for different road conditions". In: *7th IFAC Symp. on Advances in Automotive Control (AAC)*. Tokyo, Japan. *Submitted*.

Olsson, H. (1996). *Control Systems with Friction*. ISRN LUTFD2/TFRT–1045–SE. Department of Automatic Control, Lund University, Sweden. URL: `http://www.control.lth.se/Publication/olsh96dis.html`.

Overschee, P. van and B. De Moor (1994). "N4SID: subspace algorithms for the identification of combined deterministic-stochastic systems". *Automatica* **30**:1, pp. 75–93.

Pacejka, H. B. (2006). *Tyre and Vehicle Dynamics*. 2nd edition. Butterworth-Heinemann, Oxford, United Kingdom.

Pan, Z. and H. Zhang (2009). "Improving robotic machining accuracy by real-time compensation". In: *Proc. ICROS-SICE Int. Joint Conf. 2009*. Fukuoka, Japan, pp. 4289–4294.

Preisach, F. (1935). "Über die magnetische Nachwirkung". *Zeitschrift für Physik* **94** (5–6), pp. 277–302.

Puzik, A., A. Pott, C. Meyer, and A. Verl (2009). "Industrial robots for machining processes in combination with an additional actuation mechanism for error compensation". In: *7th Int. Conf. on Manufacturing Research (ICMR)*. University of Warwick, United Kingdom.

Puzik, A., C. Meyer, and A. Verl (2010). "Results of robot machining with additional 3D-piezo-actuation-mechanism for error compensation". In: *7th CIRP Int. Conf., Intelligent Computation in Manufacturing Eng.: Innovative and Cognitive Production Technology and Systems*. Capri, Italy.

Puzik, A. (2011). *Genauigkeitssteigerung bei der spanenden Bearbeitung mit Industrierobotern durch Fehlerkompensation mit 3D Ausgleichsaktorik*. PhD dissertation. University of Stuttgart, Stuttgart, Germany.

Rajamani, R. (2006). *Vehicle Dynamics and Control*. Springer-Verlag, Berlin Heidelberg, Germany.

Reis GmbH (2011). *Reis RV40 Fact Sheet*. Reis GmbH, Obernburg, Germany.

Ruderman, M., F. Hoffmann, and T. Bertram (2009). "Modeling and identification of elastic robot joints with hysteresis and backlash". *IEEE Trans. Ind. Electron.* **56**:10, pp. 3840–3847.

Schindler, E. (2007). *Fahrdynamik: Grundlagen Des Lenkverhaltens Und Ihre Anwendung Für Fahrzeugregelsysteme*. Expert-Verlag, Renningen, Germany.

Schneider, U. (2010). *Regelung einer 3D-Ausgleichsaktorik für Fräsanwendungen mit Industrierobotern*. Diploma Thesis. Fraunhofer Institute for Manufacturing and Engineering, Stuttgart, Germany.

Sharon, A., N. Hogan, and D. E. Hardt (1993). "The macro/micro manipulator: an improved architecture for robot control". *Robotics & Computer-Integrated Manufacturing* **10**:3, pp. 209–222.

Sharp, R. S. and H. Peng (2011). "Vehicle dynamics applications of optimal control theory". *Vehicle System Dynamics* **49**:7, pp. 1073–1111.

Siciliano, B., L. Sciavicco, L. Villani, and G. Oriolo (2009). *Robotics: Modelling, Planning and Control*. Springer-Verlag, London.

Slotine, J. J. E. and W. Li (1991). *Applied Nonlinear Control*. Prentice Hall, Upper Saddle River, NJ.

Sörnmo, O., B. Olofsson, U. Schneider, A. Robertsson, and R. Johansson (2012). "Increasing the milling accuracy for industrial robots using a piezo-actuated high-dynamic micro manipulator". In: *IEEE/ASME Int. Conf. on Advanced Intelligent Mechatronics (AIM)*. Kaohsiung, Taiwan, pp. 104–110.

Spong, M. W., S. Hutchinson, and M. Vidyasagar (2006). *Robot Modeling and Control*. John Wiley & Sons.

Sun, Y. and B. Yang (2009). "Compensation of hysteresis nonlinearity for the piezoelectric actuators". In: *Proc. 3rd IEEE Int. Conf. on Computer Science and Information Technol. (ICCSIT)*. St. Louis, MO, pp. 307–312.

SUNDIALS (2013). SUite of Nonlinear and DIfferential/ALgebraic equation Solvers. URL: `https://computation.llnl.gov/casc/sundials/main.html`.

Sundström, P., M. Jonasson, J. Andreasson, A. Stensson Trigell, and B. Jacobsson (2010). "Path and control optimisation for over-actuated vehicles in two safety-critical maneuvers". In: *10th Int. Symp. on Advanced Vehicle Control (AVEC)*. Loughborough, United Kingdom.

Velenis, E. and P. Tsiotras (2005). "Minimum time vs. maximum exit velocity path optimization during cornering". In: *IEEE Int. Symp. on Industrial Electronics (ISIE)*. Dubrovnik, Croatia, pp. 355–360.

Velenis, E. (2011). "FWD vehicle drifting control: the handbrake-cornering technique". In: *IEEE Conf. on Decision and Control (CDC)*. Orlando, FL, pp. 3258–3263.

Verhaegen, M. and P. Dewilde (1992). "Subspace model identification—The output-error state-space model identification class of algorithms". *Int. J. Control* **56**, pp. 1187–1210.

Vuong, N. D., M. H. Ang Jr., T. M. Lim, and S. Y. Lim (2009). "Multi-rate operational space control of compliant motion in robotic manipulators". In: *Proc. IEEE Int. Conf. on Systems, Man and Cybernetics*, pp. 3175–3180.

Wächter, A. and L. T. Biegler (2006). "On the implementation of an interior-point filter line-search algorithm for large-scale nonlinear programming". *Mathematical Programming* **106**:1, pp. 25–57.

Wang, J., H. Zhang, and T. Fuhlbrigge (2009). "Improving machining accuracy with robot deformation compensation". In: *Proc. IEEE/RSJ Int. Conf. on Intelligent Robots and Systems (IROS)*. St. Louis, MO, pp. 3826–3831.

Xu, J.-H. (1993). "Neural network control of a piezo tool positioner". In: *Proc. Canadian Conf. on Electrical and Computer Engineering*. Vancouver, Canada, pp. 333–336.

Zhang, H., J. Wang, G. Zhang, Z. Gan, Z. Pan, H. Cui, and Z. Zhu (2005). "Machining with flexible manipulator: Toward improving robotic machining performance". In: *Proc. IEEE/ASME Int. Conf. Advanced Intelligent Mechatronics (AIM)*. Monterey, CA, pp. 1127–1132.

A

Vehicle and Tire Model Parameters

In this appendix, the model parameters for the vehicle and tire configurations investigated in Chapter 8 and Chapter 9 are provided.

Table A.1 Vehicle model parameters used in the different vehicle model configurations studied in Chapter 8 and Chapter 9.

Notation	Value	Unit
l_f	1.3	m
l_r	1.5	m
w	0.8	m
m	2 100	kg
I_{xx}	765	kgm^2
I_{yy}	3 477	kgm^2
I_{zz}	3 900	kgm^2
R_e	0.3	m
R_w	0.3	m
σ	0.3	m
I_w	4.0	kgm^2
g	9.82	ms^{-2}
h	0.5	m
K_ϕ	178 000	Nm/rad
D_ϕ	16 000	Nms/rad
K_θ	363 540	Nm/rad
D_θ	30 960	Nms/rad

Table A.2 Tire model parameters for friction ellipse with isotropic behavior (FE-Iso), nonisotropic behavior (FE-Noniso), and weighting functions with isotropic behavior (WF-Iso), nonisotropic behavior (WF-Noniso), studied in Chapter 8. Note that in (8.17)–(8.18) in Chapter 8 the relations $B_{x,i} = C_{\kappa,i}/(\mu_x F_{z,i} C_x)$ and $B_{y,i} = C_{\alpha,i}/(\mu_y F_{z,i} C_y)$, $i \in \{f, r\}$, hold.

Parameter	FE-Iso	FE-Noniso	WF-Iso	WF-Noniso
μ_x	1.0	1.2	1.0	1.2
μ_y	1.0	1.0	1.0	1.0
$C_{\alpha,f}$	1.09e5	1.09e5	1.09e5	1.09e5
$C_{\alpha,r}$	1.02e5	1.02e5	1.02e5	1.02e5
$C_{\kappa,f}$	1.09e5	2.38e5	1.09e5	2.38e5
$C_{\kappa,r}$	1.02e5	2.06e5	1.02e5	2.06e5
C_x	1.3	1.7	1.3	1.7
C_y	1.3	1.3	1.3	1.3
$B_{x1,f}$	-	-	8.55	11.23
$B_{x2,f}$	-	-	8.33	10.80
$C_{x\alpha,f}$	-	-	1.03	1.14
$B_{y1,f}$	-	-	8.63	6.37
$B_{y2,f}$	-	-	8.35	2.64
$B_{y3,f}$	-	-	0	0
$C_{y\kappa,f}$	-	-	1.03	1.03
$B_{x1,r}$	-	-	9.28	11.71
$B_{x2,r}$	-	-	9.04	11.61
$C_{xa,r}$	-	-	1.03	1.14
$B_{y1,r}$	-	-	9.38	5.88
$B_{y2,r}$	-	-	9.08	2.98
$B_{y3,r}$	-	-	0	0
$C_{y\kappa,r}$	-	-	1.02	1.08

Table A.3 Tire model parameters used to represent dry asphalt, wet asphalt, snow, and smooth ice in Chapter 9.

Parameter	Dry	Wet	Snow	Ice
$\mu_{x,f}$	1.20	1.06	0.407	0.172
$\mu_{x,r}$	1.20	1.07	0.409	0.173
$B_{x,f}$	11.7	12.0	10.2	31.1
$B_{x,r}$	11.1	11.5	9.71	29.5
$C_{x,f}, C_{x,r}$	1.69	1.80	1.96	1.77
$E_{x,f}$	0.377	0.313	0.651	0.710
$E_{x,r}$	0.362	0.300	0.624	0.681
$\mu_{y,f}$	0.935	0.885	0.383	0.162
$\mu_{y,r}$	0.961	0.911	0.394	0.167
$B_{y,f}$	8.86	10.7	19.1	28.4
$B_{y,r}$	9.30	11.3	20.0	30.0
$C_{y,f}, C_{y,r}$	1.19	1.07	0.550	1.48
$E_{y,f}$	-1.21	-2.14	-2.10	-1.18
$E_{y,r}$	-1.11	-1.97	-1.93	-1.08
$C_{x\alpha,f}, C_{x\alpha,r}$	1.09	1.09	1.09	1.02
$B_{x1,f}, B_{x1,r}$	12.4	13.0	15.4	75.4
$B_{x2,f}, B_{x2,r}$	-10.8	-10.8	-10.8	-43.1
$C_{y\kappa,f}, C_{y\kappa,r}$	1.08	1.08	1.08	0.984
$B_{y1,f}, B_{y1,r}$	6.46	6.78	4.19	33.8
$B_{y2,f}, B_{y2,r}$	4.20	4.20	4.20	42.0

B

Code Listings

Listing B.1 The Modelica and Optimica code implementing the hairpin maneuver problem with the single-track model with isotropic tire model, discussed in Section 8.5.

```
optimization hairpin (objective = finalTime,
                                  startTime=0,
                                  finalTime(free=true,
                                  min=0.1,
                                  initialGuess=10))

  // Input signals
  constant Real ddeltamax = 1; // Max steer rate
  constant Real deltamax = 0.5;   // Max steer angle
  Real delta(start=0, fixed=true, min=-deltamax,
             max=deltamax, nominal=0.2);
  input Real ddelta(start=0, fixed=true, min=-ddeltamax,
             max=ddeltamax);

  input Real Twf(min=-car.Twfmax, max=0,
                 nominal=car.Twfmax);
  input Real Twr(min=-car.Twrmax, max=car.Twrmax,
                 nominal=car.Twrmax);

  // Geometric track parameters
  constant Real R1i = 3;
  constant Real R2i = 50;
  constant Real R1o = 8;
  constant Real R2o = 58;

  // Define initial and final positions of the car
  parameter Real X_final = (R1i+R1o)/2;
  parameter Real Y_final = 0;
  parameter Real psi_final = -Modelica.Constants.pi/2;
```

```
30
31    // Define car model, initial coordinates, and vx
32    CarModel car(X0=-(R1i+R1o)/2, Y0=0,
33                              vx0=25/3.6, X(min=-8, max=8),
34                              Y(min=0, max=55),
35                              beta(min=-1, max=5));
36
37    equation
38      der(delta) = ddelta;
39      connect(delta, car.delta);
40      connect(Twf, car.Twf);
41      connect(Twr, car.Twr);
42
43    constraint
44      (car.X/R1i)^6 + (car.Y/R2i)^6 >= 1;
45      (car.X/R1o)^6 + (car.Y/R2o)^6 <= 1;
46
47      car.X(finalTime) = X_final;
48      car.Y(finalTime) = Y_final;
49      car.psi(finalTime) = psi_final;
50  end hairpin;
51
52
53  //////// VEHICLE MODEL ////////
54
55  model CarModel
56    constant Real pi = Modelica.Constants.pi;
57
58    // Initial parameters
59    parameter Real X0 = 0;
60    parameter Real Y0 = 0;
61    parameter Real vx0 = 25;
62
63    // Vehicle properties
64    parameter Real l = 2.8;
65    parameter Real lf = 1.3;
66    parameter Real lr = l-lf;
67    parameter Real m = 2100;
68    parameter Real Izz = 3900;
69    parameter Real g = 9.82;
70
71    // Tire parameters
72    parameter Real mu = 1;
73    parameter Real Cf = 1.09e5;
74    parameter Real Cr = 1.02e5;
75    parameter Real Fzf = m*g*lr/l;
```

```
76    parameter Real Fzr = m*g*lf/l;
77    parameter Real C = 1.3;
78    parameter Real Bf = Cf/(mu*Fzf*C);
79    parameter Real Br = Cr/(mu*Fzr*C);
80
81    parameter Real Rw = 0.3; // loaded wheel radius
82    parameter Real Iw = 4;
83
84    parameter Real Twfmax = mu*Fzf*Rw;
85    parameter Real Twrmax = mu*Fzr*Rw;
86    parameter Real Fxfmax = mu*Fzf;
87    parameter Real Fxrmax = mu*Fzr;
88    parameter Real Fyfmax = mu*Fzf;
89    parameter Real Fyrmax = mu*Fzr;
90
91    // Model inputs
92    Modelica.Blocks.Interfaces.RealInput delta(min=-0.5,
93                                max=0.5, nominal=0.2);
94    Modelica.Blocks.Interfaces.RealInput Twf(min=-Twfmax,
95                                max=0, nominal=Twfmax);
96    Modelica.Blocks.Interfaces.RealInput Twr(min=-Twrmax,
97                                max=Twrmax, nominal=Twrmax);
98
99    // Model variables
100   Real X(nominal=50, start=X0, fixed=true);
101   Real Y(nominal=10, start=Y0, fixed=true);
102   Real psi(nominal=pi, start=pi/2, fixed=true);
103   Real vy(nominal=1, start=0, fixed=true);
104   Real vx(nominal=10, start=vx0, fixed=true, min=5);
105   Real dpsi(nominal=1, start=0, fixed=false);
106   Real alphaf(nominal=0.2, start=0);
107   Real alphar(nominal=0.2, start=0);
108   Real beta(nominal=0.2, start=0, fixed=true);
109   Real Fyf0(nominal=mu*Fzf, start=0);
110   Real Fyr0(nominal=mu*Fzr, start=0);
111   Real Fyf(nominal=mu*Fzf, start=0,
112                min=-Fyfmax, max=Fyfmax);
113   Real Fyr(nominal=mu*Fzr, start=0,
114                min=-Fyrmax, max=Fyrmax);
115   Real Fxf(nominal=mu*Fzf, start=0,
116                min=-Fxfmax, max=Fxfmax);
117   Real Fxr(nominal=mu*Fzr, start=0,
118                min=-Fxrmax, max=Fxrmax);
119   Real omegaf(nominal=30, start=vx0/Re, fixed=true);
120   Real omegar(nominal=30, start=vx0/Re, fixed=true);
121   Real kappaf(nominal=0.3, start=0);
```

```
122     Real kappar(nominal=0.3, start=0);
123     Real vxf(nominal=10, start=vx0);
124     Real vxr(nominal=10, start=vx0);
125
126     equation
127       beta = vy/vx;
128
129       // Motion equations
130       (der(vy)+vx*dpsi)*m = (Fyf*cos(delta) +
131                              Fyr + Fxf*sin(delta));
132       der(dpsi)*Izz  = (lf*Fyf*cos(delta) - lr*Fyr +
133                              lf*Fxf*sin(delta));
134       (-vy*dpsi+der(vx))*m = (Fxf*cos(delta) +
135                              Fxr - Fyf*sin(delta));
136
137       Twf - Iw*der(omegaf) - Fxf*Rw = 0;
138       Twr - Iw*der(omegar) - Fxr*Rw = 0;
139
140       // Slip angles
141       alphaf = delta - atan((vy + lf*dpsi)/vx);
142       alphar = -atan((vy - lr*dpsi)/vx);
143
144       vxf = vx*cos(delta) + (vy+lf*dpsi)*sin(delta);
145       vxr = vx;
146
147       kappaf = (Rw*omegaf - vxf)/vxf;
148       kappar = (Rw*omegar - vxr)/vxr;
149
150       // Tire forces
151       Fxf = mu*Fzf*sin(C*atan(Bf*kappaf));
152       Fxr = mu*Fzr*sin(C*atan(Br*kappar));
153
154       Fyf0 = mu*Fzf*sin(C*atan(Bf*alphaf));
155       Fyr0 = mu*Fzr*sin(C*atan(Br*alphar));
156
157       Fyf = Fyf0*(1 - 0.9999*(Fxf/Fxfmax)^2)^0.5;
158       Fyr = Fyr0*(1 - 0.9999*(Fxr/Fxrmax)^2)^0.5;
159
160       // Global coordinates
161       der(psi) = dpsi;
162       der(X) = vx*cos(psi) - vy*sin(psi);
163       der(Y) = vx*sin(psi) + vy*cos(psi);
164   end CarModel;
```

Department of Automatic Control
Lund University
Box 118
SE-221 00 Lund Sweden

Document name
LICENTIATE THESIS

Date of issue
April 2013

Document Number
ISRN LUTFD2/TFRT--3259--SE

Author(s)
Björn Olofsson

Supervisor
Anders Robertsson, Rolf Johansson

Sponsoring organisation
EU FP7, SSF/ProViking

Title and subtitle
Topics in Machining with Industrial Robots and Optimal Control of Vehicles

Abstract

Two main topics are considered in this thesis: Machining with industrial robots and optimal control of road-vehicles in critical maneuvers. The motivation for research on the first subject is the need for flexible and accurate production processes employing industrial robots as their main component. The challenge to overcome here is to achieve high-accuracy machining solutions, in spite of strong process forces affecting the robot end-effector. Because of the process forces, the nonlinear dynamics of the manipulator, such as the joint compliance and backlash, significantly degrade the achieved position accuracy of the machined part. In this thesis, a macro/micro manipulator configuration is considered to the purpose of increasing the position accuracy. In particular, a model-based control architecture is developed for control of the micro manipulator. The macro/micro manipulator configuration are validated by experimental results from milling tests in aluminium. The main result is that the proposed actuator configuration, combined with the control architecture proposed in this thesis, can be used for increasing the accuracy of industrial machining processes with robots.

The interest for research on optimal control of road-vehicles in time-critical maneuvers is mainly driven by the desire to devise improved vehicle safety systems. Primarily, the solution of an optimal control problem for a specific cost function and model configuration can provide indication of performance limits as well as inspiration for control strategies in time-critical maneuvering situations. In this thesis, a methodology for solving this kind of problems is discussed. More specifically, vehicle and tire modeling and the optimization formulation required to get useful solutions to these problems are investigated. Simulation results are presented for different vehicle models, under varying road-surface conditions, in aggressive maneuvers, where in particular the tires are performing at their limits. The obtained results are evaluated and compared. The main conclusion here is that even simplified road-vehicle models are able to replicate behavior observed when experienced drivers are handling vehicles in time-critical maneuvers. Hence, it is plausible that the results presented in this thesis provide a basis for development of future optimization-based driver assistance technologies.

Key words

Classification system and/or index terms (if any)

Supplementary bibliographical information

ISSN and key title
0280–5316

ISBN

Language
English

Number of pages
134

Recipient's notes

Security classification